

THERMAL CHARACTERIZATION AND MODELING OF
NANOSTRUCTURED MATERIALS

A DISSERTATION

SUBMITTED TO THE DEPARTMENT OF MECHANICAL ENGINEERING

AND THE COMMITTEE ON GRADUATE STUDIES

OF STANFORD UNIVERSITY

IN PARTIAL FULFILLMENT OF THE REQUIREMENTS FOR THE DEGREE OF
DOCTOR OF PHILOSOPHY

Matthew A. Panzer

June 2010

© 2010 by Matthew Alan Panzer. All Rights Reserved.

Re-distributed by Stanford University under license with the author.



This work is licensed under a Creative Commons Attribution-Noncommercial 3.0 United States License.

<http://creativecommons.org/licenses/by-nc/3.0/us/>

This dissertation is online at: <http://purl.stanford.edu/km615kq7832>

I certify that I have read this dissertation and that, in my opinion, it is fully adequate in scope and quality as a dissertation for the degree of Doctor of Philosophy.

Kenneth Goodson, Primary Adviser

I certify that I have read this dissertation and that, in my opinion, it is fully adequate in scope and quality as a dissertation for the degree of Doctor of Philosophy.

Bruce Clemens

I certify that I have read this dissertation and that, in my opinion, it is fully adequate in scope and quality as a dissertation for the degree of Doctor of Philosophy.

Ravi Prasher

Approved for the Stanford University Committee on Graduate Studies.

Patricia J. Gumpert, Vice Provost Graduate Education

This signature page was generated electronically upon submission of this dissertation in electronic format. An original signed hard copy of the signature page is on file in University Archives.

Abstract

Thermal conduction resistances are becoming increasingly complicated as advanced materials, photonics, and electronic devices incorporate more nanostructured features (e.g. carbon nanotubes (CNTs), ultra-thin films, nanoparticles, etc.). The reduced dimensions and large interface densities of nanostructured materials modify the energy transport physics, requiring the development of new thermal models and thermal metrology techniques with deep sub-micron spatial resolution. This research develops and applies ultra-fast (nanosecond thermoreflectance (TR) and picosecond time-domain thermoreflectance (TDTR)) to characterize thermal resistances in carbon nanotube arrays and thin-film materials. In conjunction, this work develops novel models of thermal transport within the nanostructured material and interfaces.

Owing to their high intrinsic thermal conductivities (~ 3000 W/m/K), aligned arrays of CNTs are promising for use in advanced thermal interface materials. Nanosecond TR data for metal-coated aligned nanotube films show that the thermal resistance of the films is dominated by interfaces due to incomplete CNT-metal contact, and that the thermal resistance of these films can be significantly reduced by varying the metallic composition at the interface. This work presents data for the growth-interface thermal resistance of multiwalled carbon nanotubes measured directly using TDTR with a variable modulation frequency technique.

The abrupt changes in geometry at nanostructured interfaces induce phonon confinement, which creates additional contributions to the interface resistance. This work investigates model problems of thermal transport through abrupt junctions between a one-dimensional lattice in contact with a two- and three-dimensional lattice using a Green's function approach. The model indicates that the thermal resistances due to dimensional mismatch are comparable to those due to material property mismatch effects. Finally, the results suggest that engineering an intentional

impedance mismatch at a nanostructured interface may enhance the transmission of energy.

This work also develops a picoseconds pump/probe thermoreflectance system to achieve deep sub-micron spatial resolution of thermal properties of ultra-thin hafnium oxide films, which are promising for the next generation of gate oxides for transistors. These data isolate the intrinsic film resistance and show that crystalline nanoparticles reduce the intrinsic thermal conductivity its bulk value.

Acknowledgements

I would like to first thank my advisor, Prof. Goodson, for providing me the opportunity to work in his research group and for his continued support and guidance throughout my graduate program, particularly the freedom, encouragement, and opportunities to pursue and develop my research interests. I greatly enjoyed and learned from our discussions over the years. I would also like to thank Prof. Clemens, Prof. P. Wong, and Dr. Prasher, for serving on my thesis committee and providing valuable feedback.

This research program was made possible by the many collaborators who provided the samples and material support, and to whom I owe many thanks. Prof. H. Dai, Dr. Dave Mann, and Dr. Guangyu Zhang provided some of the initial nanotubes samples which founded this thesis work. Great thanks to Molecular Nanosystems, Inc. (Dr. Lawrence Pan, Clark Dong, and Senyo Dogbe) for their commitment and continued support through my thesis work. Senyo Dogbe and Lawrence Pan spent countless hours, which were often on personal time and weekends, to provide nanotubes samples for my work and feedback on research. I would also like to thank Prof. Wardle at MIT and his students, Dr. Hai Duong and N. Yamamoto; Prof. Maruyama and Prof. Shiomi at U. Tokyo; and Prof. Cola at Georgia Tech for their collaboration in developing interesting sample materials and for technical discussions. Dr. Chuan Hu (Intel) and Dr. Maxat Touzelhaev provided invaluable technical and materials characterization support.

I would like to thank my fellow group members, from whom I benefited greatly with discussions and their input, feedback, and assistance: Eric Pop, Sanjiv Sinha, Carlos Hidrovo, Angie McConnell, Tricia Gharagozloo, Milnes David, Saurabh Chandorkar, Yoonjin Won, Jeff Weisse, and SangBum Kim. I would like to thank Xuejiao Hu for being my mentor and helping me get started on my research program. It has been an honor to work with Jeremy Rowlette and John Reifenberg, who have

been great friends and colleagues and from whom I have learned so much. I thoroughly enjoyed the hours I spent with them both in and out of the lab, and I could always count on their help, support, advice, insight, and critical feedback. Special thanks to our administrative assistant, Cecilia Gichane-Bell who was always so kind and helpful and the financial support of the Stanford Graduate Fellowship, SRC, ONR, and DARPA.

Special thanks to all the friends that I have made along the way who have made my time here at Stanford so enjoyable and memorable. Finally, I must thank my family for all their love and support throughout the years and who have provided the opportunities and guidance that have led me here.

Contents

Abstract	iv
Acknowledgements	vi
List of Tables.....	xi
List of Figures	xii
Chapter 1 Introduction.....	1
1.1 Importance of the Thermal Properties of Nanostructured Materials	1
1.2 Thermal Conduction Considerations in Nanostructured Materials	3
1.2.1 Classical Conduction Physics	3
1.2.2 Nanoscale Physical Considerations.....	5
1.2.3 Thermal Boundary Resistance	9
1.3 Carbon Nanotubes as a Nanostructured Thermal Material	11
1.4 Application of CNT Arrays: Advance Thermal Management Materials	16
1.5 Thermal Characterization Needs for Nanostructured Materials	19
1.6 Scope of Work	20
1.7 Organization	20
Chapter 2 Thermal Characterization of Metal-coated Aligned Nanotube Arrays	22
2.1 Thermal Properties of Metal-Coated Vertically-Aligned Single-Wall Nanotube Arrays.....	22
2.1.1 Introduction.....	22
2.1.2 Experimental Method	25
2.1.2.1 Sample Preparation.....	25
2.1.2.2 Experimental Setup and Procedure.....	27
2.1.2.3 Data Extraction Model and Method	30
2.1.3 Results and Discussion	32

2.1.4 Thermal Model for Conduction in CNT Films.....	36
2.1.5 Summary and Conclusions	45
2.2 Temperature-dependent Phonon Conduction and Composition Dependence of Nanotube Engagement in Metalized Single Wall Carbon Nannotube Films	46
2.2.1 Introduction and Motivation.....	46
2.2.2 Sample Preparation and Thermal Property Measurement	47
2.2.3 Data Results and Interpretation	50
2.2.4 Conclusion.....	59
2.3 Reduction of Resistances in MWNT Films through Interface Engineering: CNT- indium Composites.....	59
2.3.1 Concept and Background	59
2.3.2 Sample Preparation and Metrology	61
2.3.3 Thermal Resistance Data for Indium-MWNT Composites	62
2.4 Summary of Conduction Mechanisms in CNT Films	66
Chapter 3 Picosecond Thermoreflectance Thermometry of MWNT Growth Interfaces	68
3.1 Motivation.....	68
3.1.1 The Need for Picosecond Thermoreflectance Thermometry of MWNT Growth Interfaces	68
3.1.2 Conduction Regime Considerations for Picosecond Thermoreflectance Measurements of CNT Growth Interfaces.....	69
3.2 Multi-frequency Picosecond Time Domain Thermoreflectance Technique (TDTR)	73
3.2.1 Overview of the Picosecond TDTR Technique and System.....	73
3.2.2 Thermal Model of TDTR Signal for Thermal Property Extraction.....	78
3.2.2.1 Interpretation of the Lock-in Signal.....	78
3.2.2.2 Frequency Domain Response of Stacked Sample Structure	81
3.3 Sample Preparation for TDTR Measurement of MWNT Growth Interfaces	87
3.4 Measurement Results and Data Interpretation	88
3.5 Summary and Future Directions.....	91

Chapter 4 Thermal Resistance between Low-Dimensional Nanostructures and Semi-Infinite Media	93
4.1 Introduction.....	93
4.2 Model	97
4.2.1 Model Overview and Interface Geometry	97
4.2.2 Surface Green's Function for Semi-infinite Lattice	99
4.2.3 Energy Transmission between the 1D and Semi-infinite Lattices	108
4.3 Results and Discussion.....	112
4.4 Conclusions.....	122
Chapter 5 Thermal Properties of Ultra-thin Hafnium Oxide Gate Dielectric Films	123
5.1 Introduction.....	123
5.2 Sample Fabrication and Experimental Setup.....	124
5.3 Results and Discussion	126
5.4 Conclusion	129
Chapter 6 Conclusion	131
6.1 Summary.....	131
6.2 Discussion and Suggestions for Future Work	135
6.2.1 Thermal Properties of CNT Interface Materials	135
6.2.2 Mechanical Properties of CNT Films	137
6.2.3 Engineering and Fundamental Physics of Interface Resistances in Nanostructures	139
Bibliography.....	140

List of Tables

Table 2.1: Best-fit values averaged from multiple measurements of $C_{cnt,eff}$, $R''_{cnt-Pd,eff}$, $R''_{cnt-SiO_2,eff}$, and $k_{cnt,eff}$ for the 28 μm thick sample along with their associated uncertainty. The uncertainty is calculated from the RMS variation in extracted parameters individually fit to multiple measurements.	33
Table 3.1: Extracted properties for the MWNT/ Al_2O_3 /W/ SiO_2 film structure.....	89
Table 5.1: Structure, composition, and thermal properties of HfO_2 sample films.....	126

List of Figures

Figure 1.1: Illustration of a common general geometry encountered in nanoscale energy transport. Energy is transported from a high temperature region to a low temperature reservoir through the nanostructure, represented by the bold outlined rectangular region. In general, the nanostructure can sustain an electric current (j) and a heat flux (q''); in dielectrics, the heat flux is dominated by phonon (illustrated by green circle) conduction. The total thermal resistance is due to a combination of interface scattering (illustrated by dotted gray arrows) and volumetric effects such as scattering with defects, boundaries, and carriers, the physics of which are strongly modified in the ballistic ($L < \Lambda$) and mesoscopic regimes ($L < \lambda$) due to reduced dimensions.....7

Figure 1.2: Schematic illustration of the relative magnitudes of volumetric and interface resistances as a function of length scale. As the length scale is reduced, the ratio of TBR to volumetric resistance increases, with the TBR becoming the dominant resistance. Such a transition can occur at length scales of microns for high conductivity materials (e.g. CNTs) down to ~ 10 nm for low conductivity materials (e.g. SiO₂).9

Figure 1.3: Carbon Nanotube Structure: Schematic of a 2-d graphene sheet. Carbon atoms are arranged in a honeycomb lattice with lattice vectors \mathbf{a}_1 and \mathbf{a}_2 . A carbon nanotube is a rolled up sheet of graphene, where the ends of the chiral vector are connected, the sheet becomes a tube, and the tube that is aligned with the translation vector, \mathbf{T} . The chiral vector is $\vec{OA} = n\vec{a}_1 + m\vec{a}_2$, where n and m are integers, and the nanotube chirality is described by (n,m) . The chiral angle, θ , is defined from the zigzag $(n,0)$ axis. Figures adapted from Saito et al. [35]..... 13

Figure 1.4: Illustration of thermal conduction pathways in a common configuration for a microprocessor and its packaging. The thermal interface resistances along the pathway from the generation region within the device to the ambient environment constitute a significant fraction of the thermal budget. The TIM material increases the real contact area by conforming to the surface topography. The total resistance of the TIM is the sum of its interface resistances with the two materials and the volumetric contribution, which depends on the TIM thermal conductivity and the bond line thickness (BLT). Figure adapted from reference [49]...... 17

Figure 1.5: Illustration of the relation between total thermal resistance and elastic moduli of common TIM materials such as solder and greases. With conventional materials, reduced resistances often come at the expense of increasing elastic modulus, which reduces reliability and increases thermal degradation during thermal cycling. Engineering materials with nanofeatures such as carbon nanotubes or nanoparticles offers the possibility of achieving materials with reduced resistances, potentially below $0.01 \text{ cm}^2\text{K/W}$, while maintaining compliance. Representative material properties taken from literature [49]. 18

Figure 2.1: a) SEM profile of aligned SWNTs grown on Si—the tube length is $28 \text{ }\mu\text{m}$. The SWNT diameter ranges between 1 nm and 2 nm, with an average of approximately 1.3 nm. b) AFM topographic profile of the top of the CNT film, which indicates that the RMS surface roughness is $\sim 60 \text{ nm}$. c) SEM of top of the metal film after it has been deposited on CNTs. The image shows that the metal film is porous at a scale below 100 nm. 27

Figure 2.2: a) Schematic of the thermoreflectance thermometry experimental setup including the optical and signal paths. b) Schematic of sample geometry. The initial deposition of 20 nm thick layer of palladium on the SWNT ends forms an adhesion layer with the 160 nm thick aluminum film used for thermal reflectance thermometry. 28

Figure 2.3: Typical thermal response trace data for a particular measurement (solid) for 28 μm sample along with the best fit analytical solution evaluated with the average best fit parameters summarized in Table 2.1 (dashed). The data show two characteristic decay time scales during the measurement: the initial rapid decay lasting $\sim 0.5 \mu\text{s}$ followed by a longer decay lasting $\sim 4 \mu\text{s}$34

Figure 2.4: Schematic illustrating the hypothesis that a subset of the CNTs are in good thermal contact with the porous and discontinuous evaporated film. The data suggest that the overwhelming majority of the heat transport is brought about by longer tubes that fully contact the metal film. We use a thermal circuit model to account for lateral thermal transport in the CNT film. The heat flows into the central tube that is in thermal contact with the metal film and then flow laterally through the inter-tube coupling resistance to surrounding tubes. We reduce the thermal network to a frequency dependant parallel equivalent RC thermal circuit, which is what is experimentally measured.37

Figure 2.5: a) Schematic top view of CNT in a close pack arrangement grouped into concentric shells of neighboring tubes to calculate the effective impedance of the series of neighboring tubes, as assumed in the model. b) Block diagram of impedance network modeling the linking of neighboring shells by and inter-shell thermal resistance.40

Figure 2.6: The effective thermal capacity, $C_{th,eq}$, and thermal resistance, R_{eq} , due to inter-tube coupling effects normalized to that of an individual tube as a function the inter-tube coupling resistance R''_i41

Figure 2.7: a) Representative TEM of SWNT-metal contact showing voids and incomplete contact near the metal interface. b) Schematic of sample geometry used in the measurements and for the thermal model. c) Representative thermal trace data for the 100 nm Al-coated sample (black)

along with optimal fit (solid red) yielding the optimal parameter set $R_{met-SWNT}^*$, R_{sv}^* , and $C_{v,eff}^*$. The blue and green traces illustrate the data extraction sensitivity, showing the results of varying one of the fit parameters from its optimal value and re-optimizing the fit of the remaining two free parameters to the data. 48

Figure 2.8: a) Measured area-averaged metal-SWNT, SWNT-substrate, and total thermal resistance plotted as a function of the measured effective SWNT heat capacity volume fraction, ϕ , calculated by dividing the measured effective SWNT volumetric heat capacity $C_{v,eff}$, by the volumetric heat capacity of an individual SWNT, $C_{v,ind}$. b) Estimated resistance of individual metal-SWNT contact extracted by multiplying the area-average metal-SWNT interface resistance by ϕ . Data are compared to theoretical predictions of the individual SWNT interface resistance from molecular dynamics of SWNT-Si interfaces from M. Hu *et al.* [104] and Daio *et al.* [105] (gray-dashed arrows) and from the AMM model modified for 2D-2D interfaces. [48] The theoretical values are shown on the right axis for clarity. 52

Figure 2.9: a) Temperature dependence of the area-average metal-SWNT interface and effective $C_{v,eff}$ for a 100 nm-thick Al-coated SWNT film. The data are compared to theoretical calculation of the heat capacity of an individual SWNT based on Bose-Einstein statistics using a classical potential function [109] (black-dashed) and a calculation of the heat capacity of graphene acoustic modes (red-solid) based on graphene parameters in Prasher *et al.* [43] The theoretical predictions have been scaled by a factor of 0.006 so that the value of the data matches the SWNT theoretical results at 300 K. Also shown are the contributions of the graphene longitudinal (LA), transverse (TA), and out-of-plane bending (ZA) acoustic phonon bands to the total graphene heat capacity. b) Temperature dependence of the conductance of individual SWNT interfaces, $(R_{met-SWNT} \times \phi)^{-1}$ and

$(R_{sv} \times \phi)^{-1}$. The gray dashed curves are optimal power law fits to the data. The solid red curve is the total theoretical upper bound for the interface conductance of a graphene-metal interface allowing for inelastic scattering. The broken red curves show the contributions from the individual acoustic phonon modes in graphene.56

Figure 2.10: Temperature dependence of $I^{inel}(T)$ along with the optimal power law fit (gray-dashed). The temperature dependence suggests inelastic phonon scattering at the interface.58

Figure 2.11: Schematic illustration of CNT-binder composite to reduce the resistance in CNT films. The binder is deposited on the CNT ends and is heated after forming an interface to allow the binder to conform to the CNT topography, increasing the real contact area. A thermal tape structure may provide a convenient vehicle to implement CNT films in thermal management solutions.61

Figure 2.12: Schematic of indium-MWNT composite and IR microscopy configuration. The IR microscope produces a full-field image of the cross-sectional temperature profile under a steady state heat flux. Measuring temperature drop across the TIM enable the extraction of the TIM thermal resistance.62

Figure 2.13: Total thermal resistance data for In-MWNT composites consisting of various thicknesses of MWNT films, along with the Al/Pd/SNWT sample presented previously in this work, and an interface consisting of only indium without CNT. The best performing sample has a resistance of 0.07 cm²K/W. Representative cross sections temperature profiles show that the relative distribution between interface and volume resistance depends on the samples.63

Figure 2.14: a) Impact of thermal cycling on the total thermal resistance of 175 μm thick In-MNWT composite sample. b) Schematic illustration of the thermal cycle.	65
Figure 2.15: a) Total thermal resistance CNT-In composites with un-fluxed Ti/Ni/Au adhesion layers of thickness 100/50/100 nm on both indium interfaces. b) Acoustic transmission image of an In-CNT sample showing poor mechanical bonding of the indium. Dark areas indicate high transmission and strong metallurgical bonds. (acoustic transmission image courtesy of Advance Micro Devices, Inc.).....	65
Figure 2.16: Cartoon illustration summarizing the important conduction mechanisms in CNT films and typical values for interface and volume resistances. Partial engagement of the CNT films amplifies nanoscale interface and volume resistances	67
Figure 3.1: The schematic on the left illustrates the canonical thermoreflectance configuration for top heating and the relevant thermal properties. The total resistance (R_f) and capacitance (C_f) of the film depends on the individual CNT conductivity (k_i), heat capacity ($C_{v,f}$), CNT volume fraction (ϕ), CNT diffusivity (α_i), and measurement time scale (t) thorough the diffusion length $L \sim (\alpha_i t)^{1/2}$. The thermal circuit models represent a simple approximation to conduction in the array, where the metal capacitance discharges through an interface resistance into a parallel resistance and capacitance of the CNT film. The plot on the right schematically illustrates the conduction regimes for combinations of CNT capacitance and interface resistances. The size of the circuit elements in the different regimes represents their relative magnitude. For low density CNT films (1-3% vol), the thermal conduction depends strongly on all parameters, complicating data interpretation.	72

Figure 3.2: Schematic layout of the picosecond TDTR metrology platform developed in this work. See text for detailed explanation of the layout and key features of the system.	77
Figure 3.3: Sample thermal trace (black) with a well-characterized and behaved calibration sample consisting of a 102 nm thick thermal SiO ₂ film coated with 37 nm of Al on an Si substrate, illustrating and validate measurement systems, technique, and thermal model (red line).....	78
Figure 3.4: Example time-domain thermal response of sample structure with thermal overlap between pulses (solid blue) and probe signal (solid black circle), delayed from the pump, that is generate by a modulated pump pulse train (red squares).....	79
Figure 3.5: Schematic representation of generic multi-layer film structure for the thermal model of the sample structure. The thermal model developed in this work allows for an arbitrary number of layers, N , with Gaussian surface heating at an arbitrary interface and Gaussian temperature probing at an arbitrary interface. The boundary conditions enforce heat flux continuity and allow for interface resistances at all interfaces. The bounding layers are treated as semi-infinite.	82
Figure 3.6: Example phase data for calibration sample with well-known thermal properties.	86
Figure 3.7: Cross-sectional TEM of MWNT interface with an Al ₂ O ₃ /W/SiO ₂ substrate, illustrating a MWNT diameter of ~10 nm and wall thickness of ~2.5 nm. The TEM provides the thickness of the Al ₂ O ₃ and W films.....	88
Figure 3.8: TDRT data for the MWNT/Al ₂ O ₃ /W/SiO ₂ film for pump beam modulation frequencies of 1, 5, and 8 MHz. Simultaneously fitting the data to the thermal model for all three frequencies simultaneously extracts the CNT effective heat capacity through the volume fraction, ϕ , the effective	

MWNT-CNT interface resistance ($R_{eff,MWNT-Al_2O_3}$), and the W- Al_2O_3 interface resistance ($R_{W-Al_2O_3}$). The low frequency data are most sensitive to the heat capacitance of the MWNT film, and hence the effective volume fraction, while the high frequency data are most sensitive to the thermal properties confined near the temperature transducer. Due to the local self-heating of the lasers, the remaining known thermal properties are evaluated at 800 K. 90

Figure 4.1: Schematic illustration of the lattice geometry used in this study a) junction between a 1D lattice and the (001) surface of semi-infinite FCC lattice extending in the positive z direction. b) junction between 1D lattice and the (01) surface of a semi-infinite 2D square lattice extending in the positive z direction. 98

Figure 4.2: Comparison of the calculated value of the LDOS given by Eq. (4.29) using the two parameter model for the Si-like FCC lattice in this work (bottom) with calculations by Treglia *et al.* [152] using a four parameter recursive technique for Pd and Ni FCC lattices. The similarity in the structure of the LDOS indicate that this simple model captures the essential features of the LDOS and provide validation for the model. 107

Figure 4.3: a) Illustration of impact of increasing the bond stiffness parameters on the surface LDOS, which show that increasing the bond stiffness reduces the magnitude of the LDOS and stretches and flattens the features. b) Log-log plot of the LDOS in (a) showing quadratic low-frequency behavior which is predicted by continuum theory [153] and provides further validation for the model. 108

Figure 4.4: Transmission coefficient for longitudinal and transverse polarizations incident on the junction between the 1D and 3D (a, b) and 1D and 2D (c, d) lattices as a function of frequency normalized to the maximum longitudinal polarization of the 1D lattice. The solid black curves show

the transmission for lattices with identical stiffness and mass parameters for a “silicon-like” material. The blue dashed curve and red dotted curve show the impact of changing the ratio of the mass or lattice stiffness parameters in the semi-infinite lattice to those in the 1D lattice to 1.25 and 0.75, respectively. For the 3D case (a) shows the effect of scaling the stiffness and (b) show the effect scaling the mass. For the 2D case, (c) shows the effect of scaling the stiffness and (d) show the effect scaling the mass. The impact of scaling mass and stiffness are qualitatively quite similar, but differ in the details of the transmission curve shapes due to their unique role in the junction boundary conditions..... 113

Figure 4.5: The local density of states for out-of-plane displacements ($\rho_{3D,\perp}$, black solid) for the 3D lattice, in-plane ($\rho_{3D,\parallel}$, black dashed) for the 3D lattice, and out-of-plane ($\rho_{2D,\perp}$ red solid) for the 2D lattice. Also shown is the bulk DOS for the 1D lattice (red solid) and the corresponding transmission coefficients for the 3D and 2D cases. The frequency is normalized to the maximum frequency of the longitudinal mode in the 1D lattice. 115

Figure 4.6: Total thermal conductance as a function of temperature for a junction for both the 3D and 2D cases. (a) shows the impact of varying the stiffness scaling of the semi-infinite lattices or the junction conductance, and (b) shows the impact of varying the mass on the junction conductance. The solid black curves show the transmission for lattices with identical stiffness and mass parameters. The blue dashed curve and red dotted curve show the impact of changing the ratio of the mass or lattice stiffness parameters in the semi-infinite lattice to those in the 1D lattice to 1.25 and 0.75, respectively. The results show that there is a finite conductance of comparable magnitude to the acoustic mismatch conductance even for materials of identical stiffness parameters..... 118

- Figure 4.7: The junction conductance as a function of stiffness ratios between the semi-infinite and 1D lattice at 300 K (black solid circles) and 30 K (blue open circles) and mass ratios between the semi-infinite and 1D lattice at 300 K (black x) and 30 K (blue triangle). For each data set, the noted ratio is varied while all other parameters are held fixed. The results show that there is a maximum conductance for a for a stiffness ratio of ~ 0.5 and mass ratio of ~ 1.5 . The conductances at 30 K do not show a maximum conductance. 120
- Figure 5.1: a) Representative cross-sectional TEM of 200 Å thick sample showing HfO₂ nanocrystals embedded in an amorphous HfO₂ matrix. b) Plan view of the 118 Å sample showing a low density of HfO₂ nanoparticles in an amorphous matrix. c) Plan view of the 200 Å sample showing a high density of HfO₂ crystallites in an amorphous matrix..... 125
- Figure 5.2: a) Intrinsic HfO₂ thermal conductivity for 200 Å (black square), 118 Å red circle), and 56 Å (blue triangle) as a function of temperature. Predictions for the minimum thermal conductivity theory calculate using the atomic number density (solid black) are molecular density (black dashed) . b) Total thermal resistance for the HfO₂-SiO₂-Si interface, and DMM predictions in the Debye approximation (solid black) [22, 24] and using the specific heat correction to the density of states (red dashed) [24] ... 128
- Figure 6.1: Schematic of CNT grown on a microresonator and example cross section of a fabricated micro resonator for measuring the lateral elastic modulus and density of CNT films. The resonant frequency can be measured through using laser Doppler velocimetry and the thermal properties can be measured through the optical techniques developed in this work..... 138

Chapter 1

Introduction

1.1 Importance of the Thermal Properties of Nanostructured Materials

Engineering the structure of materials at nanometer length scales provides an opportunity to achieve unique combinations of physical properties that are otherwise unattainable with materials under natural conditions. Similarly, reducing the dimensions of electronic device features to nanometer dimensions offers the potential to not only improve device performance at higher packing densities, but also to exploit the modified physics of the nanoscale features to enable entirely new devices. From a more fundamental interest, these materials and devices can incorporate near pristine and ideal systems which can be tailored and exploited to study new physical phenomenon. However, the decreasing feature dimensions presents additional characterization and physical complexities which challenge performance, including unprecedented energy densities, non-continuum coupled transport, and high interface densities.

As device dimensions decrease, thermal loads tend to increase due to increasing electrical current and optical absorption densities. The modification in the thermal and electrical conduction physics due to the nanoscale dimensions can amplify local heating effects. It is not uncommon for a device such as a transistor or nanoparticle to generate an electron-volt of thermal energy in a few cubic nanometers of material, leading to local temperature rises on the order of several hundred Kelvin. These elevated temperatures can adversely affect device behavior, performance, and reliability. For example, the local hotspots created by ballistic phonon transport and

INTRODUCTION

geometric confinement effects in nanoscale CMOS transistors can create local effective phonon temperature rises of several hundred Kelvin in the drain, which can adversely affect electrical resistances in the device and other device performance metrics [1, 2]. In photonics, microcavities optically coupled to nanoparticles are promising on-chip and single photon sources. However, the emission wavelength stability is strongly affected by local temperatures, which often results from optical heating [3]. Predicting the thermal behavior of such materials is complicated by their reduced dimensions and high interface densities. Consequently, the thermal characterization and modeling of nanostructured materials is critical in understanding, predicting, and controlling phenomenon in devices and materials that incorporate nanostructured features.

Nanostructured materials can incorporate a variety of structures and features including thin-films, nanotubes, nanowires, nanoparticles, and even individual molecules. The combinations of geometry, materials, and structure of these systems can potentially be engineered to achieve desired combinations of physical properties. Carbon nanotubes (CNTs) are one of the more promising materials due to their outstanding thermal, electrical, optical, and mechanical properties. The combination of high thermal conductivity of individual CNTs at room temperature ($\sim 3600 \text{ W m}^{-1} \text{ K}^{-1}$ [4, 5]) and their ability to sustain large current densities ($\sim 10^9 \text{ J/cm}^2$) makes them attractive for electronic devices [1, 6]. Similarly, the combination of high thermal conductivity, large axial stiffness ($\sim 1 \text{ TPa}$) [7], strength [7], and flexibility can yield advanced multi-functional composites that can exhibit a wide range of properties. Although the thermal properties of ideal individual CNTs are potentially outstanding, realizing such values in practice are challenging due to a variety of effects that degrade their performance, such as interfaces and defects. The strongly reduced dimensions of CNTs and the long mean free path of phonons in these materials strongly amplifies the impact of these effects on the thermal properties compared to bulk and higher dimensional materials. A primary goal of this work is the separation

of the thermal properties arising within a material from those at the interface to understand the conduction physics in nanostructured materials.

1.2 Thermal Conduction Considerations in Nanostructured Materials

1.2.1 Classical Conduction Physics

Thermal transport is a relatively mature phenomenon and well understood in bulk materials. Energy transport can be described in terms of energy carriers (e.g. phonons, electrons, etc.), which randomly scatter, resulting in diffusive thermal transport. Such conduction phenomenon are captured by Fick's law of diffusion,

$$\vec{q}'' = -\vec{k} \bullet \nabla T \quad (1.1)$$

where \vec{q}'' is the heat flux, \vec{k} is the thermal conductivity of the material, which is in general a tensor, and ∇T is the temperature gradient. Combining Eq. 1 with energy conservation yields the heat diffusion equation for calculating the temperature field,

$$C_v \frac{\partial T}{\partial t} = \nabla \bullet (\vec{k} \bullet \nabla T) + \dot{Q}_{gen} \quad (1.2)$$

where C_v is the volumetric specific heat and \dot{Q}_{gen} is the volumetric heat generation rate. For solids in general, both electrons and lattice vibrations (phonons) contribute to the energy transport. Since this work focuses primarily on the properties of dielectric materials (e.g. carbon nanotubes, HfO_2 , etc.), where the thermal transport is dominated by lattice vibrations, this discussion will focus on the physics of energy transport by lattice vibrations.

INTRODUCTION

The vibrations of atoms in a crystal can be described in terms of the collective vibrational modes of the lattice, which can be calculated from the classical equations of motion of the atoms once the interatomic potential is known (c.f. reference [8]). Quantization of the lattice vibration field (i.e. vibration field amplitude and conjugate momentum do not commute) results in quantized amplitudes of vibration and the quantization of the mode energies such that the energy excitation levels of each mode can only occur in discrete multiples of the vibration frequency,

$$E = n\hbar\omega \quad (1.3)$$

where E is the mode energy, n is the mode occupation number, \hbar is Planck's constant divided by 2π , and ω is the vibration frequency of the mode. The quantization of these vibration modes, called phonons, endows the crystal excitations with both wave and particle-like behavior. Thus, the energy transport by phonons includes both particle-like behavior such as the collision (scattering) of phonons with other phonons or interfaces, and wave-like behavior such as interference and diffraction of phonon modes. For a system at finite temperature, phonon scattering drives the system toward thermal equilibrium, in which the number of phonons in each mode, n , is related to the temperature by the Planck distribution,

$$n = \frac{1}{\exp(\hbar\omega/k_bT) - 1} \quad (1.4)$$

where k_b is Boltzmann's constant.

For system sizes and length scales much larger than the phonon wavelength and phonon mean free path, the strong scattering of phonons leads to diffusive transport, which is well described by Eq. (1.1), where the thermal conductivity is a function of the phonon spectra and the phonon scattering rates, including scattering with other phonons, defects, and other carriers. The thermal conductivity results from a sum over

contributions of the energy flux of each vibration mode due to a temperature gradient, and for an isotropic 3D material can be expressed as

$$k = \frac{1}{3} \sum_{p=pol} \int_0^{\omega_{max}} C_v(\omega, T, p) v(\omega, p) \Lambda(\omega, p) d\omega \quad (1.5)$$

where $C_v(\omega)$ is the spectral specific heat, v is the phonon group velocity, p is the phonon branch, and Λ is the phonon mean free path, which is an appropriately defined average distance that a phonon travels before scattering. However, in nanostructured materials the reduction in system sizes to dimensions comparable to the mean free path or phonon wavelength strongly modifies the conduction physics, leading to a limited validity of Eqs. (1.1) and (1.5). Consequently, understanding and interpreting energy transport and thermal properties at the nanoscale requires a more complete understanding of nanoscale conduction physics, including models that incorporate ballistic and mesoscopic effects.

1.2.2 Nanoscale Physical Considerations

Figure 1.1 schematically illustrates a common general geometry encountered in nanoscale energy transport. As shown in the figure, the nanostructure sustains energy transport in the form of phonon and electron conduction from a high temperature region, which can possibly be within the nanostructure itself, to a low temperature reservoir. In general, there may be no clear distinction between the nanostructure and the reservoirs. Electrical currents or optical interactions may also deposit energy within the nanostructure. In the high temperature region, the phonon modes are excited with a distribution of occupation numbers given by Eq. (1.4) at a characteristic temperature T_h . To enter and conduct across the nanostructure, the phonons must traverse an interface between the reservoir and the nanostructure, which are in general two different materials. The abrupt change in material properties and geometry at the interface creates additional phonon scattering events, resulting in a thermal boundary

INTRODUCTION

resistance (TBR) highly localized near the interface. This scattering of phonons due to impedance mismatches between the two domains is analogous to sound waves reflecting off of a wall. The following section describes the physics of the TBR in more detail. Once entering the nanoobject, the phonons can scatter with other phonons, electrons, boundaries, or defects, creating volumetric contributions to the thermal resistance. Electrical current or optical interactions can also generate phonons (i.e. heating) and local scattering within the volume. After traversing the volume, the phonons then scatter into the thermal reservoir, typically through an additional interface. As with the interfaces, the volumetric resistances are modified compared to their bulk values when $L \gg \Lambda, \lambda$. With sub-continuum transport, thermal equilibrium, and hence temperature, are poorly defined, often making it challenging to unambiguously define intrinsic material properties (i.e. intrinsic conductivity, TBR, etc.) independent of the specific geometry since energy transport becomes non-local [9]. Under the conditions of sub-continuum transport, often it is only the total conductance of the nanostructure and its interfaces with thermal reservoirs that is a well defined quantity, with the interface transport strongly impacting the total conductance.

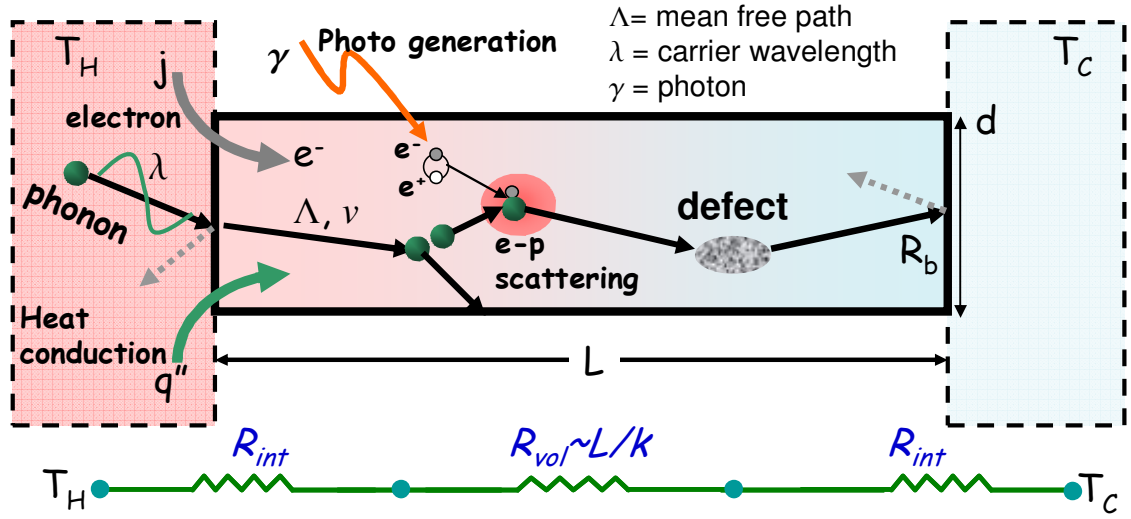


Figure 1.1: Illustration of a common general geometry encountered in nanoscale energy transport. Energy is transported from a high temperature region to a low temperature reservoir through the nanostructure, represented by the bold outlined rectangular region. In general, the nanostructure can sustain an electric current (j) and a heat flux (q''); in dielectrics, the heat flux is dominated by phonon (illustrated by green circle) conduction. The total thermal resistance is due to a combination of interface scattering (illustrated by dotted gray arrows) and volumetric effects such as scattering with defects, boundaries, and carriers, the physics of which are strongly modified in the ballistic ($L < \Lambda$) and mesoscopic regimes ($L < \lambda$) due to reduced dimensions.

The TBR due to material property mismatch is present even in classical conduction where $L \gg \Lambda, \lambda$, and is modeled by a temperature discontinuity boundary condition across the interface proportional to the heat flux,

$$q'' = (R_b)^{-1} (T^+ - T^-) \quad (1.6)$$

where R_b is the interface resistance, T^+ is the temperature on the “hot” side of the interface, and T^- is the temperature on the “cold” side of the interface. The impact of the abrupt change in geometry on the thermal boundary resistance depends on length scales. In the classical conduction regime, it creates a spreading resistance that is captured by the heat diffusion equation, Eq. (1.2) [10]. However, the TBR is strongly modified in the ballistic regime due to phonon constriction and scattering [11-14],

INTRODUCTION

requiring detailed solutions of the Boltzmann transport equation (BTE) [12, 14]. In the mesoscopic regime, the TBR is strongly augmented by modifications in the phonon spectra [11, 15], density of states mismatch [16], and phonon diffraction effects [11, 13, 17], typically requiring atomistic simulation approaches such as lattice dynamics calculations [16-19], non-equilibrium Green's functions (NEGF) calculations [20], or molecular dynamics calculations (MD) [21]. Understanding non-classical TBR is an active area of research and an objective of this work.

In the continuum transport regime, the volumetric contribution to the thermal resistance tends to scale strongly with length, $R_{vol} \sim L/k(L)$, where the intrinsic conductivity, $k(L)$, is a weak function of length. However, the TBR, R_b , tends to fall within a small range of values 10^{-7} - 10^{-9} m²K/W [22, 23], and depends weakly on length, as it is only a strong function of the properties within a mean free path of the interfaces. Consequently, there is a characteristic length scale $L_b \sim R_b \times k$ (Fig. 1.2) for a material below which the interface begins to dominate the total thermal resistance. For low conductivity materials such as SiO₂ $L_b \sim 20$ nm, whereas for a high conductivity material such as a CNT, $L_b \sim 20$ μ m. For most materials these length scale occur in the classical conduction regime. Thus, isolating individual contributions to the thermal resistance is critical in the thermal characterization and modeling of nanostructure materials, even when the thermal conduction is well approximated by classical behavior.

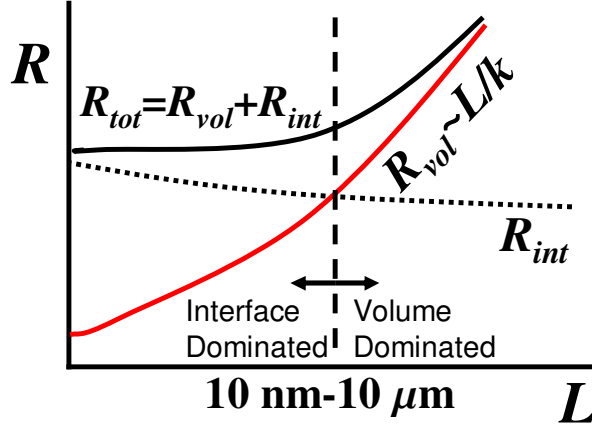


Figure 1.2: Schematic illustration of the relative magnitudes of volumetric and interface resistances as a function of length scale. As the length scale is reduced, the ratio of TBR to volumetric resistance increases, with the TBR becoming the dominant resistance. Such a transition can occur at length scales of microns for high conductivity materials (e.g. CNTs) down to ~ 10 nm for low conductivity materials (e.g. SiO_2).

1.2.3 Thermal Boundary Resistance

The understanding of TBR resulting from phonon transport through the interface between different materials is a relatively mature field for interfaces with lateral dimensions much larger than the phonon wavelength and mean free path [22, 24]. In this theory, the TBR results from the scattering of phonons at the interface, which impedes heat flow and creates a temperature discontinuity across the interface. The net energy flux carried by phonons across an interface in the presence of a temperature difference determines the interface conductance $h = (R_b)^{-1}$ —the inverse of the TBR. By summing the contribution from each phonon mode, assuming a small temperature difference across the interface (i.e. $(T^+ - T^-)/(T^+ + T^-) \ll 1$), as well as an isotropic phonon dispersion, the thermal boundary conductance between two three-dimensional materials, material 1 and material 2, can be expressed generally as [22, 24, 25],

INTRODUCTION

$$h = (R_b)^{-1} = \sum_p \frac{1}{2} \int_0^{\pi/2} \int_0^{\omega_{max}} \hbar \omega v_1(\omega, p) \cos(\theta) \alpha_{1-2}(\omega, p) g(\omega, p) \frac{\partial n}{\partial T} \sin(\theta) d\theta d\omega \quad (1.7)$$

where α_{1-2} is the spectral phonon transmission coefficient across the interface, θ is the angle between the phonon wavevector and the interface normal, g is the phonon density of states for branch p , and ω_{max} is the maximum phonon cutoff frequency. Assuming pure elastic scattering at the interface, ω_{max} is the lower of the maximum cutoff frequencies of the two materials (i.e. Debye frequency) [22]. However, allowing ω_{max} to range to the maximum Debye frequency can allow for implicit inelastic scattering [25], and allows for a more general interpretation of Eq. (1.7). Invoking the principle of detailed balance allows Eq. (1.7) to be evaluated in either material domain [22, 26].

Calculating the phonon transmission coefficient, α_{1-2} , requires the details of the phonon physics at the interface, which can be quite complicated. Thus, a variety of models have been developed to calculate α_{1-2} , which invoked several assumptions that are valid in different regimes and attempt to more accurately account for the interface transport physics [14, 16, 22, 24, 25, 27, 28]. The two most basic models are the acoustic mismatch model (AMM) and the diffuse mismatch model (DMM). The AMM model exploits the continuum behavior of long wavelength phonons and linear elasticity to calculate the transmission of the vibration mode energy across the interface [22, 24, 29], yielding a transmission coefficient [29],

$$\alpha_{1-2} = \frac{4 \rho_2 v_2 \cos(\theta_2) / \rho_1 v_1 \cos(\theta_1)}{\left(\rho_2 v_2 / \rho_1 v_1 + \cos(\theta_2) / \cos(\theta_1) \right)^2} \quad (1.8)$$

where ρ_i is the density of material i . The assumptions in the continuum approach are typically only valid at low temperatures (<10 K), where the phonon wavelength is much larger than the surface roughness and only the long wavelength phonons are strongly excited [22, 26]. By assuming the perfectly diffuse scattering at the interface

where the phonons loose all memory of their origin, the DMM attempts to extend the model to higher temperatures, where the dominant phonon wavelength is small compared to the surface roughness [22, 26]. These assumptions yield a phonon transmission coefficient given by

$$\alpha_{1-2} = \frac{\sum_p (v_{2,p})^{-2}}{\sum_p (v_{2,p})^{-2} + \sum_p (v_{1,p})^{-2}} \quad (1.9)$$

However, in practice, both the AMM and DMM yield similar values, which often deviate significantly from experimental data [22, 24]. More recently, attempts have been made to develop more advanced models for calculating α_{1-2} , valid at higher temperature, as well as with more realistic assumptions. These improvements have included the use of detailed lattice dynamic calculations [16, 19, 21], more accurate phonon density of states [24, 30], modifications in the AMM and DMM for more realistic surface scattering [27, 28], and the inclusion of inelastic scattering [25]. However, most of these approaches have focused on interfaces between three-dimensional materials, while relatively little work [31-34] has focused on developing models relevant for low dimensional interfaces. Consequently, one objective of this work is to develop a model for the interface conductance relevant for interfaces between low dimensional materials such as CNTs, molecular junctions, and other nanostructures.

1.3 Carbon Nanotubes as a Nanostructured Thermal Material

Carbon nanotubes can be described as a rolled-up sheet of graphene that forms a structure with one-dimensional translational symmetry along the CNT axis. Single wall nanotubes (SWNTs) consist of one individual rolled up graphene sheet while

INTRODUCTION

multi-wall nanotubes (MWNTs) consist of multiple concentric shells. While SWNTs typically have diameters below 5 nm, MWNTs can span much larger diameters, on the order of tens of nanometers, and consist of a wide range in number of inner shells.

Chirality describes the angle of the CNT axis with respect to the graphene lattice and can affect the CNT properties. The CNT structure and chirality are described through the chiral vector, which is directed circumferentially around the tube,

$$\mathbf{C}_h = n\mathbf{a}_1 + m\mathbf{a}_2 \quad (1.10)$$

where \mathbf{a}_1 and \mathbf{a}_2 are the graphene lattice vectors and (n,m) are integers with $0 \leq |m| \leq n$ restricted such that \mathbf{C}_h links coincidental lattice sites in the rolled up sheet. Figure 1.3 shows the arrangement of the SWNT with respect to the graphene lattice, along with common nanotube chiralities including zig-zag $(n,0)$ and arm chair (n,n) structures. The most dramatic effect of the tube chirality is in determining whether a tube is semiconducting or metallic. When $(2n+m)$ is divisible by three, the allowed reciprocal lattice vectors fall on the high symmetry points, and the tubes are metallic [35]. For a distribution of tubes with random chiralities, $\sim 2/3$ of the tubes are semiconducting, determined by the fraction of tubes that satisfy the metallic criterion.

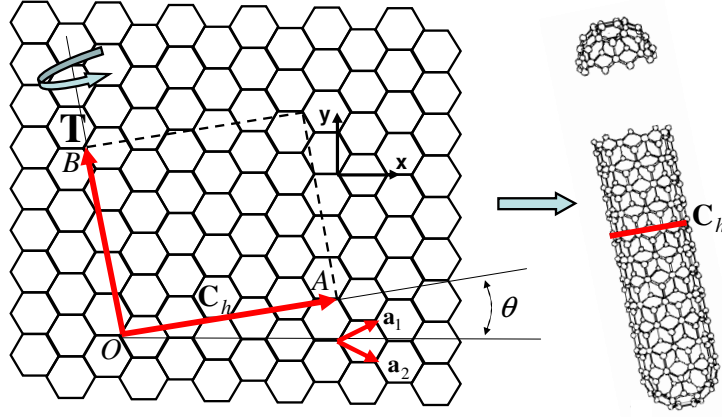


Figure 1.3: Carbon Nanotube Structure: Schematic of a 2-d graphene sheet. Carbon atoms are arranged in a honeycomb lattice with lattice vectors \mathbf{a}_1 and \mathbf{a}_2 . A carbon nanotube is a rolled up sheet of graphene, where the ends of the chiral vector are connected, the sheet becomes a tube, and the tube that is aligned with the translation vector, \mathbf{T} . The chiral vector is $\overline{OA} = n\vec{a}_1 + m\vec{a}_2$, where n and m are integers, and the nanotube chirality is described by (n,m) . The chiral angle, θ , is defined from the zigzag $(n,0)$ axis. Figures adapted from Saito et al. [35].

High expectations for the thermal conductivity of CNTs stem from the high in-plane thermal conductivity of graphite and the high thermal conductivity of diamond [36]. Phonon transport calculations and molecular dynamics simulations predicted individual CNTs to have extremely high room temperature thermal conductivities, in the range of $2500\text{-}6000 \text{ Wm}^{-1}\text{K}^{-1}$ [37-39]. Experimental measurements on individual CNTs seem to support these predictions, yielding similar values in the range of $2000\text{-}3600 \text{ Wm}^{-1}\text{K}^{-1}$ [4, 5, 40]. The geometry (length, diameter, and chirality), defect concentration, and temperature all influence the thermal conduction properties of individual CNTs. The thermal conductivity of an individual SWNT is given by

$$k_z = \sum_q \sum_p C_v(q,p) v^2(q,p) \tau(q,p) \quad (1.11)$$

INTRODUCTION

where k_z is the SWNT axial conductivity, q is the phonon wavevector in the first Brillouin zone of the one-dimensional SWNT Bravais lattice, p is the phonon branch, v is the phonon group velocity, τ is the phonon lifetime, and C_v is the volumetric heat capacity of the phonon mode p with wavevector q . The high thermal conductivity of CNTs is due to the combination of large acoustic phonon group velocities originating from the stiff interatomic carbon bonds and long phonon lifetimes. As with nanowires in general, SWNTs have four acoustic modes [41, 42]: one longitudinal ($v_L=20,000$ m/s), one torsional ($v_{TW}=15,000$ m/s), and two quadratic bending modes with quadratic dispersion relations [41, 43]. The total phonon lifetime is due to a combination of Umklapp scattering, boundary scattering, and scattering with defects. Combining these effects using Matthiessen's rule yields a total scattering rate of

$$\tau^{-1}(\omega) = \tau_U^{-1}(\omega) + \tau_{BC}^{-1}(\omega) + \sum_{i=1}^{N_d} \tau_{D,i}^{-1}(\omega) \quad (1.12)$$

where τ_U is the lifetime for Umklapp processes, τ_{BC} is the lifetime for interface scattering, and $\tau_{D,i}$ is the lifetime for scattering with the i^{th} defect. For pristine tubes with sufficient length that boundary scattering is unimportant, the phonon lifetime is dominated by Umklapp scattering processes, which yield longer phonon lifetimes compared to those in graphene and other materials—up to hundred picoseconds at room temperature [44]—due to the geometry of the SWNT reducing the number of allowed states into which phonons can scatter [44, 45]. These long lifetimes combined with the high acoustic phonon group velocity yield large phonon mean free paths on the order of $1 \mu\text{m}$ [44, 46]. Since many applications, devices, and experiments employ CNTs with lengths on the order of the phonon mean free path, considering ballistic conduction effects is often important, even at elevated temperatures. Consequently, thermal transport in CNTs is often dominated by interface scattering, for which there is currently incomplete understanding.

Similarly, the confined transverse geometry and high acoustic phonon velocities in CNTs can affect the volumetric and interface properties of CNTs by magnifying the

wave nature effects of phonons, generating mesoscopic effects even at modest temperatures (~ 100 K). The dominant phonon wavelength is given by [43]

$$\lambda_d = \frac{h\nu}{2.6k_bT} \quad (1.13)$$

where λ_d is the dominant phonon wavelength, h is Planck's constant, k_b is Boltzmann's constant, T is the temperature, and ν is the phonon velocity. At 300 K, Eq. (1.13) yields a dominant phonon wavelength of ~ 1.3 nm, which is comparable to the diameter of many SWNTs. Consequently, wave nature effects such as phonon confinement and interference can be significant even at elevated temperatures as compared to other materials which have lower phonon velocities and larger critical dimensions. The phonon confinement impacts the thermal transport properties by creating sub-bands and modifying the density of states [47]. As there is currently little work aimed at understanding these mesoscopic effects on TBR, a goal of this work is to develop a better understanding of these resistances of low dimensional interfaces.

Extrapolating the thermal conductivity of individual nanotubes to bulk CNT materials, such as films formed from aligned arrays of CNTs, predicts thermal conductivities rivaling those of metals, even at low CNT densities (1-10 %vol.). However, achieving these high thermal conductivities of bulk CNT materials in practice has proved challenging. Compared to individual tubes, such films are complicated by thermal interfaces, partial CNT engagement, nanoscale conduction resistances due to reduced dimensionality, and reduced CNT quality [48]. Since most bulk CNT materials have thicknesses greater than tens of microns, modeling the tube as diffusive conductors is a reasonable approximation under many circumstances. However, because of the high thermal conductivities of the individual constituent tubes, the thermal interface resistance of individual CNT contacts can contribute a significantly to the total thermal resistance, even in films with thicknesses much above the phonon mean free path. Similarly, the aggregate effect of nanoscale conduction and interface resistance effects are critical in determining the macroscopic thermal

properties. Reducing these additional contributions to the volumetric thermal resistance of bulk CNT films is a critical problem in achieving high thermal performance material, and would enable their application in many areas such as in advance thermal management materials.

1.4 Application of CNT Arrays: Advance Thermal Management Materials

The excess heating generated by energy dissipation in electronic components such as microprocessors can degrade their performance and lead to premature device failure. Thus, the efficient removal of heat from the device to the ambient environment through electronic component packaging materials is critical in maintaining device temperatures at acceptable levels. Figure 1.4 illustrates an example thermal conduction pathway in a common packaging configuration for a microprocessor. These conduction pathways can contain several interfaces between materials (e.g. interfaces between die and heat spreader, and heat spreader and heat sink) that consume a significant portion of the thermal resistance budget. Placing thermal interface materials (TIMs) such as thermal greases or solder in the interface is a common approach to reduce the interface resistance by filling in the surface asperities that significantly reduce the effective cross-sectional area contributing to conduction [49]. The total resistance of the TIM is the sum of the interface resistances and the volumetric contribution, which depends on the TIM thermal conductivity and the bond line thickness (BLT). As the power generation densities continue to increase, and if there are no further advancements in TIM technology, the thermal interface resistance will continue to contribute to an increasing portion of the thermal budget, potentially saturating it within the next few years [50]. Future TIM advancements will need to achieve total thermal resistance below the current state-of-the-art value of $\sim 0.05 \text{ cm}^2\text{K/W}$.

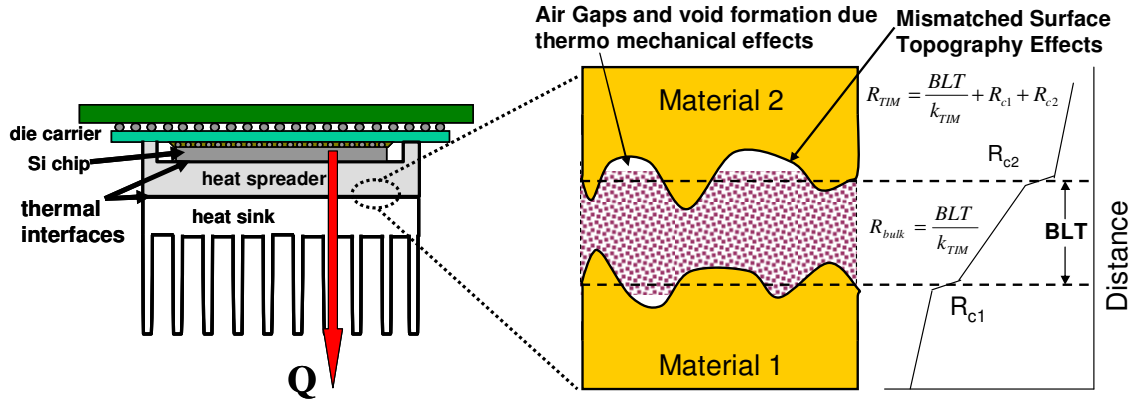


Figure 1.4: Illustration of thermal conduction pathways in a common configuration for a microprocessor and its packaging. The thermal interface resistances along the pathway from the generation region within the device to the ambient environment constitute a significant fraction of the thermal budget. The TIM material increases the real contact area by conforming to the surface topography. The total resistance of the TIM is the sum of its interface resistances with the two materials and the volumetric contribution, which depends on the TIM thermal conductivity and the bond line thickness (BLT). Figure adapted from reference [49].

Effective thermal interface materials must meet a variety of criteria, including maintaining a low total thermal resistance and compliance to accommodate surface topography and thermal expansion mismatch over the thermal cycling lifetime of the material. Achieving such a combination of materials properties is often challenging since inter-atomic bonding correlates stiffness and thermal conduction. Figure 1.5 illustrates the relation between the total thermal resistance and elastic modulus of common TIM materials such as solders and thermal greases. While solders such as indium can achieve resistances of $0.03 \text{ cm}^2\text{K/W}$, their stiffness generates stresses during thermal cycling that degrade their performance [49]. Thermal greases offer increased compliance, but at the expense of increased thermal resistances.

Engineering materials with nanofeatures such as carbon nanotubes and nanoparticles can provide an opportunity to achieve low resistance combined with a low elastic

INTRODUCTION

modulus. For example, prior work with Ni/CNT suspensions in silicone oil showed anomalous conductivity enhancements of $\sim 5\times$ [51], suggesting the potential for significant improvements in conductivity with the inclusion of nanoparticles. The excellent thermal conductivity of individual nanotubes, as well as their bending compliance due to their large aspect ratio, makes aligned arrays of nanotubes very promising as advance TIMs, with the potential to achieve resistances below $0.01 \text{ cm}^2\text{K/W}$ [48]. While initial measurements of the thermal resistance of aligned MWNT arrays yielded total resistances competitive with conventional interface materials ($\sim 0.15 \text{ cm}^2\text{K/W}$) [52], the results suggested that interfaces reduced the performance of the films compared to theoretical predictions. Consequently, the impact of the interface resistance in CNT films is a critical issue in improving their performance. Furthermore, there are little data for their mechanical properties (e.g. elastic modulus) and the impact of thermal cycling on the CNT film thermal properties. Providing such data is critical for the advancement of nanostructured TIMs.

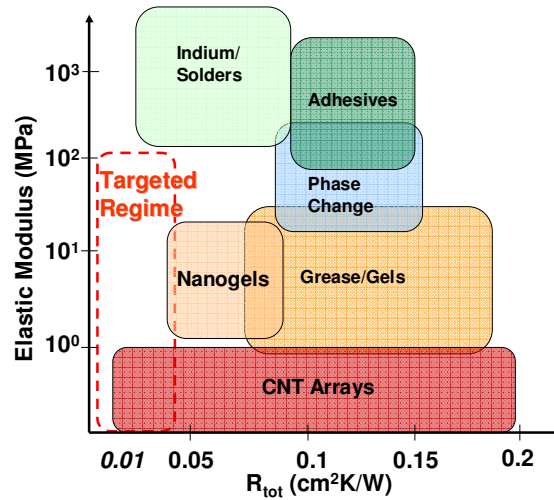


Figure 1.5: Illustration of the relation between total thermal resistance and elastic moduli of common TIM materials such as solder and greases. With conventional materials, reduced resistances often come at the expense of increasing elastic modulus, which reduces reliability and increases thermal degradation during thermal cycling. Engineering materials with nanofeatures such as carbon nanotubes or nanoparticles offers the possibility of achieving materials with reduced resistances, potentially

below $0.01 \text{ cm}^2\text{K/W}$, while maintaining compliance. Representative material properties taken from literature [49].

1.5 Thermal Characterization Needs for Nanostructured Materials

The high density of interfaces and reduced dimensions complicate conduction in nanostructured materials. Thus, understanding conduction and the thermal properties of these materials require metrology techniques that can resolve the distribution of thermal properties, often requiring the confinement of temperature gradients to sub-micron dimensions. Achieving such confinement of temperature gradients typically requires establishing ultrafast temperature fields in the material and measuring the resulting temperature response to infer thermal properties. Traditional long-time-scale approaches such as steady-state finite difference offer insufficient resolution in time, and hence space, to accurately separate the various contributions to the interfaces. Even advanced transient electrical techniques such as 3ω [53] are practically limited to measuring temperature transients on the order of $\sim 10 \mu\text{s}$, yielding temperature gradients extending over $1 \mu\text{m}$ for many materials. To achieve the required spatial resolution in thermal properties necessary to characterize nanostructured materials typically requires ultra-fast optical techniques such as pump-probe and thermoreflectance approaches [54]. A key contribution of this work is the development of ultrafast optical characterization techniques for measuring the thermal properties of CNT and ultrathin films.

1.6 Scope of Work

This work has three primary goals and contributions to the field. The first objective of this work is the development of ultra-fast optical metrology systems (nanosecond thermoreflectance and picosecond time-domain thermoreflectance (TDTR)) and conduction models suitable for measuring and understanding the thermal interface resistances in nanotube and ultra-thin films. These systems are used for 1) measuring the thermal resistances in metal-coated SWNT arrays; 2) studying the impact of metallization on the thermal resistance of metal-coated SWNT arrays; 3) studying the temperature dependence of phonon conduction in SWNT films; 4) providing data for the growth interface resistance in MWNT arrays; and 5) measuring the relative contribution of interface and volume resistances in ultra-thin HfO₂ films. These data are presented in conjunction with novel models for conduction within the CNT array for interpreting data and extracting the contact resistance of individual nanotubes.

The second objective of this work is the development of new theoretical models for conduction resistances between low dimensional materials and semi-infinite contacts. These models specifically account for the modification in the phonon spectra due to the abrupt change in geometry present in dimensionally mismatched contacts.

The third goal of this work is the advancement of CNT-based TIMs to maximize their performance. A novel CNT-solder tape is proposed as a potential solution and thermal performance data are provided.

1.7 Organization

This dissertation is organized into the following five chapters:

CHAPTER 1

Chapter 1 provides introductory, background, and motivational material for this dissertation.

Chapter 2 develops the nanosecond thermoreflectance technique and applies the technique to the characterization of aligned SWNT arrays and their interfaces. The work develops a model for nanoscale conduction in CNT films to interpret thermal data. The work studies the temperature and composition dependences of the thermal properties of metal-coated SWNT arrays. Data are provided for a proposed thermal tape structure to maximize the thermal performance of CNT-based TIMs.

Chapter 3 develops a picosecond time domain thermoreflectance (TDTR) technique suitable for the direct measurement of the thermal resistance of the growth interface of MWNT films through transparent substrates and presents data for the interface resistance.

Chapter 4 develops a theoretical lattice dynamics Green's function model for phonon transmission and the interface resistance between dimensionally mismatched materials, relevant for understanding conduction in low dimensional nanostructure contacts.

Chapter 5 applies the picosecond TDTR technique to measure the interface and volume resistance in ultra-thin HfO₂ films that include nanoparticles. The thermal properties are interpreted in terms of traditional interface resistance models and phonon scattering within the film.

Chapter 6 summarizes this work and offers suggestions for future work.

Chapter 2

Thermal Characterization of Metal-coated Aligned Nanotube Arrays

2.1 Thermal Properties of Metal-Coated Vertically-Aligned Single-Wall Nanotube Arrays

2.1.1 Introduction

The outstanding thermal properties of carbon nanotubes (CNTs), particularly their extraordinary thermal conduction properties, have generated considerable interest and research activity. Past work investigated the thermal properties of individual single wall nanotubes [4, 37-39, 55-59], multiwalled nanotubes [40, 60], bulk films of nanotubes [61, 62], nanotube composites [51, 63-67], and aligned arrays of mulitwalled nanotubes [52, 68, 69]. A very promising application is the use of vertically-aligned arrays of carbon nanotubes as thermal interface materials (TIMs) for electronic systems. Thermal interface materials require a high thermal conductivity, a low thermal interface resistance with the adjacent microprocessor and heat sink, as well as significant mechanical compliance to help minimize the impact of mismatched thermal expansion coefficients. Many thermal interface materials, such as particle-filled organics and related composites, offer excellent mechanical compliance with the penalty of relatively poor thermal conductivity. Other materials, such as alloyed metals and eutectics, offer relatively good thermal conduction properties with the penalty of poor mechanical compliance and reliability concerns related to thermal cycling. Carbon nanotube films, which consist of many flexible nanotubes, may

eventually provide both high thermal conductivity and lateral compliance, a truly unique combination of properties that could be very attractive for interfaces in electronic systems. However, past work has suggested that the thermal performance of CNT films is impeded by high thermal interface resistances, indicating that more detailed measurements and improved fabrication methods will be needed.

The thermal conductivity of individual single wall CNTs (SWNTs) and multiwall CNTs (MWNTs) has been the subject of recent theoretical and experimental research activity. Experimental and molecular dynamic studies have yielded room temperature thermal conductivities of individual SWNTs ranging from 2500 to 6600 $\text{Wm}^{-1}\text{K}^{-1}$ [4, 37-39]. For MWNTs past research yielded similar values ranging from 2000 to 3000 $\text{Wm}^{-1}\text{K}^{-1}$ [40, 60]. Theoretical works predict that ballistic transport effects, interface scattering, and modification to the phonon modes in sub-micron length individual SWNTs tend to reduce their thermal conductivity to values below 350 $\text{Wm}^{-1}\text{K}^{-1}$ [55-59]. Likewise, measurements of bulk CNT films yielded lower thermal conductivities in the range of 20-200 $\text{Wm}^{-1}\text{K}^{-1}$ [61, 62]. The discrepancy between the thermal conductivities of individual CNTs and their value in bulk films can be attributed to various effects. In particular, tube-tube contact, tube-matrix contact, and an increased defect density due to bulk film preparation methods may reduce the phonon mean free path compared to its value in individual tubes. The tube-matrix contact has been the focus of several studies [63, 64, 70]. Furthermore, the defined area of heat flow through the nanoscale geometries of both the individual constituent tubes and of the film itself is often ambiguous and subject to variation, directly influencing the reported values of CNT thermal conductivities. This problem is particularly acute with MWNT films, which often exhibit significant variations in individual tube cross sectional areas within a film.

Although the bulk thermal performance of CNT films falls short of the theoretical expectations, the use of carbon nanotubes as fillers in advanced thermal interface materials (TIMs) and in nanostructured composite films greatly improves the thermal performance of the material. A CNT volume fraction of 1% showed an increase in the

effective thermal conductivity of 2.5 in silicon oil [65] and 125% for epoxy [66]. Similarly, by suspending SWNTs randomly oriented in a PMMA composite, Guthy *et al.* [67] measured a thermal conductivity enhancement that saturated at 240% for 6vol% SWNTs. Additionally, Hu *et al.* [51] combined CNTs with traditional nickel fillers, creating a seven-fold increase in the effective thermal conductivity of the base fluid, twice that of nickel nanoparticle filler alone.

Other investigations showed that creating vertically-aligned CNT films better utilizes the outstanding thermal conductivity of individual CNTs. Using the 3 ω method, Hu *et al.* [52] measured the room temperature thermal conductivity of a 13 μm thick vertically-aligned MWNT film grown on silicon to be $75 \text{ Wm}^{-1}\text{K}^{-1}$, which outperforms that of randomly oriented tube samples. However, the total thermal resistance of the aligned CNT TIM was found to be $16 \text{ m}^2\text{KMW}^{-1}$, which still falls well short of theoretical expectations. Yang *et al.* [68] performed a similar measurement of MWNT films using a thermoreflectance technique, and found the effective thermal conductivities to be around $15 \text{ Wm}^{-1}\text{K}^{-1}$, with total thermal resistances falling in the range of $0.8\text{-}2.9 \text{ m}^2\text{KMW}^{-1}$. Even accounting for porosity effects, the reduced performance of these aligned MWNT films indicates the thermal boundary resistance between the CNT and substrate is the problem.

Much of the variation observed in the previous data can be attributed to the impact of thermal interface resistances in carbon nanotube films. The relative importance of thermal interface resistance in CNT based TIMs was recently confirmed by Tong *et al.* [69] in a transient phase sensitive photothermal measurement of an aligned MWNT TIM. The TIM was formed by dry adhesion of a 7 μm thick MWNT array, grown on a Si wafer, to a glass plate. The total resistance of the TIM was measured to be $12 \text{ m}^2\text{KMW}^{-1}$, which was dominated by the dry glass interface resistance of $11 \text{ m}^2\text{KMW}^{-1}$. The importance of the thermal interface resistance in CNT arrays motivates its further study as well as the need for metrology that focuses on this property.

In this work, we measure and model the room temperature thermal properties of a 28 μm thick metal-coated vertically-aligned SWNT film using a nanosecond thermorefectance technique. Our objective is to extract, model, and illuminate the governing physics of the interface resistance. A 6 nanosecond heating pulse from a frequency doubled Q-switched Nd:YAG laser generates a transient temperature field in the metalized film, and the combination of sub-microsecond laser-reflectance thermometry and effective medium modeling extract the vertical distribution of area-averaged thermal properties in the system. The transient timescales of the measurement provide a means to separate the relative importance of thermal resistance within the film from those of the film boundaries. Isolating the thermal boundary resistances and measurement of the CNT volumetric heat capacity enables an understanding of the low measured effective thermal conductivity of the aligned SWNTs. This work provides insight into the physical mechanisms governing the thermal resistance in aligned CNT films, which will enable innovations in fabrication technology to reduce the total thermal resistance and lead to promising interface materials.

2.1.2 Experimental Method

2.1.2.1 Sample Preparation

The aligned SWNT sample was prepared as follows. First, an iron film 1-2 \AA thick is deposited using electron beam evaporation on a 10 nm thick thermal oxide layer grown on the silicon substrate. Subsequent annealing in oxygen at 550 $^{\circ}\text{C}$ produced a monolayer of ~ 1.3 nm diameter iron clusters to act as catalysts for the CNT growth. The CNT synthesis was carried out in a coupled-RF CVD plasma system with a mixture of methane, hydrogen, and oxygen. Additional details of the CNT growth process are discussed in Ref. [71].

THERMAL CHARACTERIZATION OF METAL-COATED ALIGNED NANOTUBE ARRAYS

The SEM profile of the sample in Fig. 2.1a shows that the tube length is 28 μm . Raman data [71] indicate that the SWNT diameter, d , ranges between 1-2 nm, with the average being close to the average catalyst diameter of ~ 1.3 nm. Since the SWNT growth conditions yield approximately one nanotube per iron catalyst cluster [71], we estimate the SWNT number density to be $8.7 \times 10^{16} \text{ m}^{-2}$ based on the thickness of the deposited catalyst layer and cluster diameter after annealing. This number density corresponds to a volume fraction of $\sim 12\%$ based on the average SWNT annular area, $A_a = \pi db$, where we use an average diameter of $d = 1.3$ nm, and $b = 3.4 \text{ \AA}$, the thickness of a graphene plane. A pre-metalization topographic profile, produced by scanning AFM, of the top of the CNT film is shown in Fig. 2.1b and indicates that the RMS roughness of the film is ~ 60 nm.

Prior to the evaporation of the 160 nm thick aluminum film, an initial evaporation of a 20 nm thick palladium film on the exposed CNT ends enhances the metal-CNT contact interface. An SEM image (Fig. 2.1c) of the top of the metal film taken after deposition shows that the surface is rough and porous on the sub-micron scale. The potential effects of the film porosity on its optical properties will be considered in the following section.

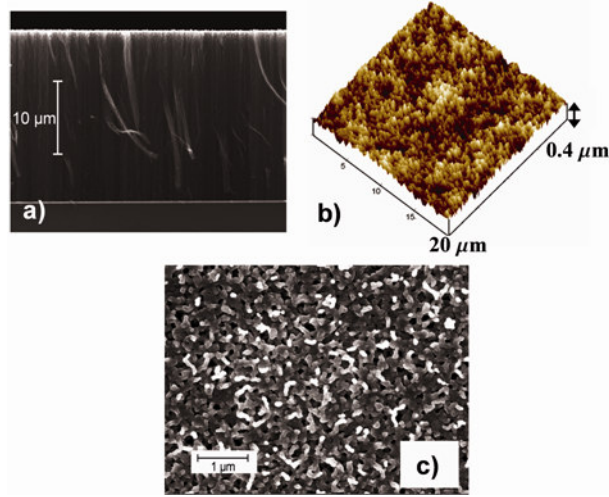


Figure 2.1: a) SEM profile of aligned SWNTs grown on Si—the tube length is 28 μm . The SWNT diameter ranges between 1 nm and 2 nm, with an average of approximately 1.3 nm. b) AFM topographic profile of the top of the CNT film, which indicates that the RMS surface roughness is ~ 60 nm. c) SEM of top of the metal film after it has been deposited on CNTs. The image shows that the metal film is porous at a scale below 100 nm.

2.1.2.2 Experimental Setup and Procedure

The thermal properties of the metallized SWNT film are measured using a thermoreflectance technique in which a high power pump laser induces a transient temperature field in the metal film. The reflected intensity of a second low power CW probe laser, being proportional metal temperature, provides a dynamic measurement of the temperature response of the metal film. The thermoreflectance technique has been used in the nanosecond regime to characterize the thermal properties of thin films [68, 72, 73], in the picosecond regime to measure both the thermal properties of thin films and their interfaces [74-76], and in the femtosecond regime to measure electron and phonon processes [77, 78].

THERMAL CHARACTERIZATION OF METAL-COATED ALIGNED NANOTUBE ARRAYS

Figure 2.2 is a schematic of the optical path and experimental configuration along with a schematic of the sample geometry. A 650 MHz photodiode and amplifier measures the reflected intensity of a 10 mW diode laser at 637 nm wavelength that is focused on the sample with a spot size of approximately 10 μm . The metal film on top of the CNTs is heated using a 10 Hz, 6 ns pulse width Nd:YAG laser, frequency doubled to 532 nm.

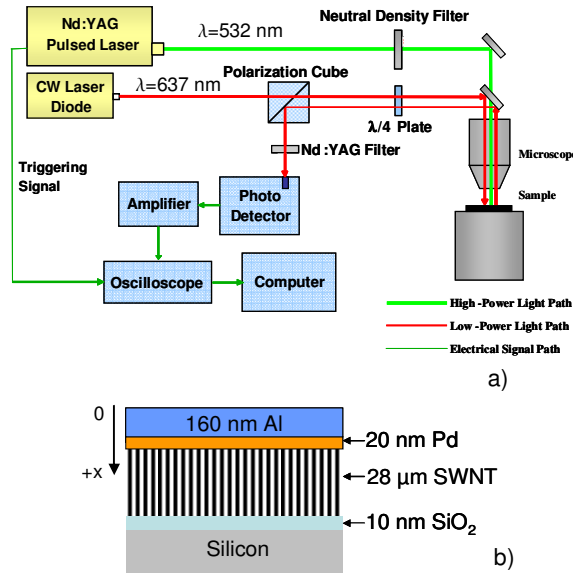


Figure 2.2: a) Schematic of the thermoreflectance thermometry experimental setup including the optical and signal paths. b) Schematic of sample geometry. The initial deposition of 20 nm thick layer of palladium on the SWNT ends forms an adhesion layer with the 160 nm thick aluminum film used for thermal reflectance thermometry.

The transient metal temperature is measured through the temperature dependence of its dielectric constant [79]. The linearized temperature dependent reflectivity [80], defines the thermoreflectance coefficient, C_{tr} , as

$$\frac{\Delta R}{R_0} \equiv C_{tr} \Delta T \quad (2.1)$$

where R_0 is a reference reflectivity and T is the metal temperature. Since for most metals, C_{tr} is approximately constant [79, 81], the reflected probe intensity is proportional to the metal surface temperature.

The surface topography and porous structure of the metalized CNT films poses significant challenges for photothermal diagnostics. Due to porosity, the optical radiation may be absorbed on both the surface of the metal film and in its pores. However, since all thermal diffusion time scales in the aluminum film are sub-nanosecond and below the temporal resolution of the equipment, it is inconsequential whether the radiation is absorbed strictly on the metal surface or within the pores of the metal layer.

The transmission of optical radiation through the metal may lead to the possibility of energy absorption in the structure underlying the film, complicating the solution to the heat diffusion equations. Data from image analysis of the SEM image in Fig. 2.1c bounds the potential un-metalized regions to less than 5%. The sub-wavelength of nature of the pores further reduces the transmitted radiation by a factor of $(r/\lambda)^4$ [82, 83], where r is the hole radius, yielding a net energy transmission factor less than 5×10^{-4} . Furthermore, the near field radiation is appreciable only within $\sim 4r$ [83] of the hole, and is thus much less than the thermal diffusion distance ($\sim 4 \mu\text{m}$) into the CNT film during the laser pulse. These conclusions render the transmission of optical radiation through the metal film insignificant.

The relatively large surface roughness of the metal film ($\sim 100 \text{ nm}$) augments absorption such that care must be taken to avoid damage and delamination. The mechanical compliance, porosity, and mismatched thermal expansion behavior of the metal coating and underlying CNT film may lead to significant temperature induced changes in the surface topography and associated thermorefectance coefficient. The value of C_{tr} may also be influenced by microstructural changes in the metal film with

temperature, which are related to the reflectivity through electron scattering and the plasma frequency.

We address the above concerns about photothermal interaction with the film through a strong reduction in the heating laser fluence and careful verification that C_{tr} is constant and reproducible in the temperature range of the measurement. For different laser powers, the normalized thermal response trace collapsed to a single shape that depends only on the thermal properties within the structure. Furthermore, the amplitude of the peak reflected probe intensity scaled in direct proportion to the pump power. These results indicate that interaction of the metal with both lasers is linear and reproducible.

2.1.2.3 Data Extraction Model and Method

To extract the thermal properties of the CNT film, we fit the experimentally measured thermal response to an analytical solution of the heat diffusion equation based on effective area-averaged thermal properties. As long as heat is fully absorbed by the metal layer, and is forced to conduct through the CNT film and into the substrate, the solution of the heat diffusion equation using effective area-averaged properties is a fully rigorous mathematical treatment of the physics and does not require knowledge of the CNT volume fraction. Solving the heat diffusion equation reduces to a 1D problem since the diameter of the heating pulse ($d \sim 6$ mm) is much greater than any of the thermal diffusion distances into the structure during the measurement. The governing equation in each layer is

$$\frac{\partial T_j(x, t)}{\partial t} - \alpha_j \frac{\partial^2 T_j(x, t)}{\partial x^2} = 0 \quad (2.2)$$

where T_j is the temperature and α_i is the thermal diffusivity of the j^{th} material. We solve the 1D heat diffusion equation by transforming Eq. (2.2) to the frequency domain

$$\frac{\partial^2 \theta_j(\omega, x)}{\partial x^2} + \frac{i\omega}{\alpha_j} \theta_j(\omega, x) = 0 \quad (2.3)$$

where θ_j is the Fourier transform of the temperature field, and which has the general solution

$$\theta_j(\omega, x) = a_j(\omega) e^{i\sqrt{\frac{i\omega}{\alpha_j}}x} + b_j(\omega) e^{-i\sqrt{\frac{i\omega}{\alpha_j}}x} \quad (2.4)$$

The laser heating is modeled as a heat flux boundary condition on top of the metal film with a Gaussian shaped heat pulse

$$q''_{laser}(t) = -k_{Al} \left. \frac{\partial T_{Al}(t, x)}{\partial x} \right|_0 \quad (2.5)$$

$$q''_{laser}(t) = \sqrt{\frac{1}{\pi \tau^2}} \rho_{Al} L_{Al} c_{p,Al} \Delta T_{max} e^{-\frac{t^2}{\tau^2}} \quad (2.6)$$

where τ is the e^{-1} laser pulse width (6 ns), ΔT_{max} is the peak temperature change, k_{Al} , ρ_{Al} , L_{Al} , and $c_{p,Al}$ is the aluminum thermal conductivity, density, thickness, and heat capacity, respectively. The silicon wafer is assumed to be semi-infinite since the thermal diffusion time through the silicon is much larger than the microsecond timescale of the measurement.

The interfaces between the aligned CNT film and both the metal film and the SiO_2 film provide four boundary conditions:

$$q''_{Al-cnt} = (R''_{cnt-Pd,eff})^{-1} (T_{Al}(L_{Al}) - T_{cnt}(0)) = -k_{Al} \left. \frac{\partial T_{Al}}{\partial x} \right|_{L_{Al}} \quad (2.7)$$

$$-k_{Al} \left. \frac{\partial T_{Al}}{\partial x} \right|_{x_{Al}=L_{Al}} = -k_{cnt,eff} \left. \frac{\partial T_{cnt}}{\partial x} \right|_{x_{cnt}=0} \quad (2.8)$$

$$q''_{cnt-SiO_2} = (R''_{cnt-SiO_2,eff})^{-1} (T_{cnt}(L_{cnt}) - T_{SiO_2}(0)) = -k_{SiO_2} \frac{\partial T_{SiO_2}}{\partial x} \Big|_{x_{SiO_2}=0} \quad (2.9)$$

$$-k_{cnt,eff} \frac{\partial T_{Al}}{\partial x} \Big|_{x_{cnt}=L_{cnt}} = -k_{SiO_2} \frac{\partial T_{SiO_2}}{\partial x} \Big|_{x_{SiO_2}=0} \quad (2.10)$$

where $k_{cnt,eff}$ is the area-averaged CNT thermal conductivity and $R''_{cnt-Pd,eff}$ and $R''_{cnt-SiO_2,eff}$ are the area-averaged contact resistances between the CNTs and the palladium adhesion layer and oxide films, respectively. We define the resistance at the metalized contact as $R''_{cnt-Pd,eff}$ because the nanotubes directly contact the palladium adhesion layer underlying the aluminum film. An inverse Fourier transform converts the frequency domain solution back to the time domain, which we then fit to the experimental thermal data using a least squares curve fit algorithm.

Fitting the thermal model to the measured data is an inverse heat transfer analysis requiring the simultaneous fit of the four unknown parameters in the governing equations: $k_{cnt,eff}$, $C_{cnt,eff}$ (through $\alpha_{cnt,eff}$), $R''_{cnt-Pd,eff}$, and $R''_{cnt-SiO_2,eff}$. The impact and sensitivity of variation in each parameter on the shape of the thermal response is unique and evident at different time scales because each appears in a unique way through the governing equations, Eq. (2.3) and Eqs. (2.7)-(2.10), and is localized in the vertical direction. Since the measurement is capable of resolving time scales below the thermal diffusion time through the CNT film, these properties can be accurately and individually resolved. We verified this capability by a mathematically rigorous parametric variation study of the best-fit solution of the heat diffusion equation to the experimental data.

2.1.3 Results and Discussion

Fig. 2.3 shows a representative thermal response for the sample along with the least squares best-fit analytical solution evaluated with the average of the extracted properties. Nine measurements at multiple locations on the samples and at multiple

laser pump powers were individually fit to the analytical heat diffusion model and the effective parameters were averaged to produce the results shown in Table 2.1. Table 2.1 shows the corresponding RMS error in the data, which is dominated by variations in the shape of the trace and uncertainty due to amplitude noise. Errors due to the sensitivity of the least squares fitting algorithm applied to a single thermal response trace generally contribute less than 10% error for each parameter.

Table 2.1: Best-fit values averaged from multiple measurements of $C_{cnt,eff}$, $R''_{cnt-Pd,eff}$, $R''_{cnt-SiO2,eff}$, and $k_{cnt,eff}$ for the 28 μm thick sample along with their associated uncertainty. The uncertainty is calculated from the RMS variation in extracted parameters individually fit to multiple measurements.

Parameter	Average Result	% Uncertainty
$C_{cnt,eff}$	5.2 $\text{KJm}^{-3}\text{K}^{-1}$	12%
$R''_{cnt-Pd,eff}$	2.9 $\text{m}^2\text{K}^1\text{MW}^{-1}$	21%
$R''_{cnt-SiO2,eff}$	9.1 $\text{m}^2\text{K}^1\text{MW}^{-1}$	31%
$k_{cnt,eff}$	$> 8 \text{ Wm}^{-1}\text{K}^{-1}$	—

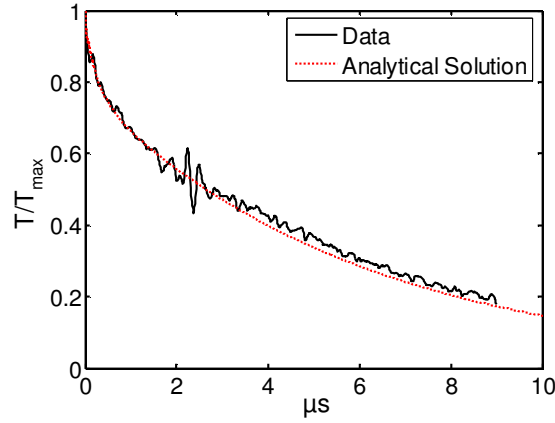


Figure 2.3: Typical thermal response trace data for a particular measurement (solid) for 28 μm sample along with the best fit analytical solution evaluated with the average best fit parameters summarized in Table 2.1 (dashed). The data show two characteristic decay time scales during the measurement: the initial rapid decay lasting $\sim 0.5 \mu\text{s}$ followed by a longer decay lasting $\sim 4 \mu\text{s}$.

An estimate of the thermal diffusion time through the CNT film qualitatively explains the particular shape of the thermal trace in Fig. 2.3, which displays an initial rapid decay lasting $< 0.5 \mu\text{s}$ followed by a second, slower decay lasting $\sim 4 \mu\text{s}$. The characteristic thermal diffusion time through the SWNT film is given by $t_{\text{diff}} = L_{\text{cnt}}^2 / \alpha_{\text{cnt}}$, where $L_{\text{cnt}} = 28 \mu\text{m}$ is the thickness of the CNTs, and α_{cnt} is the individual CNT thermal diffusivity. From the measurement of $c_p = 660 \text{ mJg}^{-1}\text{K}^{-1}$ by Hone *et al.* [47] and the CNT unit cell volume, we estimate $C_{v,a}$ to be $1.5 \text{ MJm}^{-3}\text{K}^{-1}$, which is the volumetric heat capacity for an individual SWNT compatible with the area definition $A_a = \pi db$. Combined with a value of $k_{\text{cnt}} = 3600 \text{ Wm}^{-1}\text{K}^{-1}$ [4], yields $\alpha_{\text{cnt}} \sim 2.4 \times 10^{-3} \text{ m}^2\text{s}^{-1}$ and $t_{\text{diff}} = 0.33 \mu\text{s}$, which is in reasonable agreement with the time scale for the initial rapid decay demonstrated by the data. Consequently, the initial decay rate for times less than t_{diff} is relatively insensitive to the CNT-oxide contact resistance. A rigorous parametric variation study of the fitting parameters in the analytical model verified that the initial rapid decay rate is dominated by $R''_{\text{cnt-Pd,eff}}$ and that $R''_{\text{cnt-SiO2,eff}}$ dominates the long-time decay characteristics.

Due to the large effective thermal interface resistances in the structure, the measurement only yields a potential lower bound of $\sim 8 \text{ Wm}^{-1}\text{K}^{-1}$ for the area-averaged thermal conductivity of the array, which corresponds to a total CNT resistance below $\sim 3.5 \text{ m}^2\text{KW}^{-1}$. No solution fit was attainable for thermal conductivities lower than this value, and the fit of the remaining parameters to the data trace was insensitive to conductivities at and above this value.

The data in Table 2.1 show that the effective CNT heat capacity is quite low, even accounting for the nanotube film porosity. Because the heat capacity is expected to be relatively insensitive to interface effects, the data suggest that only a fraction of the CNTs contribute to the volumetric specific heat. The ratio of the measured effective heat capacity to the volumetric heat capacity of an individual tube ($f_{eff,C}$) provides an estimate of the effective volume fraction of CNTs contributing to the thermal capacity in the structure,

$$f_{eff,C} = \frac{C_{cnt,eff}}{C_{v,a}} = 0.0035 \quad (2.11)$$

which includes the contributions to the porosity occurring within an individual tube and does not require precise knowledge of the SWNT diameter. Based on an estimated average nanotube diameter of 1.3 nm, $f_{eff,C}$ corresponds to number density of $2.5 \times 10^{15} \text{ m}^{-2}$, which is much less than the prior estimate of the SWNT yield based on the catalyst preparation conditions. A thermal model for transport within the nanotube structure presented in the subsequent section concludes that the effective volume fraction of CNTs contributing to the thermal resistance in the CNT array ($f_{eff,R}$) is nearly identical to $f_{eff,C}$. Scaling the lower bound on the area-averaged effective CNT thermal conductivity by this fraction provides an estimate of $\sim 2300 \text{ Wm}^{-1}\text{K}^{-1}$ for the lower bound on the intrinsic conductivity of an individual SWNT measured in this study.

Since the CNT thermal resistance is small in comparison to the interfaces contributions, the total effective thermal resistance of the SWNT structure is determined by the sum of the boundary resistances to be $R''_{swnt,tot}=12 \text{ m}^2\text{KW}^{-1}$. This value is comparable to the values of $12\text{-}23 \text{ m}^2\text{KW}^{-1}$ [52, 69, 84] for aligned MWNT array structures measured in prior work. The lower performance of the MWNT arrays may be due to the decrease in conformability of the shorter nanotubes, an increase in surface roughness of the MWNT arrays, or a significantly lower intrinsic resistance of MWNTs. Although the contact between the SWNT and the metal is probably much stronger than the van der Waal's dominated contact in the MWNT experiments, the use of pressure most likely increased the number of tubes contacting the interface in the MWNT experiments.

2.1.4 Thermal Model for Conduction in CNT Films

In this section we propose a hypothesis for the nanoscale SWNT-metal contact geometry that aims to explain the unexpectedly low values of the effective heat capacity and large interface resistances presented in Table 2.1. Related to this hypothesis, we develop an approximate thermal model of heat transport within the CNT film with the purpose of understanding the relationship between the effective volume fraction of tubes that contribute to the heat capacity and those that contribute to the thermal resistance within the CNT array. Through this understanding we can estimate the intrinsic thermal contact resistance between an individual SWNT and metal film from the measured data.

Since the aluminum film (Fig. 2.1c) is porous with its nominal thickness of 160 nm being comparable to the 60 nm RMS CNT surface roughness, we believe that incomplete contact between the SWNTs and the metal film reduces the CNT volume fraction that contributes to heat conduction significantly below the 12vol% of CNTs estimated from the catalyst preparation conditions. Figure 2.4 schematically illustrates our belief that the uneven CNT surface topography due to the variation in SWNT

heights combined with the porosity of the metal film causes the metal to make poor contact, particularly with the shorter nanotubes in the array. The TEM cross sectional image of the SWNT-Pd-Al interface shown in Fig. 2.7a shows the interface structure illustrating a higher density of CNTs within the array than at the interface and a large number of voids near the interface that lead to a low fraction of CNTs in full contact with the metal.

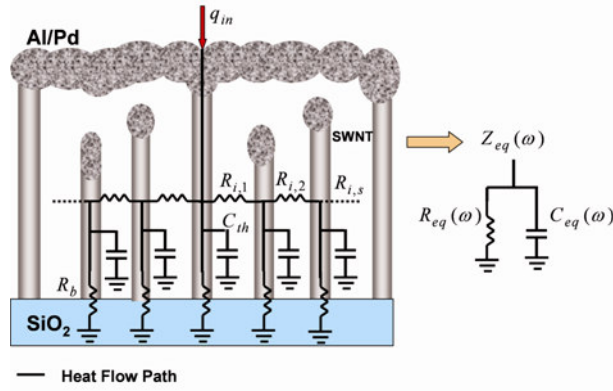


Figure 2.4: Schematic illustrating the hypothesis that a subset of the CNTs are in good thermal contact with the porous and discontinuous evaporated film. The data suggest that the overwhelming majority of the heat transport is brought about by longer tubes that fully contact the metal film. We use a thermal circuit model to account for lateral thermal transport in the CNT film. The heat flows into the central tube that is in thermal contact with the metal film and then flow laterally through the inter-tube coupling resistance to surrounding tubes. We reduce the thermal network to a frequency dependant parallel equivalent RC thermal circuit, which is what is experimentally measured.

To understand how the hypothesized contact geometry relates to the film thermal properties, we suggest a simple geometric model for the incomplete CNT-metal thermal contact in which we consider one individual SWNT that is in contact with the metal film and assume that the surrounding tubes are not in contact with the metal film. We will assume that heat flows into the central tube, and can then couple to the

THERMAL CHARACTERIZATION OF METAL-COATED ALIGNED NANOTUBE ARRAYS

surrounding tubes through an inter-tube coupling resistance R''_i (m^2KW^{-1}) (defined on the CNT perimeter area $A_p = \pi d L_{cnt}$). Included in the inter-tube coupling resistance are all possible thermal transport channels such as conduction, radiation, or occasional CNT-CNT contact between two aligned CNTs. Equating a thermal network model (Fig. 2.4) of heat transfer within the CNT array to an equivalent parallel effective thermal capacitance and resistance of the SWNT yields the experimentally measured effective thermal properties.

Because the interface resistance is much larger than the intrinsic SWNT resistance, we model the thermal impedance of each nanotube as a lumped thermal capacitor in parallel with a thermal boundary resistance, R_b (KW^{-1}), between the SWNT and oxide layer. The total complex thermal impedance of an individual CNT is

$$Z_{cnt} = \frac{Z_C Z_b}{Z_C + Z_b} \quad (2.12)$$

where

$$Z_b = R_b \quad (2.13)$$

$$Z_C = \frac{1}{i\omega C_{th}} \quad (2.14)$$

where $C_{th} = C_{v,a} \pi d b L_{cnt}$ is the total heat capacity of an individual tube. The total effective admittance of the CNT network is given by

$$\frac{1}{Z_{eff}} = \frac{1}{Z_{cnt}} + \frac{1}{Z_{s,eff}} \quad (2.15)$$

where $Z_{s,eff}$ is the total thermal impedance of the surrounding neighboring tubes calculated below. Equating the admittance of Eq. (2.15) to the admittance of the equivalent parallel RC thermal circuit,

$$\frac{1}{Z_{eq}} = \frac{1}{R_{eq}(\omega)} + i\omega C_{th,eq}(\omega) \quad (2.16)$$

Yields

$$R_{eq}(\omega) = \frac{1}{\text{Re}\left(\frac{1}{Z_{eff}}\right)} \quad (2.17)$$

$$C_{th,eq}(\omega) = \frac{1}{\omega} \text{Im}\left(\frac{1}{Z_{eff}}\right) \quad (2.18)$$

A frequency-weighted average based on a representative thermal spectrum of the analytical solution of the metal temperature field yields the total R_{eq} and $C_{th,eq}$ for the SWNT in contact with the metal film

$$R_{eq} = \frac{\int_{\omega} R_{eq}(\omega) X(\omega) d\omega}{\int_{\omega} X(\omega) d\omega} \quad (2.19)$$

$$C_{th,eq} = \frac{\int_{\omega} C_{th,eq}(\omega) X(\omega) d\omega}{\int_{\omega} X(\omega) d\omega} \quad (2.20)$$

where $X(\omega)$ is the amplitude of the Fourier transform of the metal thermal response.

We calculate total impedance of the surrounding neighboring tubes, $Z_{s,eff}$, by assuming a simple close-pack arrangement of the CNTs shown schematically in Fig. 2.5a. Around the central tube contacting the metal film, we separate by the average CNT spacing the surrounding non-contacting tubes into concentric “nearest neighbor” shells. The inter-tube coupling resistance R''_i links the total thermal impedance of each shell in the network (Fig. 2.5b).

THERMAL CHARACTERIZATION OF METAL-COATED ALIGNED NANOTUBE ARRAYS

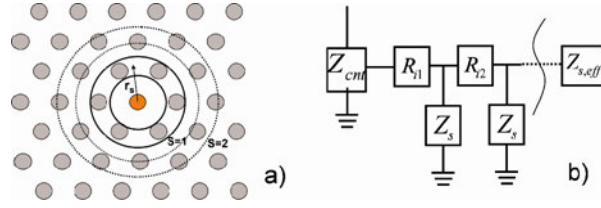


Figure 2.5: a) Schematic top view of CNT in a close pack arrangement grouped into concentric shells of neighboring tubes to calculate the effective impedance of the series of neighboring tubes, as assumed in the model. b) Block diagram of impedance network modeling the linking of neighboring shells by and inter-shell thermal resistance.

From the CNT geometric arrangement, the total impedance of the parallel n_s tubes in the s^{th} shell from the central tube is

$$Z_{cnt,s} = \frac{Z_{cnt}}{n_s} \quad (2.21)$$

where the number of tubes in the s^{th} shell is

$$n_s = 4s\sqrt{\frac{\pi\phi}{2\sqrt{3}}} \quad (2.22)$$

and where s is the shell label (1, 2, 3, ...) and ϕ is the volume fraction (~12%). The total resistance between the s^{th} and the $s^{th}-1$ shell in terms of R''_i is

$$R_{i,s} = R''_i \left(\frac{1}{A_{inner}} + \frac{1}{A_{outer}} \right) = \frac{R''_i}{\pi dL \sqrt{\frac{8\pi\phi}{\sqrt{3}}}} \left(\frac{1}{s} + \frac{1}{s-1} \right) \quad (2.23)$$

Combining Eq. (2.21) and Eq. (2.23), yields the recursive relation for the total effective impedance of $Z_{s,eff}$ and all shells beyond

$$Z_{s,eff} = R_{i,s} + \frac{Z_{cnt,s}Z_{s+1,eff}}{Z_{cnt,s} + Z_{s+1,eff}} \quad (2.24)$$

which gives $C_{th,eq}$ and R_{eq} through Eq. (2.15) and the subsequent relations.

In Fig. 2.6, we show the dependence of $C_{th,eq}$ and R_{eq} , normalized to the capacitance, $C_{th,cnt}$, and resistance, R_b , of a individual tube, on R''_i . Figure 2.6 shows that C_{eff} and R_{eq} are essentially equivalent to the individual tube values for $R''_i > 10^{-3} \text{ m}^2\text{KW}^{-1}$, indicating that lateral conduction within the CNT array is negligible in this regime. Using two vertically aligned MWNT arrays pressed together in an opposing configuration, Hu *et al.* [85] measured $R''_i = 1.4 \text{ m}^2\text{KW}^{-1}$, which is very large. While interpenetrating MWNTs pressed in an opposed geometry is a variant of the aligned SWNTs geometry of this study, the similarity in thermal transport in aligned independent nanostructures allows sensible comparison. Owing to increased CNT-CNT contact due to mechanical deformation, the MWNT inter-tube coupling resistance presumably provides a lower bound for the SWNT case.

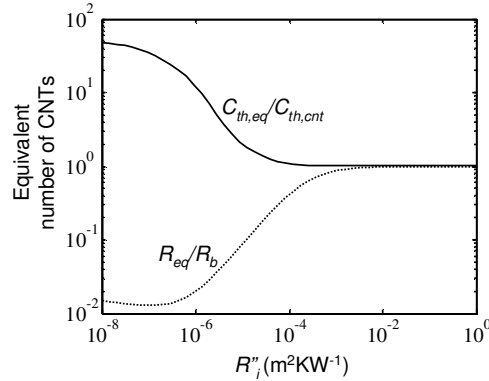


Figure 2.6: The effective thermal capacity, $C_{th,eq}$, and thermal resistance, R_{eq} , due to inter-tube coupling effects normalized to that of an individual tube as a function the inter-tube coupling resistance R''_i .

Recent work using classic molecular dynamics simulations to investigate the dependence of the inter-tube thermal contact resistance between two aligned SWNTs

on the distance between the CNT walls show that for distances larger than ~ 1.3 nm, the inter-tube thermal resistance is extraordinarily large ($> 10^{-4} \text{ m}^2\text{KW}^{-1}$) [86]. That the inter-tube resistance predicted by the simulations in Ref. [86] agrees reasonably with measurements of the interfacial thermal resistance between SWNTs and octane [70], suggests that the simulations capture the essential nanoscale physics, and that phenomenon such as near field radiation transfer is insignificant in this analysis. Based on the prior data and simulations, we believe that inter-tube coupling effects are insignificant in the analysis in this work. Thus, the effective thermal properties are entirely determined by the tubes that are in thermal contact with the metal film and that the tubes in poor thermal contact contribute negligibly. If inter-tube transport were significant, then the number of tubes that contribute to volumetric heat capacity would differ from the number of tubes that contribute to the thermal resistance and contact resistance.

If inter-tube coupling is negligible, the effective volume fraction of tubes contributing to conduction is nearly identical to the effective volume fraction contributing to the heat capacity and thus

$$f_{eff,R} \approx f_{eff,C} = 0.0035 \quad (2.25)$$

Calculation of these results exploits the directly measured volumetric heat capacity, and does not depend on the precise knowledge of the true CNT film porosity, which is challenging to directly measure. This small effective volume fraction contributing to thermal transport, which we attribute to poor contact geometry, provides an explanation for the extraordinarily large thermal boundary resistances observed in most nanotube arrays.

Additionally, if inter-tube coupling effects are negligible, the volume fraction of tubes contribution to conduction and interface resistance is the same. Scaling the area-averaged interface resistances by $f_{eff,R}$ yields a value of $10 \text{ m}^2\text{KGW}^{-1}$ for the individual CNT-Pd contact resistance and $32 \text{ m}^2\text{KGW}^{-1}$ for the individual CNT-SiO₂

contact resistance, consistent with the area definition A_a . We believe that the two additional interfaces with the catalyst and SiO_2 at the base of the CNTs explain why $R''_{cnt-\text{SiO}_2}$ is about three times larger than $R''_{cnt-\text{Pd}}$.

It is useful to compare the extracted results of the intrinsic CNT-metal contact resistance with both other experimental studies and theoretical calculations. Utilizing Joule self-heating of a MWNT on a metal substrate, Kim *et al.* [40] measured the CNT-metal contact resistance to be $29 \text{ m}^2\text{K}^1\text{GW}^{-1}$, based on the area $A=dL_{cnt}$, where $d=14 \text{ nm}$ is the diameter and $L_{cnt}=1 \text{ }\mu\text{m}$ is the contact length. The reasonable agreement of Ref. [40] with those presented in this paper suggests that the mechanisms of thermal transport between metal deposited on the end of a CNT and a CNT lying on a metal substrate may be similar.

We can provide an approximate lower bound for CNT-Pd contact resistance using the acoustic mismatch (AMM) theory of boundary resistance, reviewed in Schwartz and Pohl [22], in which phonon transport across a boundary is treated analogously to acoustic impedance mismatches. The AMM theory has been developed and applied to thermal interfaces between three dimensional materials, with insufficient development for interfaces between low dimensional structures of possibly differing dimensionality.

Proper characterization of the nanoscale interface is critical because the complicated and ambiguous nanoscale geometry strongly dictates the mathematical structure of the AMM calculation. Although a SWNT is often treated as a quazi-1D structure, its interface with a metal includes 2D and 3D aspects. We make the approximation that the nanotubes have a quasi-2D isotropic “flat-sheet” geometry, since nanotubes behave much like a 2D graphene sheet due to the strong excitation of the phonon sub-bands at room temperature [47]. We consider one longitudinal and two transverse acoustic polarization branches as well as model the Pd as an isotropic 2D medium. We derive the heat flux for a given temperature drop across the 2D boundary analogously to a 3D medium as in Refs. [22, 87] to be

*THERMAL CHARACTERIZATION OF METAL-COATED ALIGNED NANOTUBE
ARRAYS*

$$\dot{q}'_{cnt-Pd} = \left(\frac{1}{2\pi}\right)^2 \left(\frac{k_b T_{cnt}}{\hbar}\right)^3 \sum_{s=pol} \int_{-\frac{\pi}{2}}^{\frac{\pi}{2}} \alpha_{cnt-Pd,s}(\theta) \left(\frac{\hbar}{c_s}\right) \cos(\theta) d\theta \int_0^{\frac{\theta_{d,Pd}}{T_{Pd}}} x^2 \left[\frac{1}{e^{\left(\frac{x T_{cnt}}{T_{Pd}}\right)}} - \frac{1}{e^x} \right] dx \quad (2.26)$$

where $\theta_{d,Pd} \sim 250$ K is the Debye temperature of the palladium, T_{cnt} and T_{Pd} are the temperatures of the CNT and Pd side of the boundary, respectively, and $\alpha_{cnt-Pd,s}(\theta)$ is the transmission coefficient computed using the AMM approximation given by [22]

$$\alpha_{cnt-Pd,s}(\theta) = \frac{4 \frac{(\rho_{Pd} c_{Pd,s})}{(\rho_{cnt} c_{cnt,s})}}{\left[\frac{(\rho_{cnt} c_{cnt,s})}{(\rho_{cnt} c_{cnt,s})} + \frac{\cos(\theta_{Pd})}{\cos(\theta_{cnt})} \right]^2} \quad (2.27)$$

where ρ_i is density of material “i”, $c_{i,s}$ is the acoustic velocity of polarization “s” in material “i”, and θ_i is the phonon angle of incidence in side “i”. Computing the heat flux from the CNT side avoids critical cone considerations since it has the higher phonon velocities [87]. Assuming elastic boundary scattering with no mode conversion, the integral in Eq. (2.26) is limited by the lower Debye temperature (Pd) since no modes at higher frequency can be transmitted into the Pd.

From Eq. (2.26), the boundary resistance is defined as

$$R''_{AMM} = \frac{(T_{cnt} - T_{Pd})b}{\dot{q}'_{cnt-Pd}} \quad (2.28)$$

which upon numerical evaluation gives $R''_{AMM} = 3.1 \text{ m}^2 \text{K}^1 \text{GW}^{-1}$, and is consistent with the area $A_a = \pi db$ in which the phonons in the CNT are confined. The AMM calculation predicts a boundary resistance 3.2 times lower than the extracted value for the SWNT-Pd contact, which is rather reasonable considering that AMM predictions are usually much larger at room temperature [22]. Typically, the AMM theory only applies at low temperature where the phonon wavelength is much larger than the

interface roughness. However, we believe that the AMM model predicts reasonable results because the Debye temperature of the CNTs is much higher than room temperature ($\theta_{d,CNT} \sim 2500$ K), so the calculations are in the “low temperature” regime when performed from the CNT side. Also, the nanotube-metal contact is atomistic and thus conventional surface roughness considerations in phonon transport are poorly defined and inapplicable.

The consistency of the experimental results with the AMM predictions indicates that the intrinsic conduction between an individual CNT and the metal film approaches fundamental physical limits. Thus, increasing the number of CNT-substrate contacts is the most promising approach for improving the thermal performance of CNT-based interface materials. As well, the discrepancy between theory and the measured data merits future theoretical analysis, possibly considering more detailed modeling of the nanoscale dimensional effects and transport at the interface between the quasi-1D CNT and the 3D metal film.

2.1.5 Summary and Conclusions

This section studies the room temperature thermal properties of metalized vertically-aligned SWNTs using a nanosecond thermoreflectance technique. We measure the total thermal resistance of the TIM to be $R''_{eff,tot} = 12 \text{ m}^2\text{KW}^{-1}$, which we determine to be dominated by the interface resistance and not the thermal conductivity of the CNTs themselves. Images of the metal film and the CNT surface topography suggest a model for the CNT-metal contact, where by only a subset of the CNTs are actually responsible for the thermal transport. The results show that the effective volume fraction of SWNTs contributing to thermal transports is 0.35%, which is much less than the estimation of the true volume fraction of $\sim 12\%$ from the catalyst deposition process. Based on the effective volume fraction, the intrinsic thermal resistance for an individual SWNT-Pd contact is $R''_{cnt-Pd,a} = 10 \text{ m}^2\text{KW}^{-1}$ (based on the annular area, $A_a = \pi db$), which is in reasonable agreement with the upper limit predictions of the

AMM theory. These results suggest that increasing the number of CNT-substrate contacts can potentially reduce the total thermal resistance of an SWNT array to less than $1 \text{ m}^2\text{KW}^{-1}$. Future work towards developing practical CNT based TIMs needs to address the CNT contact geometry as well as characterize the lateral mechanical compliance of aligned nanotube arrays and its effect on the contact geometry and thermal transport, particularly during thermal cycling.

2.2 Temperature-dependent Phonon Conduction and Composition Dependence of Nanotube Engagement in Metalized Single Wall Carbon Nanotube Films

2.2.1 Introduction and Motivation

While aligned arrays of single and multi-wall carbon nanotubes (SWNT, MWNT) films are promising materials for thermal management [48, 52, 88, 89] and electronics applications such as field emission devices [90], flexible electronics [90], transistors [91], sensors [92], tough interfaces [93], and energy storage materials [94], as the previous sections demonstrated, integrating these materials into devices and structures creates additional interfaces, often with metals, that inhibit heat conduction. Measurements with various nanotube-substrate interface combinations such as pressed metal and dielectric interfaces [52, 88, 89], growth interfaces [48, 69, 89, 95], and physically deposited metals [48, 69], yield large nanotube-substrate thermal interface resistances in the range of $0.3\text{-}50 \text{ mm}^2\text{K/W}$. These large resistances are due to incomplete nanotube-substrate contact amplifying the nanoscale conduction resistances of individual nanotube-substrate interfaces [48, 69]. Such individual nanoscale metal-tube interfaces often dominate the conduction resistances for film thicknesses below $\sim 50 \text{ }\mu\text{m}$. The nanoscale features of the contact further complicate the interface resistance by modifying the phonon transport physics, for which there are

no established models [96]. The structure of these interfaces at the nanoscale is highly dependent on the interaction, adhesion, and wettability of the CNT and substrate materials. Previous data yield no clear relation between interface resistance and interface structure. Better understanding the contribution of the interface materials on the conduction physics and effective nanotube contact area at the interface are necessary to improve the thermal performance of nanotube films. This work directly measures the contribution of interface metallization on the SWNT engagement efficiency and thermal interface resistances via the composition dependence of the interface resistances and effective heat capacities of metal-coated SWNT films using nanosecond thermoreflectance thermometry. The temperature dependence of these properties provides a means to study phonon transmission at the interface.

2.2.2 Sample Preparation and Thermal Property Measurement

The details of the alcohol-CVD SWNT growth process used in this work can be found in Murakami *et al* [97]. Dip-coating a Si substrate into a Co-Mo acetate solution forms a dispersed monolayer of catalyst particles ($\sim 1.3 \times 10^{17} \text{ m}^{-2}$). Annealing in air at 400 °C converts the acetates to metal oxides, followed by an Ar/H₂ reducing flow to retrieve the catalytic activity. The SWNTs are grown using alcohol-CVD at 800 °C [97] to yield an aligned SWNT film 10 μm thick and a SWNT density of ~2-3%, which was measured by comparing the weight of the substrate before and after removing the SWNT film using a precision microbalance. Since the individual samples are derived the same growth batch, the variation in the density amongst the samples is less than 20%. Raman data yield an average SWNT diameter of 1.9 nm and a D/G ratio of 0.012 with a D-band FWHM of 20 cm^{-1} , suggesting high purity films. TEM images reveal that the SWNT films consist of SWNT bundles with ~10 or fewer nanotubes per bundle and a median of 6 SWNTs per bundle [98]. The resolution limits of the TEM place a lower bound of ~10% on the number of bundles that consist of individual tubes; however, the actual number may be much larger. Aligned SWNT films are individually metalized by e-beam evaporating a 50 nm

THERMAL CHARACTERIZATION OF METAL-COATED ALIGNED NANOTUBE ARRAYS

coating of either Al, Pt, Pd, Ti, or Ni at a substrate temperature of ~ 300 K. SEM images of the individual samples were used to measure the local SWNT thicknesses, and showed thickness variations less than $1.0\ \mu\text{m}$. Following an air break, 50 nm of Al was e-beam evaporated onto the samples to improve the surface reflectivity and uniformity for the thermoreflectance measurement. Duong *et al.* [99] present a detailed SEM analysis of the dependence of the metal-SWNT morphology on material and deposition conditions. A representative TEM cross section of an Al(160 nm)/Pd(20 nm)-SWNT interface in Fig. 2.7a shows many voids and a lower SWNT density near the interface compared to deeper within the sample. This incomplete contact leads to partial engagement between the SWNTs and the metal, increasing thermal conduction resistances (see section 2.1).

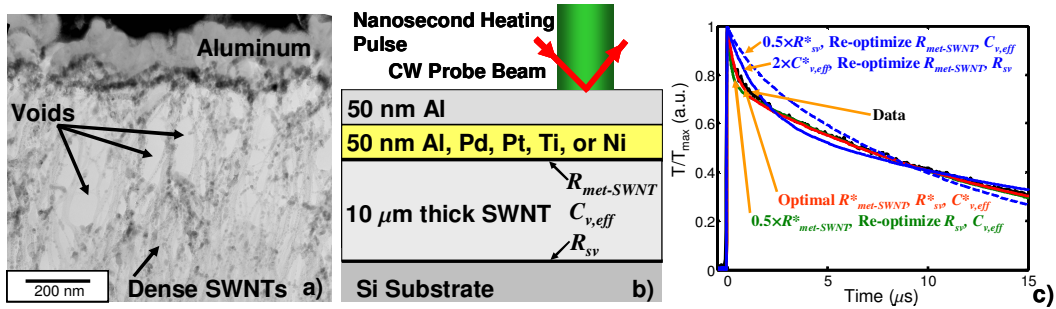


Figure 2.7: a) Representative TEM of SWNT-metal contact showing voids and incomplete contact near the metal interface. b) Schematic of sample geometry used in the measurements and for the thermal model. c) Representative thermal trace data for the 100 nm Al-coated sample (black) along with optimal fit (solid red) yielding the optimal parameter set $R_{met-SWNT}^*$, R_{sv}^* , and $C_{v,eff}^*$. The blue and green traces illustrate the data extraction sensitivity, showing the results of varying one of the fit parameters from its optimal value and re-optimizing the fit of the remaining two free parameters to the data.

This study uses nanosecond thermoreflectance thermometry to measure the interface resistances and heat capacity of the metalized SWNT films, the details of which can be found in section 2.1 and previous work [48]. In brief, a 3 mm diameter, 532 nm wavelength, 6 ns pulse from a Nd:YAG laser heats the surface of the metal film at a rep-rate of 10 Hz. A 10 mW, 658 nm continuous wave probe laser is focused on the metal in the middle of the pump beam to a diameter of $\sim 20\ \mu\text{m}$. A 650 MHz

photodiode and oscilloscope capture the reflected intensity of the probe laser with sub- μ s temporal resolution. The reflected probe intensity linearly tracks the relative changes in metal surface temperature, yielding the normalized thermal response. Lateral heat conduction is negligible since the pump beam diameter is much large than the maximum thermal diffusion distance during the measurement.

A least-squares algorithm fits the data to a solution of the heat diffusion equation for a multilayered stack model of the structure (Fig. 2.7b) using three parameters [48]: the metal-SWNT interface resistance, $R_{met-SWNT}$, the effective volumetric heat capacity of the SWNT film apparent at the measurement timescales, $C_{v,eff}$, and a resistance, $R_{sv}=R_{SWNT-sub}+R_{SWNT,vol}$, which captures the combined resistance of the SWNT-substrate interface resistance ($R_{SWNT-sub}$) and the residual volumetric resistance of the SWNT film ($R_{SWNT,vol}$). The measurement for these particular samples is sensitive only to R_{sv} and neither $R_{SWNT-sub}$ nor $R_{SWNT,vol}$ individually. The unique impact of $R_{met-SWNT}$, $C_{v,eff}$, and R_{sv} on the shape of the thermal response at different time scales permits their isolation [48]. Figure 2.7c presents sample thermal trace data, the optimal fit of the solution of the heat diffusion equation, and an illustration of the parameter extraction sensitivity by varying one parameter from its optimal value and re-optimizing the remaining two free parameters. The effective SWNT volume fraction contributing to the heat capacity during the timescales of the measurement can be estimated by $\phi=C_{v,eff}/C_{v,ind}$, where $C_{v,ind}\sim 1.5 \text{ MJ/m}^3\text{K}^{-1}$ is the volumetric heat capacity of an individual SWNT [48]. Experimental studies report a wide range of values for the conductivity of individual SWNTs and MWNTs, with values falling in the range of $\sim 50\text{-}3600 \text{ Wm}^{-1}\text{K}^{-1}$ [4, 100, 101]. In fitting the data, we assume an effective SWNT conductivity of $k_{cnt,eff}=\phi\times k_{SWNT}$, where $k_{SWNT}=3600 \text{ Wm}^{-1}\text{K}^{-1}$ is the individual SWNT thermal conductivity of high quality SWNTs [4]. A reduced SWNT conductivity will appear as an additional contribution to R_{sv} . We neglect the metal-metal interface resistance since it is typically much less than $R_{met-SWNT}$, and since the thermalization time of the metals is less than the temporal resolution of the system.

The apparent effective heat capacity can deviate from the heat capacity based on the nominal density of the 3% volume fraction films if there is poor SWNT-metal contact

and if large inter-tube thermal resistances cause the partial inter-tube thermalization of the SWNTs during the timescales of the measurement [48]. However, the detailed model of inter-tube heat transfer within the array at the nanoscale developed in the previous section work [48] suggests that inter-tube thermal transfer within the array is weak during the timescales of the measurement due to the large inter-tube thermal resistances. These results also suggest that the effective volume fraction contributing to the heat capacity is a reasonable measure for the volume fraction that makes good thermal contact with the metal film [48]. These results are supported with simple thermalization timescale arguments. Based on conductance of 3-50 pW/K for crossed SWNTs in intimate contact [86, 102, 103], the thermalization time of a 10 μm long SWNT in such cross-contact is $\sim 0.5\text{-}1\ \mu\text{s}$. Such values are a reasonable lower bound since the weak inter-tube van der Waals interactions make intimate contact unlikely and can lead to large inter-tube contact resistances [86]. For bundle-bundle contact, the thermalization timescales are likely longer since the thermal mass of the bundle that can scale faster than the bundle-bundle contact area. The extraction of the heat capacity and the metal-SWNT interface resistances sensitivity are most strongly weighted by the thermal response below 3 μs for these films (Fig. 2.7c). Consequently, the apparent heat capacity can measure a large fraction of non-thermalized SWNTs. However, the apparent heat capacity may potentially change over the longer timescales of the measurement, which can greatly complicating the analysis and interpretation.

2.2.3 Data Results and Interpretation

Figure 2.8a plots $R_{\text{met-SWNT}}$, R_{sv} , and their sum total, R_{tot} , versus the measured effective heat capacity volume fraction, ϕ , for the five metallization. The error bars capture the uncertainty due to variations in measurement data taken at four different locations on each sample, variations in film physical properties (e.g. film thickness), and the sensitivity to the uniqueness of the fit parameter combinations. While $R_{\text{met-SWNT}}$ falls in the range of 3.5-9.2 $\text{mm}^2\text{K/W}$, R_{sv} is much larger, ranging between

33-46 mm²K/W. The larger values of R_{sv} compared to $R_{met-SWNT}$ may be due to a variety of contributions including large SWNT-substrate interface resistances, large SWNT volumetric resistances, or an artifact of the effective heat capacity increasing over the longer timescales of the measurement ($\sim 10 \mu s$) for which R_{sv} is sensitive. Attributing these larger values of R_{sv} entirely to $R_{SWNT,vol}$ would require a very low value of $k_{cnt,eff} \approx 0.3 \text{ Wm}^{-1}\text{K}^{-1}$, which would yield an estimate of $k_{SWNT} \approx 45 \text{ Wm}^{-1}\text{K}^{-1}$ based on the effective SWNT volume fraction, ϕ . Although the literature has reported values as low as $\sim 50 \text{ Wm}^{-1}\text{K}^{-1}$ for k_{SWNT} , [100] we suggest that, given the high quality of the SWNT tubes indicated by the Raman data, a more plausible explanation is that the large R_{sv} is dominated by $R_{SWNT-sub}$ due to the weak adhesion of the catalyst particles resulting from the “dip-coating” technique. Measurements of similar films [48] that utilized PVD catalyst deposition showed similar values for $R_{met-SWNT}$, but much lower values of $R_{SWNT-sub}$ at a lower ϕ .

THERMAL CHARACTERIZATION OF METAL-COATED ALIGNED NANOTUBE ARRAYS

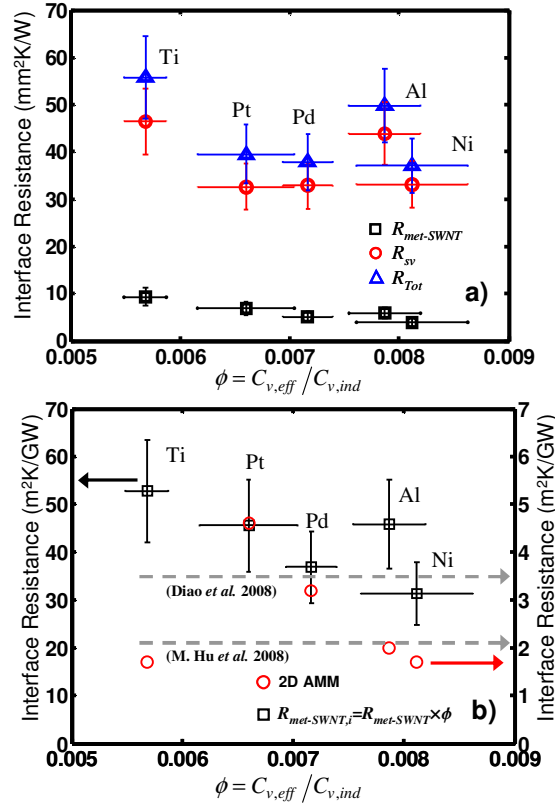


Figure 2.8: a) Measured area-averaged metal-SWNT, SWNT-substrate, and total thermal resistance plotted as a function of the measured effective SWNT heat capacity volume fraction, ϕ , calculated by dividing the measured effective SWNT volumetric heat capacity $C_{v,eff}$, by the volumetric heat capacity of an individual SWNT, $C_{v,ind}$. b) Estimated resistance of individual metal-SWNT contact extracted by multiplying the area-average metal-SWNT interface resistance by ϕ . Data are compared to theoretical predictions of the individual SWNT interface resistance from molecular dynamics of SWNT-Si interfaces from M. Hu *et al.* [104] and Daio *et al.* [105] (gray-dashed arrows) and from the AMM model modified for 2D-2D interfaces. [48] The theoretical values are shown on the right axis for clarity.

The observations that the effective SWNT volume fractions are much less than the nominal volume fraction of 3%, and the trend in the data of decreasing $R_{met-SWNT}$ with increasing ϕ suggest that the large interface resistance in SWNT arrays are due to a low SWNT engagement efficiency with the metal. Sample-dependent nanoscale surface morphologies and differences between the metals' abilities to coat the SWNTs may explain their relative engagement efficiencies. Previous observations [99, 106] showed that the metal-SWNT coating behavior can be strongly dependent on

metal-SWNT interaction energies [106], with Ti, Ni, Pd, and Al demonstrating an increasing tendency to cluster on the individual SWNTs. Metals that effectively coat the SWNTs can show reduced engagement due to the lower tendency of the metal to form inter-tube clusters that can bridge multiple tubes and bundles. This effect can explain the low value of ϕ for Ti compared to other metals since Ti has an excellent ability to coat SWNT and a low tendency to form clusters.

The thermal resistance of an individual SWNT-metal interface, $R_{met-SWNT,i}$, can be estimated from the relation $R_{met-SWNT,i} = R_{met-SWNT} \times \phi$ [48]. Fig. 2.8b shows the relation between $R_{met-SWNT,i}$ and ϕ , along with the results of molecular dynamics simulations for the resistance of an individual (10,10) SWNT-Si interface [104, 105]. Fig. 2.8b also shows theoretical predictions of individual metal-SWNT interface resistances based on a modification of the acoustic mismatch model (AMM) in an approximation treating the SWNT as a graphene-metal 2D-2D interfaces [48]. The AMM model predicts resistances similar to the molecular dynamics (MD) simulations of Si-SWNT interfaces and follows the general data trend with metallization.

The trend of decreasing $R_{met-SWNT,i}$ with increasing ϕ suggests that the same physical properties that govern the interface resistance (e.g. interface adhesion energies, Debye temperatures, etc.) may be related to the mechanisms that govern the engagement of the metal with the SWNTs. $R_{met-SWNT,i}$ is about an order of magnitude larger than the theoretical predictions. Non-ideal metal-SWNT interface geometries may explain this discrepancy. The bundle structure of the nanotubes can reduce the ratio of the metal-SWNT interface area to the SWNT volume and consequently increase the apparent individual metal-SWNT interface resistance. The models do not account for the likely formation of metal nanoclusters along the SWNTs which creates additional interfaces and modifies the local phonon density of states due to the effects of reduced and mismatched geometries [31, 107, 108]. However, the lower interface resistance values predicted by the MD simulations suggest that in addition to improving the engagement, there is the potential to significantly reduce the thermal resistance of SWNT films by reducing the individual metal-SWNT interface resistance.

THERMAL CHARACTERIZATION OF METAL-COATED ALIGNED NANOTUBE ARRAYS

Figure 2.9a,b is a plot of the temperature dependence of $C_{v,eff}$ and the interface conductance per tube, $(R_{met-SWNT} \times \phi)^{-1}$ and $(R_{sv} \times \phi)^{-1}$, between 125 K and 300 K for a 10 μm thick SWNT film coated with a 100 nm thick aluminum film. The temperature dependencies of these data can provide information about the phonon conduction physics. Optimal power law fits to the data yield temperature dependencies of $C_{v,eff} \sim T^{0.97}$, $(R_{met-SWNT})^{-1} \sim T^{1.08}$, and $(R_{sv})^{-1} \sim T^{0.85}$. In considering the phonon properties, the bundling does not influence the temperature dependencies of $C_{v,eff}$ since $k_b T \gg E_{d\perp}$, where $E_{d\perp} \sim 5$ meV is the Debye energy of the intertube coupling modes and k_b is Boltzman's constant [47]. The SWNT thermal properties are well approximated by those of graphene since $\theta_{sub} \ll T$ where $\theta_{sub} \sim 10$ K is the characteristic temperature of the first optical sub-band of the SWNT estimated from calculations using the dynamical matrix of a classical potential field [47, 109]. Fig. 2.9a compares the measured data to theoretical calculations of the heat capacity of an individual 2 nm diameter SWNT tube using Bose-Einstein statistics based on the above dynamical matrix, and a calculation of the total heat capacity of the acoustic phonon modes in graphene using the band parameters in Prasher *et al.* [43]. Fig. 2.9a shows the individual contribution of the longitudinal acoustic (LA), transverse acoustic (TA), and out-of-plane bending modes (ZA) of graphene to its total heat capacity. Due to the porosity of the SWNT film, the theoretical calculations have been scaled by a factor of 0.006 so that the calculation of the heat capacity matches the experimental data at 300 K. Note that, despite its empirical nature, the classical potential field [109] reproduces the overall features of the phonon dispersion to an extent sufficient for the current analysis [110]. The temperature dependency of the experimental data follows the theoretical predictions of the heat capacity calculation of the SWNT within the measurement uncertainty. The near identical temperature dependency of the acoustic mode heat capacity of graphene and that of the SWNT suggest that the thermal properties of the SWNT are well captured by phonon physics of graphene, in the current temperature range. The calculations show that although the heat capacity is dominated by the ZA mode, the temperature dependency of the LA and TA modes is

CHAPTER 2

stronger in this temperature regime, resulting in a temperature scaling of the total heat capacity that is strongly influenced by all modes.

THERMAL CHARACTERIZATION OF METAL-COATED ALIGNED NANOTUBE ARRAYS

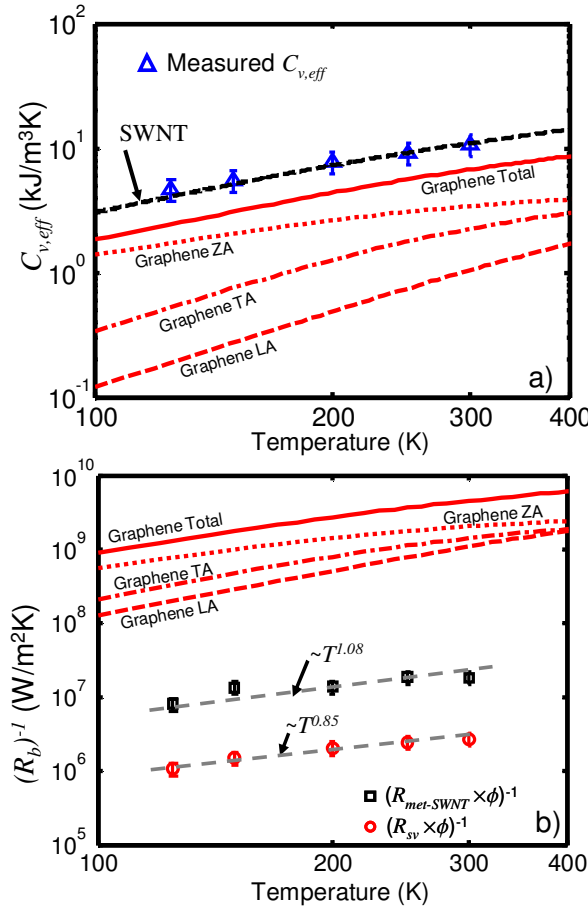


Figure 2.9: a) Temperature dependence of the area-average metal-SWNT interface and effective $C_{v,eff}$ for a 100 nm-thick Al-coated SWNT film. The data are compared to theoretical calculation of the heat capacity of an individual SWNT based on Bose-Einstein statistics using a classical potential function [109] (black-dashed) and a calculation of the heat capacity of graphene acoustic modes (red-solid) based on graphene parameters in Prasher *et al.* [43]. The theoretical predictions have been scaled by a factor of 0.006 so that the value of the data matches the SWNT theoretical results at 300 K. Also shown are the contributions of the graphene longitudinal (LA), transverse (TA), and out-of-plane bending (ZA) acoustic phonon bands to the total graphene heat capacity. b) Temperature dependence of the conductance of individual SWNT interfaces, $(R_{met-SWNT} \times \phi)^{-1}$ and $(R_{sv} \times \phi)^{-1}$. The gray dashed curves are optimal power law fits to the data. The solid red curve is the total theoretical upper bound for the interface conductance of a graphene-metal interface allowing for inelastic scattering. The broken red curves show the contributions from the individual acoustic phonon modes in graphene.

The temperature dependence of $R_{met-SWNT}$ yields information about the metal-SWNT phonon interface transmittance. Under the assumption of a small temperature

difference across the interface and isotropic phonon dispersion, the boundary resistance can be expressed as [24, 25]

$$R_b^{-1} = \Gamma^{inel}(T) \sum_s \frac{1}{\Omega_d} \int_{\Omega_d^+} \int_0^{\omega_{max,s}} \hbar \omega v_s(\omega) \cos(\theta) \frac{\partial n}{\partial T} g_s(\omega) d\omega d\Omega_d \quad (2.29)$$

where s is the mode branch, ω is the phonon frequency, $v_s(\omega)$ is the phonon velocity, n is the Bose-Einstein distribution, T is the temperature, $g_s(\omega)$ is the phonon spectral density of states, θ is the angle between \vec{k} , the phonon wave vector, and the interface normal, Ω_d is the solid angle for d -dimensional space. $\Gamma^{inel}(T)$ is the net phonon transmittance, which allows for implicit inelastic phonon scattering at the interface [25]. The integral is taken over the half space of phonons directed toward the interface (Ω_d^+). To predict the temperature dependency of the interface conductance of the SWNT, we evaluate Eq. (2.29) using the acoustic bands of graphene since the temperature dependency of the phonon heat capacity is well approximated by that of graphene for the temperature range in this work (Fig. 2.9a). Evaluating Eq. (2.29) from the graphene (SWNT) side of the interface and equating $\omega_{max,s}$ to the Debye frequencies of the graphene acoustic modes (which are greater than those of Al) implicitly allows for inelastic phonon transmission [25]. Setting $\Gamma^{inel}(T) = 1$ provides the upper limit to the total (inelastic and elastic) phonon conductance. Assuming a general dispersion relation of the form $\omega_s = c_s k^\alpha$ and combining with Eq. (2.29) yields

$$R_b^{-1} = \Gamma^{inel}(T) \sum_s \frac{k_b}{(2\pi)^d} \left(\frac{1}{c_s} \right)^{\frac{(d-1)}{\alpha}} \left(\frac{k_b T}{\hbar} \right)^{\frac{(d-1)}{\alpha} + 1} \int_{\Omega_d^+} \cos(\theta) d\Omega \int_0^{\frac{\hbar \omega_{max,s}}{k_b T}} \frac{x^{\frac{(d-1)}{\alpha} + 2} e^x dx}{(e^x - 1)^2} \quad (2.30)$$

where d is the dimension. Fig. 2.9b shows the evaluation of Eq. (2.30) using the properties of graphene for the upper bound ($\Gamma^{inel}(T) = 1$) of the total interface conductance and the individual contributions from the LA, TA, and ZA graphene

modes. As with the heat capacity, the interface conductance is dominated by the ZA mode, but the temperature dependency of the LA and TA modes is stronger in this temperature regime, resulting in a temperature scaling of the interface conductance that is strongly influenced by all acoustic modes.

Fig. 2.10 shows the temperature dependence of $I^{inel}(T)$ extracted by dividing the experimental data for the per tube interface conductance by Eq. (2.30) evaluated with $I^{inel}(T) = 1$. A power law fit to the data yields $I^{inel}(T) \sim T^n$ where $0.4 < n < 0.9$ with an optimal of $n \sim 0.6$. Since traditional AMM and diffuse mismatch models (DMM) in the Debye approximation with elastic scattering [22] result in $I^{inel}(T) \sim T^0$ with values on the order of unity, the data suggest that these simpler models do not fully capture the physics of the transport across metal-SWNT interfaces. The low values of I^{inel} may be due non-ideal interface geometry, multiple interfaces in series within the SWNT bundles, and metal clusters along the SWNT amplifying the interface resistance.

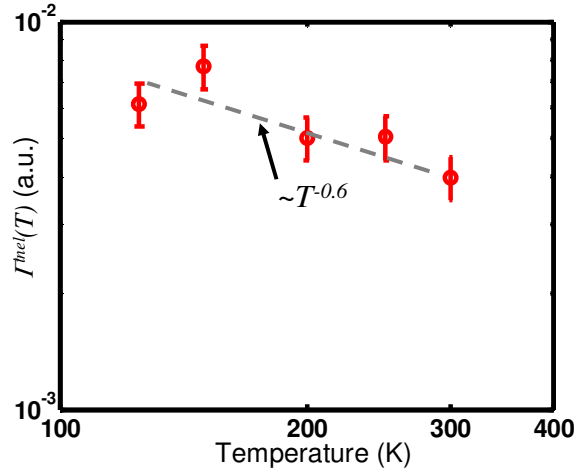


Figure 2.10: Temperature dependence of $I^{inel}(T)$ along with the optimal power law fit (gray-dashed). The temperature dependence suggests inelastic phonon scattering at the interface.

The temperature dependence of $I^{inel}(T)$ suggests a spectral dependence of the individual phonon mode transmission coefficients. This dependency may be due to a combination of inelastic phonon scattering at the interface and density of states mismatch between the materials [26], which can be complicated by the nanoscale

geometry [31, 107, 108], and interface disorder [21]. Inelastic interface scattering becomes more important as the temperature approaches the lower Debye temperature of the two materials. Previous measurements of the boundary resistances of Al/sapphire [111, 112], Pb/diamond [23], and Au/diamond [25, 113] all reported near-linear trends in the boundary conductance over similar temperature ranges, which were attributed to inelastic scattering. Hopkins *et al.* [25] reported a decreasing $I^{inel}(T)$ with increasing temperature due to inelastic scattering. These similar trends in the temperature dependency of $R_{met-SWNT}$ and $I^{inel}(T)$ indicates that inelastic scattering may be important at metal-SWNT interfaces.

2.2.4 Conclusion

In summary, we find that the large thermal interface resistances in SWNT films are related to the degree of engagement of the SWNT films and the interface resistances of individual contacts at the nanoscale. The metallization dependence of the SWNT engagement suggest that engineering the CNT interfaces contacts offers a possible approach to reduce the total thermal resistance of CNT films, potentially below 1 mm²K/W.

2.3 Reduction of Resistances in MWNT Films through Interface Engineering: CNT-indium Composites

2.3.1 Concept and Background

The relation between the thermal interface resistance and partial engagement of CNT films with substrates suggest that improving the effective number of CNT contacts can reduce the total resistance of CNT films. Binding the ends of and aligned

THERMAL CHARACTERIZATION OF METAL-COATED ALIGNED NANOTUBE ARRAYS

nanotube arrays to a substrate with a thin layer of a low melting temperature binder such as indium is a promising approach to improve the performance of CNT arrays through increasing the total CNT-substrate contact area [114]. When forming an interface, melting the binder allows it to conform to the nanotube and substrate topography, which typically has variations in height on the order of hundreds of nanometers (see figure 2.1), and increase the effective area in contact. The use of various adhesion layers can potentially improve the thermal and mechanical contact of the binder with the CNT film. Such a composite may be readily formed into a thermal tape structure which would facilitate the practical implementation of the CNT based TIMs in thermal solutions. Figure 2.11 presents a cartoon illustrate of a conception for a CNT thermal tape solution that can potentially provide a vehicle to combine CNTs with a low melting temperature binder.

Recent work has show similar structures to achieve total thermal resistances below $0.01 \text{ cm}^2\text{K/W}$ for thin ($\sim 7\text{-}10 \text{ }\mu\text{m}$) MWNT films of high density ($\sim 10 \text{ \% vol}$) [69]. However, such film thicknesses are too thin for TIM applications (due to die warpage, etc.) and the increased stiffness due to the high density may degrade its mechanical performance. This work characterizes the thermal performance of indium-MWNT composite structures using infrared thermal microscopy for MWNT films with thickness above $100 \text{ }\mu\text{m}$ and CNT densities around 1 \% vol , which are more promising for a reliable thermo-mechanical interface.

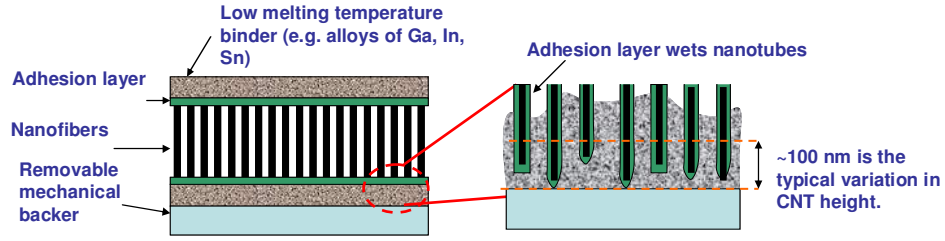


Figure 2.11: Schematic illustration of CNT-binder composite to reduce the resistance in CNT films. The binder is deposited on the CNT ends and is heated after forming an interface to allow the binder to conform to the CNT topography, increasing the real contact area. A thermal tape structure may provide a convenient vehicle to implement CNT films in thermal management solutions.

2.3.2 Sample Preparation and Metrology

The indium-MWNT composites are formed by CVD growth of MWNTs at 850 °C from an ethane pre-cursor on Si substrates of area 1.5 cm x 1.5 cm which are coated with 500 nm thermal SiO₂ followed by 3 nm Fe catalyst. The CNT growth yielded MWNT thicknesses in the range of 50-300 μm and densities around 1 % vol. Following the growth, the CNTs are soldered to a second Si substrate without adhesion layers or flux using a 25 μm thick indium film. The joint was formed by placing the film at the interface and heating to ~200 °C under vacuum with a clamping pressure of ~50 Pa. The second Si substrate incorporates an integrated electrical resistance element with resistance of $R_h=14 \Omega$, which is used to establish a steady-state heat flux through the samples, $q''=P_h/A_{Si}$, where $P_h=I^2R_h$ is the heater power, I is the electrical current, and A_{Si} is the area of the substrate. Typically, currents on the order of 1 Amp are used. IR microscopy captures the cross-sectional full-field temperature profile.

Full-field IR microscopy suitable for the characterization of MWNT films is describe in the literature [85] and is illustrated in Fig. 2.12. The IR microscope measures the full-field temperature of a cross sectional view of the sample under

THERMAL CHARACTERIZATION OF METAL-COATED ALIGNED NANOTUBE ARRAYS

steady state heating with a spatial resolution of $\sim 5 \mu\text{m}$. The emissivity differences are accounted for by a calibration measurement at known temperatures [85]. The temperature difference between the hot Si substrate (T_h) and the cold Si substrate (T_c) and the heat flux yield the TIM resistance from the relation

$$R''_{tot} = \frac{T_h - T_c}{P_h/A_{Si}} = R''_{MWNT} + R''_c \quad (2.31)$$

where R''_{MWNT} is the volumetric resistance of the MWNT film and R''_c is the total contact resistance of the MWNT film and the Si substrates.

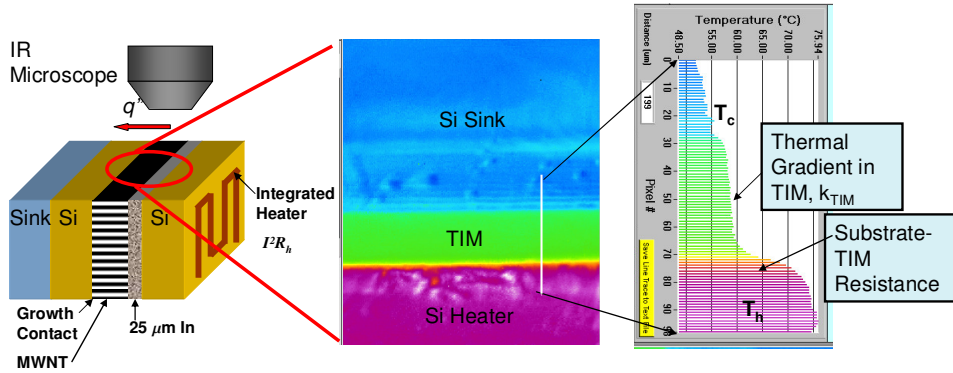


Figure 2.12: Schematic of indium-MWNT composite and IR microscopy configuration. The IR microscope produces a full-field image of the cross-sectional temperature profile under a steady state heat flux. Measuring temperature drop across the TIM enable the extraction of the TIM thermal resistance.

2.3.3 Thermal Resistance Data for Indium-MWNT Composites

Figure 2.13 present the total thermal resistance data for indium-MWNT composite of various thicknesses of MWNT films, along with the total resistance of an indium-only sample and the $28 \mu\text{m}$ thick Al/Pd/SWNT sample data from section 2.1 for comparison. The sample with the lowest resistance achieves a value of $0.07 \text{ cm}^2\text{K/W}$ (yielding a TIM effective conductivity of $\sim 38 \text{ Wm}^{-1}\text{K}^{-1}$) which is a reduction

in total resistance of about 50% compared to previous measurement of pressed MWNTs contacts without indium [52]. This reduction in total resistance suggests increased engagement with the CNTs in the film. While there is significant variation the total thermal resistance among the samples, these results show the possibility of achieving low total thermal resistances at CNT thicknesses and densities promising for a thermo-mechanically reliable bond. Figure 2.13 shows representative temperature profiles of the CNT cross-section, which illustrate the relative contribution of the interface and volume of the CNT film. While the best performing sample has a small volumetric and interface contributions, some of the higher resistance samples show that not only can the interface resistances be significant, but also that the large volume resistances can be reduce the TIM performance. The large CNT volume resistance may be due to poor intrinsic CNT quality or due to the melting of the indium film mechanically damaging the CNT, thereby reducing their quality.

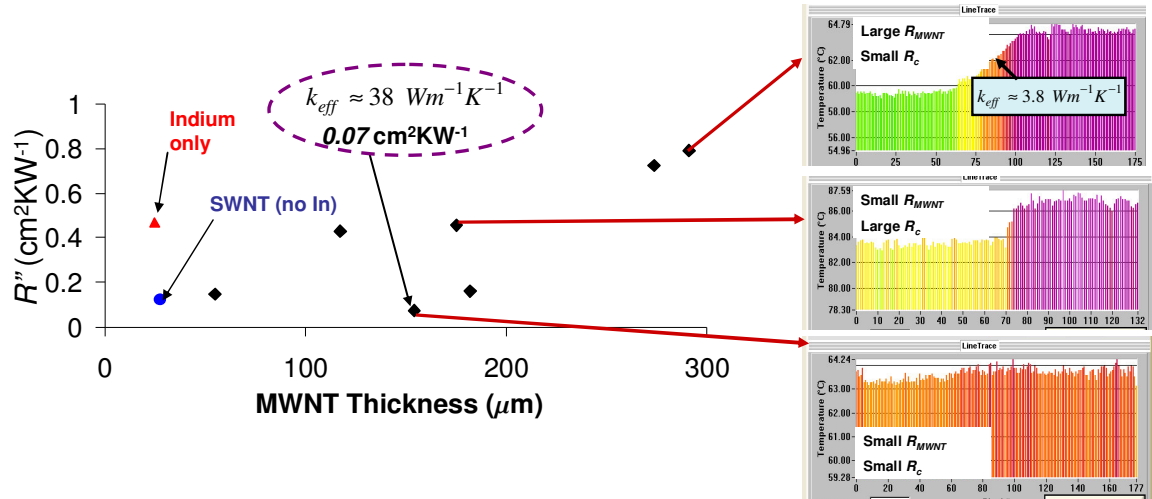


Figure 2.13: Total thermal resistance data for In-MWNT composites consisting of various thicknesses of MWNT films, along with the Al/Pd/SWNT sample presented previously in this work, and an interface consisting of only indium without CNT. The best performing sample has a resistance of $0.07 \text{ cm}^2\text{K/W}$. Representative cross sections temperature profiles show that the relative distribution between interface and volume resistance depends on the samples.

THERMAL CHARACTERIZATION OF METAL-COATED ALIGNED NANOTUBE ARRAYS

Figure 2.14a shows the impact of thermal cycling on the 175 μm thick In-MWNT sample subjected to the thermal cycle illustrated in Fig. 2.14b, in which the sample is heated repeatedly in vacuum between 130 °C and 180 °C through the indium re-melt temperature. The data show an increase in nearly a factor of two of the total resistance over a thousand cycles. This degradation in performance may be due to indium migrating away from hotspots or physically damaging the CNTs during the re-melt.

Improving the indium metallurgical bond through the use of various adhesion layers such as Ti/Ni/Au multilayer stacks, is a promising approach to improving the thermal performance of CNT-In composites. To study the impact of adhesion layers, a Ti/Ni/Au adhesion structure of thickness 100/50/100 nm, respectively, was deposited on the MWTN film and on the second Si substrate prior to soldering the two with the indium film. Figure 2.15a presents the total thermal resistance data for a variety of MWNT films of various thickness, which show that there is no significant enhancement in thermal performance of MWNT-indium composites due to the Ti/Ni/Au adhesion layers (un-fluxed) between at the In-CNT and In-Si interfaces. The poor performance could be due to poor indium adhesion, damage to the CNT from the indium during melting, or low initial CNT quality. Acoustic transmission imaging (Fig. 2.15b) of an In-CNT sample reveals that there is poor metalurgical bonding over most of the structure, suggesting that the poor performance of the samples is due to either poor wetting due to the formation of oxide surface layers, or the physical degradation of the CNT films due the melting of the indium.

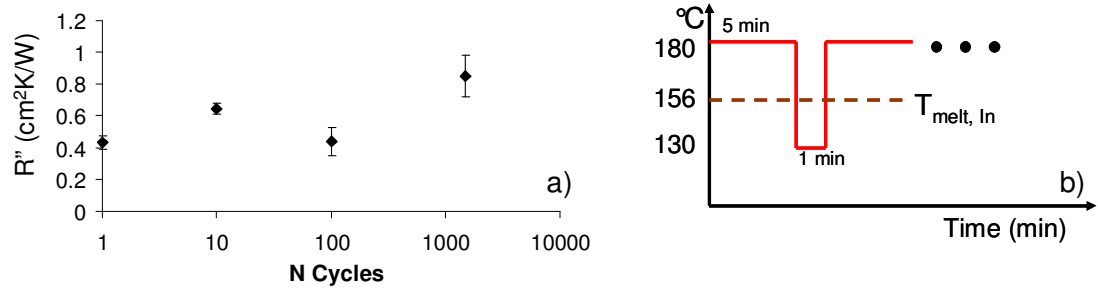


Figure 2.14: a) Impact of thermal cycling on the total thermal resistance of 175 μm thick In-MNWT composite sample. b) Schematic illustration of the thermal cycle.

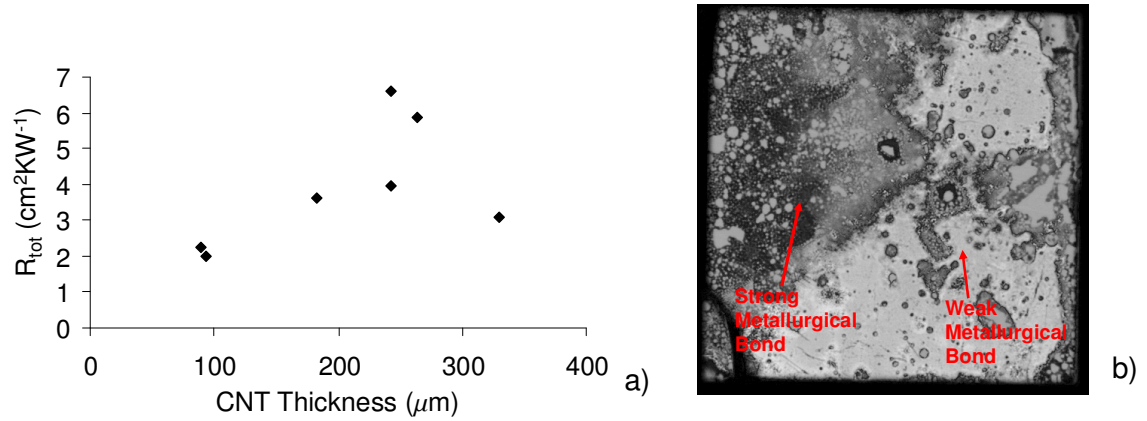


Figure 2.15: a) Total thermal resistance CNT-In composites with un-fluxed Ti/Ni/Au adhesion layers of thickness 100/50/100 nm on both indium interfaces. b) Acoustic transmission image of an In-CNT sample showing poor mechanical bonding of the indium. Dark areas indicate high transmission and strong metallurgical bonds. (acoustic transmission image courtesy of Advance Micro Devices, Inc.)

Although the low resistance value of 0.07 $\text{cm}^2\text{K/W}$ shows promise in improving the thermal performance of CNT films through utilizing a low temperature solder at the interface, the large variation in the resistance values among the samples, the poor repeatability of the data, the degradation of the thermal performance during thermal cycling, and the incomplete bonding across the structure remain challenges that need to be addressed in achieving a high performance CNT based TIM. Although developments to improve the thermal performance of CNT based TIMs are underway,

data for their mechanical properties and the relation between the mechanical and thermal properties of these films are still needed.

2.4 Summary of Conduction Mechanisms in CNT Films

The thermal characterization of aligned CNT films presented in this section has lead to the following understanding of conduction in CNT films, illustrated in Fig. 2.16. While aligned films of CNT can be relatively uniform on the macroscale, the variations in roughness and porosity at the nanoscale can cause partial engagement of the CNTs when the film is interfaced with substrates such as a deposited metal film or pressed mechanical contacts. The partial engagement reduces the effective volume fraction of CNTs participating in heat transfer, which amplifies the nanoscale interface and volume resistances. For films below 50 μm , the nanoscale interface resistances dominate over the volumetric contribution for high quality CNTs. The presence of defects can lead to increases in the volumetric resistances, which increase in probability with CNT length. The impact of inter-tube contact is not clear since although inter-tube contact can increase the effective conductivity by creating additional conduction pathways, the inter-tube interaction can create scattering sites that reduce the individual tube conductance. Increasing the nanotube engagement by engineering interfacial layers is a promising approach to improve the thermal performance of CNT film, and future work needs to focus on optimizing material combinations. Further experimental data and models for individual CNT-substrate contacts are needed to better understand conduction in CNT films.

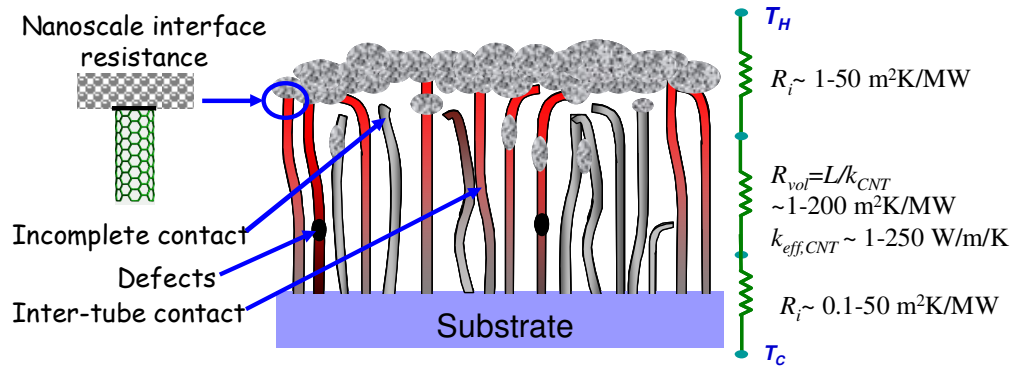


Figure 2.16: Cartoon illustration summarizing the important conduction mechanisms in CNT films and typical values for interface and volume resistances. Partial engagement of the CNT films amplifies nanoscale interface and volume resistances

Chapter 3

Picosecond Thermoreflectance

Thermometry of MWNT Growth

Interfaces

3.1 Motivation

3.1.1 The Need for Picosecond Thermoreflectance Thermometry of MWNT Growth Interfaces

As addressed in the previous chapters, measuring the thermal boundary resistance between arrays of nanotubes and substrates is complicated by the partial engagement of the nanotube tips with substrates. Although a key contribution of this work is the development of an approach to measure this engagement factor, using this data to extract individual CNT-substrate resistances from the area-averaged values is less direct and relies on subtle assumptions about conduction within the arrays during the experiments. In measuring the TBR at the native CNT growth interface, it is a reasonable approximation that the nanotubes are fully physically engaged with the substrate. However, in the traditional configuration where the samples are heated from the top, the apparent value of the growth interface TBR remains complicated by the fraction of tubes that contribute to heat transfer throughout the array and the reduction in sensitivity to the TBR.

Direct measurement of the TBR of the growth interface by establishing a heat flux from the based of the CNT would avoids the challenge of partial CNT engagement associated with the traditional approach. However, such a measurement requires a thin metal film in close proximity (within a thermal diffusion depth during the measurement time scales) to the CNT film and optical access to the base interface. The requirement of a transparent substrate complicates the sample fabrication and reduces the options for suitable substrate materials. Furthermore, the CNT growth interface often requires multiple auxiliary thin films on the order of tens of nanometers thick (such as SiO_2 or Al_2O_3) to assist the growth. These films and their additional interfaces can contribute thermal resistances comparable to that of the CNT growth interface. Thus, accurate isolation of the CNT TBR requires deep sub-micron spatial resolution of buried thermal interfaces, necessitating transient thermometry techniques with picosecond temporal resolution. Although the general principal of picosecond transient optical thermometry is quite similar to the nanosecond approach developed in the previous section, constructing a system that achieves such resolution is much more complicated than the nanosecond approach. A primary objective of this work is the development of a picosecond thermorefectance system suitable for the characterization of nanotube growth interfaces, and the fabrication of sample structures suitable for the growth of CNT films on transparent substrates.

3.1.2 Conduction Regime Considerations for Picosecond Thermorefectance Measurements of CNT Growth Interfaces

Even with the perfect engagement of CNTs with their substrates, the thermal characterization of CNT arrays remains complicated by the low and unknown density of CNT films, and accurate measurements of CNT densities are difficult. A material with a low effective heat capacity and low effective thermal conductivity significantly reduce the sensitivity to measuring a thermal boundary resistance with the film since the poor thermal sinking of heat into the films will dominate the thermal response.

PICOSECOND THERMOREFLECTANCE THERMOMETRY OF MWNT GROWTH INTERFACES

Thus, the sensitivity to accurately extract the thermal resistances of films depends strongly on the sample structure and relative magnitudes of the thermal properties of the films and interfaces. Such problems are particularly acute for CNT films since, even though individual CNTs have a very high thermal conductivity, the low CNT density can significantly reduce the effective heat capacity and thermal conductivity, reducing the thermal effusivity of the film. Thus, extracting and interpreting thermal property data depends strongly on the CNT density and magnitude of the interface resistances.

The relevance and influence of conduction parameters on the transient thermal response of a sample structure can be understood by looking at the conduction regimes. These conduction regimes are captured by a simple thermal circuit model of conduction in metal-coated CNT films in the traditional “top heating” configuration, which is illustrated in Figure 3.1. Similar general considerations hold for thermoreflectance thermometry at a buried interface. As a simple approximation, thermal conduction during a pump probe experiment can be modeled as a lumped-capacitance metal film discharging through a thermal boundary resistance in series with a parallel RC circuit, with a resistance and a capacitance determined by the lumped effective capacitance and effective resistance of the CNT film (Fig. 3.1). Furthermore, these values can evolve over time as the heat diffuses into the CNT arrays during the measurement. The lumped resistance and capacitance per unit area of the CNT film can be approximated as $R_f \sim \sqrt{\alpha_i t} / (\phi k_i)$ and $C_f \sim \phi \sqrt{\alpha_i t} C_{v,f}$, where t is the timescale of the measurement, α_i is the thermal diffusivity of an individual CNT, k_i is the conductivity of an individual CNT, $C_{v,f}$ is the volumetric heat capacity of an individual CNT, and ϕ is the CNT volume fraction. The effective interface resistance is given by $R_i \sim \phi R''_i$, where R''_i is the resistance per unit area of an individual tube. The light yellow area in Fig. 3.1 maps a region for large effective heat capacities of the CNTs (compared to the metal capacitance) or when the CNT thermal resistance is low. In this region, the TBR with the CNT dominates and there is little sensitivity to the other properties of the CNT film. When the interface resistances are

low compared to the CNT volumetric resistance and the heat capacity of the film is low (light blue regime), the thermal properties of the film are dominated by the volumetric resistance of the CNT films. For CNT densities of 1-3%, a maximum measurement time scale for the picosecond technique of ~ 1 ns, a typical metal film thicknesses of tens of nanometers, and a thermal conductivity for the individual CNTs on the order $3000 \text{ Wm}^{-1}\text{K}^{-1}$, the measurement falls in a regime where all properties significantly impact the thermal response, as is illustrated by Fig. 3.1. These conditions complicated the measurement of the TBR by requiring either knowledge of many of the CNT properties or the ability to measure their value. A key objective of this work is a novel extension and modification of the picosecond thermoreflectance technique to provide a means to uniquely extract the CNT and other film properties to isolate the CNT-substrate TBR.

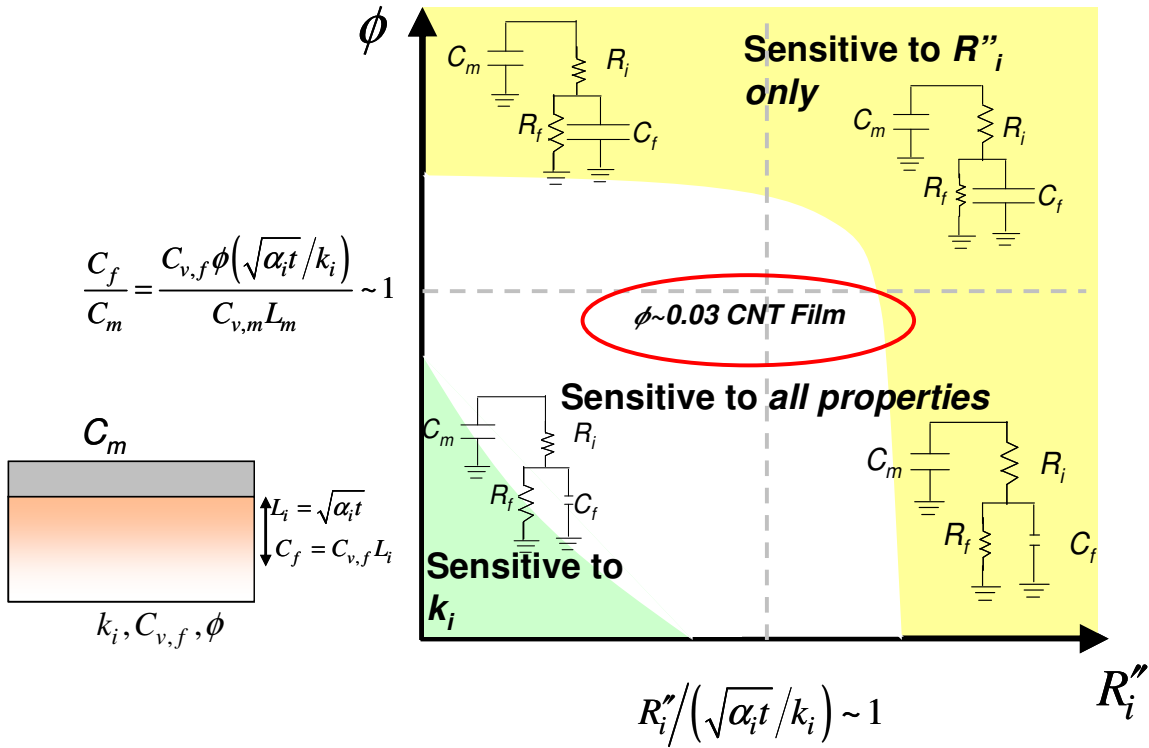


Figure 3.1: The schematic on the left illustrates the canonical thermoreflectance configuration for top heating and the relevant thermal properties. The total resistance (R_f) and capacitance (C_f) of the film depends on the individual CNT conductivity (k_i), heat capacity ($C_{v,f}$), CNT volume fraction (ϕ), CNT diffusivity (α_i), and measurement time scale (t) thorough the diffusion length $L \sim (\alpha_i t)^{1/2}$. The thermal circuit models represent a simple approximation to conduction in the array, where the metal capacitance discharges through an interface resistance into a parallel resistance and capacitance of the CNT film. The plot on the right schematically illustrates the conduction regimes for combinations of CNT capacitance and interface resistances. The size of the circuit elements in the different regimes represents their relative magnitude. For low density CNT films (1-3% vol), the thermal conduction depends strongly on all parameters, complicating data interpretation.

3.2 Multi-frequency Picosecond Time Domain Thermorefectance Technique (TDTR)

3.2.1 Overview of the Picosecond TDTR Technique and System

The picosecond TDTR technique, utilized in the “top-down” surface heating configuration, is an established technique for measuring the thermal interface resistance and properties of thin films, and the system development, signal interpretation, and thermal modeling are described in the literature [54, 81, 115-119]. Although the basic principles of thermorefectance thermometry are similar for all time scales, the implementation and approach for achieving picosecond temporal resolution in practice typically requires utilizing mode-locked lasers combined with optical delay and lock-in techniques. Such an approach adds complexity in optics, data collection, and data interpretation. This work exploits some of these complexities to provide the additional information about the thermal properties of sample structures.

In picosecond TDTR, a periodic train of pulses with duration on the order of picoseconds from a high rep-rate mode-locked laser is focused on and heats the surface of a metal-coated sample structure, changing the optical properties through the change in temperature of the metal [79, 81]. The change in reflectivity of the metal is measured by the change in reflected intensity of a probe pulse train that is picked off from the pump beam and optically delayed using a variable length optical path. Varying the probe delay path reconstructs the transient temperature response of the metal by probing the metal temperature at different delay times with respect the pump pulses. Fitting a model of the observed lock-in signal and temperature response of the structure to the experimental data enables the extraction of unknown properties.

PICOSECOND THERMOREFLECTANCE THERMOMETRY OF MWNT GROWTH INTERFACES

Typically, the high rep-rate pump pulse train is modulated in the MHz range and the induce fluctuation in the probe intensity at this modulation frequency is detected using lock-in techniques. This approach has two primary advantages: 1) lock-in detection enhances the signal-to-noise ratio (SNR) by enabling a low noise, narrow bandwidth steady-periodic measurement at a given optical delay, 2) modulating the pump beam adds additional low frequency (MHz) Fourier components to the heating spectrum in addition to the high frequency components (~ 1 THz) of the picosecond pulses. When there is thermal overlap between pulses, these low frequency components add additional sensitivity of the thermal response (amplitude and phase) to the associated low frequency thermal excitations [54, 116, 118, 119] which probe thermal properties as vastly different length scales within the sample structure compared to the picosecond transients. The subsequent sections present a detailed rigorous analysis of the lock-in signal resulting from the probing of the surface temperature of the material system resulting from a modulated periodic pulse train that accounts for the modulation and pulse accumulation.

Figure 3.2 illustrate the layout of the picosecond TDTR system developed in this work. The heart of the system is a 1 W average-power picosecond mode-locked (SESAM mode-locking) laser emitting 10 ps pulses, with wavelength of 1064 nm at a rep-rate of an 82 MHz. After passing through a Faraday-isolator, a polarizing beam splitter diverts a portion of the pump to the probe path. The remaining pump beam is passed through an electro-optic modulator (EOM) and a fixed optical delay path to allow for time delay matching of the pump and probe paths. The pump beam is then focused into a temperature controlled (50 °C) periodically-poled LiNb crystal for second harmonic generation (SHG) (532 nm) of the pump beam. Frequency doubling the pump allows for easy spectral filtering and spectral separation of the pump and probe beam, which increases the SNR and provides the option to excite carriers in large band-gap materials. An optical SHG bypass path allows for pumping at 1064 nm; however, this approach is challenged by the need to remove the residual pump from the probe signal, which both have a wavelength of 1064 nm. A lens collimates

the output of the SHG and a subsequent spectral notch filter removes any residual fundamental (1064 nm) of the pump beam so as to avoid back-scatter in to the detector. Such back-scatter is particularly troublesome since it is modulated at the EOM frequency, and any leakage of this beam into the detector will swamp the small thermal modulation signal in the probe. The pump then passes through a lens telescope to provide a means to change the beam diameter and focal plane position on the sample surface relative to the probe. The beam is co-aligned with the probe using a dichroic mirror and focused on the sample with an objective (10-50x magnification) to a spot size of ~ 10 microns. Varying the spot size can provided sensitivity to additional properties such as lateral conductivities due to the variation in the lateral conduction with spot size [118].

The probe beam, after being picked off from the pump, passes through a computer-controlled delay stage equipped with a corner cube retroreflector. The probe is then focused into a single mode optical fiber (SMF) which acts as a mode cleaner to covert any alignment and beam characteristic variation associated with the stage motion to amplitude variations that can be measured with a photodetector and divided out of the signal in post-processing [116]. Since the maximum delay time of the picosecond TDTR is limited by beam walking due to stage misalignment and diameter variations due to the stage motion, the inclusion of the SMF greatly increases the capabilities and SNR of the system [116]. Even with perfect alignment, without the SMF, the variations in optical path length of the probe can cause shift in the probe beam at the sample surface, which can significantly affect the data [116]. The probe output of the fiber is collimated and passed though a non-polarizing beam splitter. A portion of the beam is chopped at a low frequency (~ 200 Hz) and collected with photodetector and lock-in amplifier to monitor the output probe intensity to correct for intensity fluctuations and the intensity dependence on the stage position. The reaming probe beam is co-aligned with the pump and focused on the sample surface, typically with a spot size of $\sim 6 \mu\text{m}$. The reflected intensity is collected with and imaging lens

PICOSECOND THERMOREFLECTANCE THERMOMETRY OF MWNT GROWTH INTERFACES

and focused on a CCD for beam imaging and a fast photodetector (17 MHz bandwidth) with a 1064 nm notch filter for probe detection.

The electrical output at the modulation frequency is measured with a RF lock-in amplifier (SRS 844) and the demodulated output is collected by the auxiliary input of a low frequency lock-in (SRS 850) used for the pump and probe amplitude monitoring at the chopper frequency. In theory, the RF lock-in detects the appropriately weighted averages of the odd harmonics of the fundamental modulation frequency since the EOM modulates using a square wave and the RF lock-in uses a square wave mixer. However, in practice the contributions to the signal of the higher harmonics are negligible due to their filtering from the finite bandwidth of the photodiode. The signal, pump amplitude monitor, and probe amplitude monitor data are collected by the SRS 850 which is controlled and coordinated with the delay stage motion using a custom LabView program developed for this work.

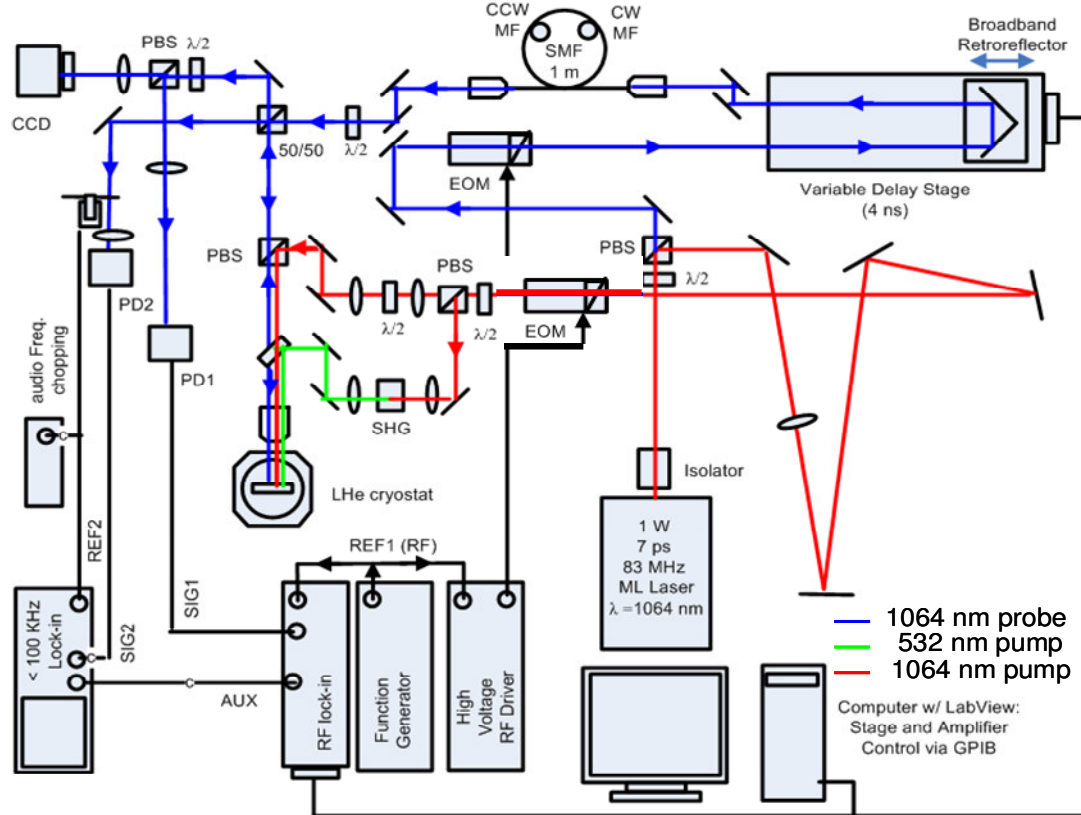


Figure 3.2: Schematic layout of the picosecond TDTR metrology platform developed in this work. See text for detailed explanation of the layout and key features of the system.

The measurement system and thermal model are validated by extracting a thermal conductivity of $1.38 \text{ Wm}^{-1}\text{K}^{-1}$ for a 102 nm thick SiO_2 film coated with 37 nm of Al, which has well known and reliable thermal properties. Figure 3.3 shows representative thermal trace data along with an optimal fit of the thermal model (described in detail in the following sections) to the data over long time-scales (3500 ps). Similarly, the through-substrate measurement approach was verified by measuring samples with well-characterized thermal properties such as SiO_2 substrates coated with 30 nm Al, 25 nm Pt, and $\text{H}_2\text{O}/30 \text{ nm Al}$.

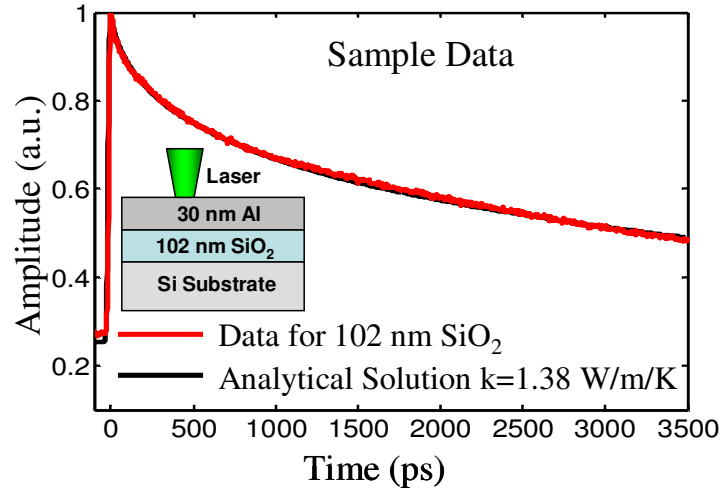


Figure 3.3: Sample thermal trace (black) with a well-characterized and behaved calibration sample consisting of a 102 nm thick thermal SiO₂ film coated with 37 nm of Al on an Si substrate, illustrating and validate measurement systems, technique, and thermal model (red line).

3.2.2 Thermal Model of TDTR Signal for Thermal Property Extraction

3.2.2.1 Interpretation of the Lock-in Signal

The instantaneous change in intensity of a periodic probe pulse train (modeled as delta functions) reflected from the sample structure heated by a modulated periodic pulses is given by [116, 118, 120]

$$\Delta I(t, t_p) = Q_{pump} Q_{probe} \frac{dR}{dT} \sum_{n,m=-\infty}^{\infty} M(n\tau_r) \Delta T(t - n\tau_{rep}) \delta(t - m\tau_{rep} - t_p) \quad (3.1)$$

where Q_{pump} and Q_{probe} are the pump and probe pulse energies, respectively, dR/dT is the coefficient of thermoreflectance, M is the pump modulation function, ΔT is the temperature response per unit pump energy in response to an individual pump pulse, t_p is the delay of the pump with respect to the probe, t is time, and τ_{rep} is the period

between pump pulses. Figure 3.4 illustrates an example of the probe signal represented by Eq. (3.1) and the total thermal response of a sample structure with a simple impulse response of the form $\Delta T \sim \exp(-t/t_d)$, where t_d is the characteristic decay time, resulting from a modulated periodic pump pulse train. The thermal overlap between pump pulses causes heat accumulation and results in a finite pre-pump-pulse temperature and a phase shift between the pump reference and the probe signal.

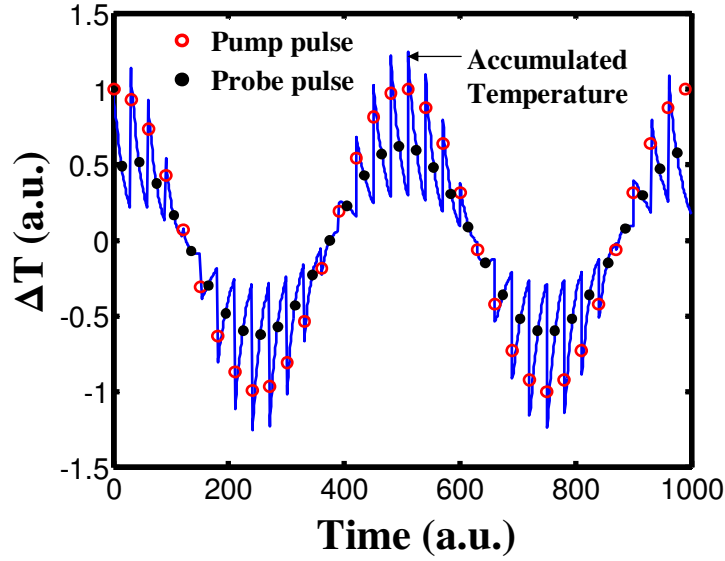


Figure 3.4: Example time-domain thermal response of sample structure with thermal overlap between pulses (solid blue) and probe signal (solid black circle), delayed from the pump, that is generate by a modulated pump pulse train (red squares).

At a fixed delay time, the lock-in amplifier measures the time average power of the probe intensity at the fundamental modulation frequency, Eq. (3.1). Time-averaging Eq. (3.1) and projecting out the component of the signal at the fundamental modulation frequency yields a lock-in signal of [54, 118]

$$V_{LI}(t_p, \omega_{mod}) = \frac{\beta Q_{pump} Q_{probe}}{\tau_p} \sum_n e^{i\omega_{mod}(t_p + n\tau_p)} \Delta T(t_p + n\tau_p) \quad (3.2)$$

PICOSECOND THERMOREFLECTANCE THERMOMETRY OF MWNT GROWTH INTERFACES

where β is a coefficient that contains the thermoreflectance coefficient of the of the sample and ω_{mod} is the modulation frequency. Since the signal of the lock-in is periodic in t_p (probe time delay—not real-time) with the rep rate of the laser, Eq. (3.2) can be Fourier-transformed into frequency components with a fundamental period of τ_p , and recast in a frequency domain form [118, 121]

$$V_{LI}(t_p, \omega_{mod}) = \frac{\beta Q_{pump} Q_{probe}}{\tau_p^2} \sum_{n=-\infty}^{\infty} H(\omega_{mod} + n\omega_0) e^{in\omega_0 t_p} \quad (3.3)$$

where $\omega_0 = 2\pi/\tau_p$, and H is the frequency domain thermal response of the sample structure. Interpreted in the frequency domain, the measurement system multiplies the modulated pump Fourier spectrum with the frequency domain thermal response of the sample, and convolves the resulting product with the probe spectrum with a phase shift factor due to the time delay of the probe. While the interpretation of Eq. (3.2) is more intuitively clear, Eq. (3.3) has the advantage that it does not require calculating the impulse thermal response of the sample, only requiring the frequency domain kernel of the heat diffusion equation, which is typically easier to compute. Eqs. (3.2) and (3.3) clearly indicate a dependence of the lock-in signal on the modulation frequency of the pump, yielding a sensitivity to the to lower frequency harmonic near ω_{mod} in the thermal response in addition to the high frequency components near ω_0 . Eq. (3.2) reveals that both the sensitivity to ω_{mod} and the phase signal between the pump reference and the probe are due to thermal overlap between the impulse responses of the system. Thus, the phase shift data and the negative time delay amplitude depend quite strongly on ω_{mod} , and are thus sensitive to the thermal properties at depths characteristic of $L_d \sim (2\alpha/\omega_{mod})^{1/2}$, where α is the thermal diffusivity of the material. Eq. (3.2) indicates that at $t_p=0$ the derivative of the complex component of the lock-in signal is necessarily zero, which provides a mean to calibrate the phase shift of the electronic components of the system [121]. Eq. (3.3) provides a rigorous analysis of measurement signal once the frequency domain thermal response of the sample, H , is calculated for the specific sample structure.

3.2.2.2 Frequency Domain Response of Stacked Sample Structure

The most general sample geometry for the TDTR approach is a multi-layer film structure with heating at one interface with a Gaussian heat flux distribution, and probing the temperature at the same or another interface with a Gaussian probe profile. The typical geometry employed in the literature consists of surface heating of a multilayer stack, and the thermal analysis for such a structure is discussed in previous work [121]. This work develops a more generic thermal model suitable for modeling TDTR thermal characterization of buried interfaces in CNT films.

Figure 3.5 shows a schematic of the sample structure for the thermal model developed in this work. The thermal model allows for an arbitrary number of material layers of arbitrary thickness, with the ability to heat at an arbitrary interface in the structure and probe at another, potentially different, interface. The model assumes a Gaussian heating profile for both the pump and the probe beam. Heat flux and interface resistance boundary conditions are employed between each layer of the film. The bounding material layers are treated as semi-infinite. Solving for the radial-symmetric heat diffusion equation in response to the heating source provides the temperature at the probe surface, the Gaussian-average of which yields the temperature measured by the probe beam.

The general approach is to solve the heat diffusion equation within a layer of the stack in the frequency domain using a separation of variables technique. A Hankel-Bessel transform addresses the radial component, and a transfer matrix approach addresses the z component. The solution for heating at an internal interface used in this work is adapted from the solution for surface heating of a multilayer stack by splitting the structure (Fig. 3.5) at the interface with surface heating, treating the problem as a simultaneous heat flux into both stacks and superposing the solutions with the proper boundary conditions at the heated interface.

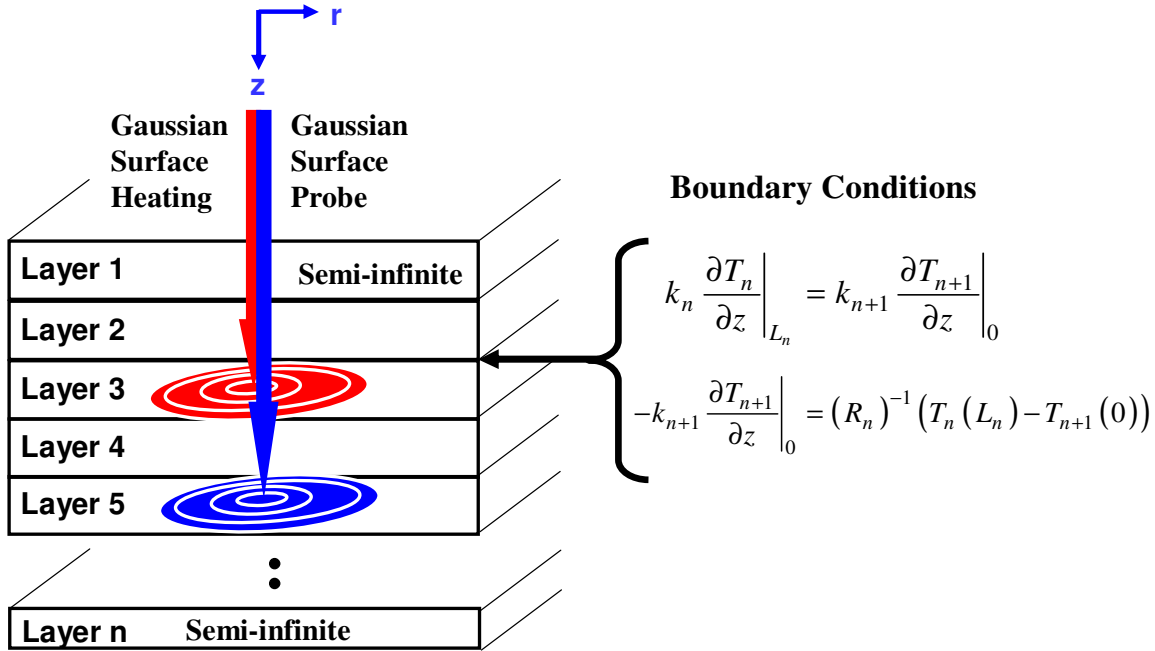


Figure 3.5: Schematic representation of generic multi-layer film structure for the thermal model of the sample structure. The thermal model developed in this work allows for an arbitrary number of layers, N , with Gaussian surface heating at an arbitrary interface and Gaussian temperature probing at an arbitrary interface. The boundary conditions enforce heat flux continuity and allow for interface resistances at all interfaces. The bounding layers are treated as semi-infinite.

The general form of the radial-symmetric heat diffusion equation within the j^{th} layer is

$$\rho_j c_{p,j} \frac{\partial T_j}{\partial t} = \frac{k_{r,j}}{r} \frac{\partial}{\partial r} \left(r \frac{\partial T_j}{\partial r} \right) + k_{z,j} \frac{\partial^2 T_j}{\partial z^2} \quad (3.4)$$

where T_j is the temperature, ρ_j is the density, $c_{p,j}$ is the specific heat, $k_{r,j}$ is the radial thermal conductivity, and $k_{z,j}$ is the thermal conductivity in the z direction. The boundary conditions at the interface between two layers without external heating are

$$-k_z^n \frac{\partial T^n}{\partial z} \Big|_{L_n} = -k_z^{n+1} \frac{\partial T^{n+1}}{\partial z} \Big|_{z_{n+1}=0} \quad (3.5)$$

$$-k_z^{n+1} \frac{\partial T^{n+1}}{\partial z} \Big|_{z_{n+1}=0} = (R_b^n) (T^n(L_n) - T^{n+1}(z_{n+1} = 0)) \quad (3.6)$$

where R_b^n is the boundary resistance between the n^{th} and $n^{th}+1$ layers, and L_n is the thickness of the n^{th} layer. For the layer, N_q , with surface heating the boundary conditions are modified to

$$q''_{pu}(r) - k_z^{N_q} \frac{\partial T^{N_q}}{\partial z} \Big|_{L_{N_q}} = -k_z^{N_q+1} \frac{\partial T^{N_q+1}}{\partial z} \Big|_{z_{N_q+1}=0} \quad (3.7)$$

$$q''_{pu}(r) - k_z^{N_q+1} \frac{\partial T^{N_q+1}}{\partial z} \Big|_{z_{N_q+1}=0} = (R_b^{N_q}) (T^{N_q}(L_{N_q}) - T^{N_q+1}(z_{N_q+1} = 0)) \quad (3.8)$$

where $q''_{pu}(r)$ is the surface heat flux, which in this cases has a Gaussian spatial distribution. Separating the variables and assuming a time-dependent component of form $e^{i\omega t}$ leads to a solution for Eq. (3.4) of the form $T^n = J_0(\lambda r) Z_n(z) e^{i\omega t}$, where $J_0(\lambda r)$ is the 0th order Bessel function of the first kind and

$$Z_n = c_{1,n} e^{\gamma_n z} + c_{2,n} e^{-\gamma_n z} \quad (3.9)$$

Where

$$\gamma_n^2 = \mu_n^2 + \lambda^2 \eta_n \quad (3.10)$$

$$\mu_n^2 = i\omega / \alpha_n \quad (3.11)$$

and where α_n is the diffusivity of the i^{th} material, λ is the radial Eigen value, $\eta_n = k_r / k_z$, $c_{i,n}$ are coefficient determined by the surface heat flux boundary conditions,

Eq. (3.7) and Eq. (3.8). Employing the boundary conditions, Eq. (3.5) and Eq. (3.6), yield the relation between the coefficients in the n and $n+1$ layers,

$$\begin{bmatrix} c_{1,n} \\ c_{2,n} \end{bmatrix} = P_n D_n \begin{bmatrix} c_{1,n+1} \\ c_{2,n+1} \end{bmatrix} \quad (3.12)$$

where

$$P_n = \begin{bmatrix} e^{-\gamma_n L_n} & 0 \\ 0 & e^{+\gamma_n L_n} \end{bmatrix} \quad (3.13)$$

$$D_n = \frac{1}{2\beta_n} \begin{bmatrix} \beta_n + \beta_{n+1} - \kappa_n & \beta_n - \beta_{n+1} + \kappa_n \\ \beta_n - \beta_{n+1} - \kappa_n & \beta_n + \beta_{n+1} + \kappa_n \end{bmatrix} \quad (3.14)$$

With

$$\beta_n = k_{z,n} \gamma_n \quad (3.15)$$

$$\kappa_n = R_b^n \beta_n \beta_{n+1} \quad (3.16)$$

Re-labeling the coefficients $c_{i,j}$ to $d_{i,j}$ for $n < N_q$ for clarity, the temperature rise of the probe surface for the radial eigen component, λ , is

$$G(\lambda) = \frac{P_0}{2\beta_{N_q}} \frac{(d_{1,N_q} + d_{2,N_q})}{(d_{1,N_q} c_{2,N_q} + d_{2,N_q} c_{1,N_q})} (c_{1,N_p} + c_{2,N_p}) \quad (3.17)$$

where N_p is the probe interface and P_0 is the average power. Using the inverse Hankle-Bessel transform for Gaussian heating and probing profiles, and the kernel from Eq. (3.17), yields the frequency domain temperature response measured by the probe required by Eq. (3.3),

$$H(\omega) = \frac{1}{2\pi} \int_0^\infty G(\lambda) \exp\left(-\lambda^2 (w_p^2 + w_q^2)/8\right) \lambda d\lambda \quad (3.18)$$

where w_p and w_q are the probe and pump beam waists, respectively.

Fitting the response of the system, Eq. (3.3), to the experimentally measured thermal response using unknown material properties of the sample structure extracts their value. Figure 3.3 presents example amplitude thermal data measured by the TDTR system along with the evaluation of the thermal model of the system for a 102 nm thick SiO₂ layer coated with 37 nm of Al. This structure acts as a system and thermal model calibration sample since it has known thermal properties. In addition to temperature amplitude, the phase data, which is generated by pulse overlap and modulation of the pump beam, can provide additional information about the thermal properties of the structure. Figure 3.6 presents sample phase data from the SiO₂ calibration sample.

The spatial distribution in location of thermal properties can impact the thermal response uniquely at different time scales as heat diffuses through the sample, which permits the isolation of the properties uniquely. This ability to uniquely extract combinations of multiple thermal properties of a material depends specifically on the independent sensitivity of the thermal response of the system as a function of delay time, which depends strongly on the sample geometry and compositions. Carefully modifying and choosing sample geometries is one approach to increasing sensitivity to desired material properties.

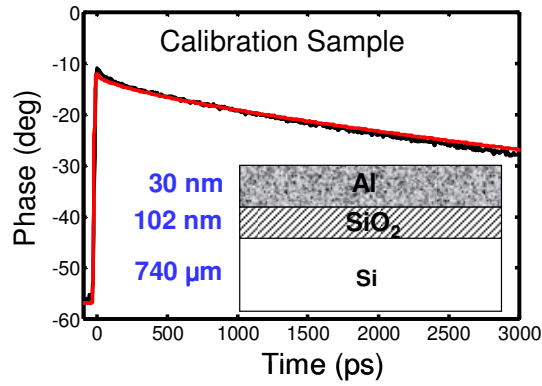


Figure 3.6: Example phase data for calibration sample with well-known thermal properties.

In addition to the temperature transients, the average laser power leads to steady state heating of the structure. This long time-scale heating is dominated by the thermal response of the substrate. Taking the low frequency limit of Eq. (3.18) provides an estimation for the steady-state temperature rise of [122]

$$\Delta T_{ss} = \frac{P_0}{k_s (2\pi (w_p^2 + w_q^2))^{1/2}} \quad (3.19)$$

where k_s is the substrate thermal conductivity. The strong dependence of the steady-state temperature rise on the substrate conductivity and beam radii can lead to significant local heating when using small beam radii ($\sim 10 \mu\text{m}$) and low conductivity substrates. This heating is an important consideration when evaluating the thermal properties in the heat conduction model and interpreting the temperature at which data are taken.

3.3 Sample Preparation for TDTR Measurement of MWNT Growth Interfaces

The samples are prepared by growing MWNT films on metal-coated SiO_2 substrates. The SiO_2 substrates are evaporation-coated with 36 nm of tungsten to act as the temperature transducer, followed by sputtering 35 nm of an amorphous Al_2O_3 layer to facilitate the growth of the MWNTs. The thickness of the transducer was chosen such that it would thermalize during the heating pulses, thus minimizing sensitivity to heat transfer through the film. Using thinner temperature transducers is problematic due to the possibility of optical penetration creating heating in the CNT film. A 3 nm layer coating on the Al_2O_3 layer acts as a catalyst for the MWNT growth. The MWNTs are grown by CVD from an ethane pre-cursor at 850 °C to yield a film thickness of 9 μm , measured with an SEM. Figure 3.7 shows a TEM cross section of the MWNT/ Al_2O_3 / SiO_2 interfaces which provides an accurate measurement of the film thicknesses and an estimation for the MWNT diameter of ~10 nm with a wall thickness of ~2.5 nm. Although the TEM images do not yield a precise value, the images indicate that the MWNT density is low.

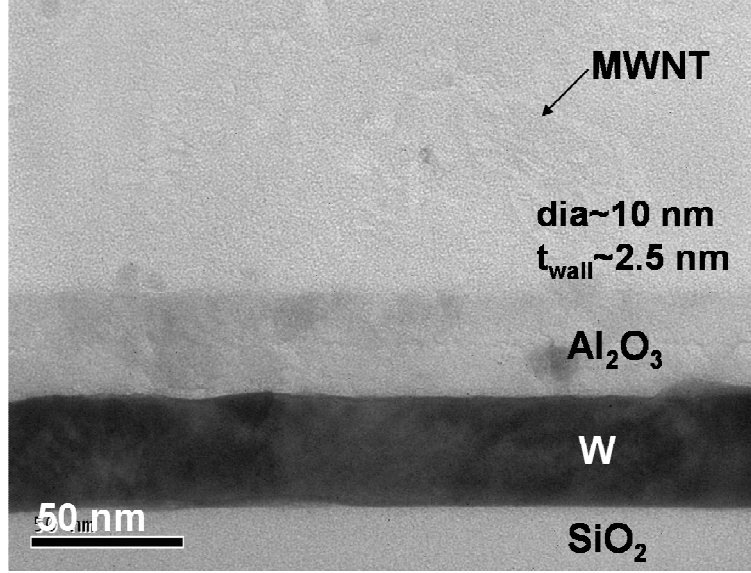


Figure 3.7: Cross-sectional TEM of MWNT interface with an Al₂O₃/W/SiO₂ substrate, illustrating a MWNT diameter of ~10 nm and wall thickness of ~2.5 nm. The TEM provides the thickness of the Al₂O₃ and W films.

3.4 Measurement Results and Data Interpretation

The Al₂O₃ film between the metal transducer and the MWNT interface, and the low and unknown density of MWNTs increase the sensitivity of the thermal response (as described previously) to properties other than the MWNT interface resistances. These additional properties include the W-Al₂O₃ interface resistance, the Al₂O₃ thermal properties, the CNT effective heat capacity, and the CNT effective thermal conductivity. Furthermore, the large thermal penetration depths of the heating Fourier components at the modulation frequency combined with the high frequency picosecond transients complicate the extraction of the thermal interface resistance by creating strong sensitivities to thermal properties at disparate spatial extents in the CNT film (at depths of several microns) compared to the more localized Al₂O₃ and the interfaces. This work provides a technique for the isolation of the MWNT interface resistance and remaining unknown thermal properties by exploiting the dependence of

the TDTR data on the modulation frequency to provide the necessary additional information.

Figure 3.8 presents sample TDTR data for the structure illustrated in Fig. 3.7 for pump beam modulation frequencies of 1, 5, and 8 MHz. Simultaneously fitting the data to the thermal model for all three frequencies extracts the CNT effective heat capacity through the volume fraction, ϕ , the effective MWNT-CNT interface resistance ($R_{eff,MWNT-Al_2O_3}$), and the W- Al_2O_3 interface resistance ($R_{W-Al_2O_3}$). For these particular combinations of material properties and sample geometry, the data only yield a lower bound for the individual MWNT conductivity of $>1200 \text{ Wm}^{-1}\text{K}^{-1}$. Consequently, we assumed this value of $1200 \text{ Wm}^{-1}\text{K}^{-1}$ in the extraction of the remaining properties. Table 3.1 presents the extracted thermal properties. The average power absorbed by the tungsten film during measurement is 10-14 mW, resulting in a local temperature rise of $\sim 500 \text{ K}$, estimated from Eq. (3.19). Consequently, the remaining thermal properties were taken from the literature values [123] evaluated at 800 K. The uncertainty in the values presented in Table 3.1 is due to the combination of this uncertainty in the local temperature combined with the sensitivity to the independent extraction of the unknown thermal properties.

Table 3.1: Extracted properties for the MWNT/ Al_2O_3 /W/ SiO_2 film structure.

R_{eff, Al_2O_3-MWNT}	$150-280 \text{ m}^2 \text{ K/GW}$
Vol. Frac (ϕ)	0.01-0.019
$R_{W-Al_2O_3}$	$3-4.1 \text{ m}^2 \text{ K/GW}$
$k_{ind, MWNT}$	$>1200 \text{ Wm}^{-1}\text{K}^{-1}$
R_{ind, Al_2O_3-MWNT}	$= \phi \times R_{eff} = 1-1.5 \text{ m}^2 \text{ K/GW}$

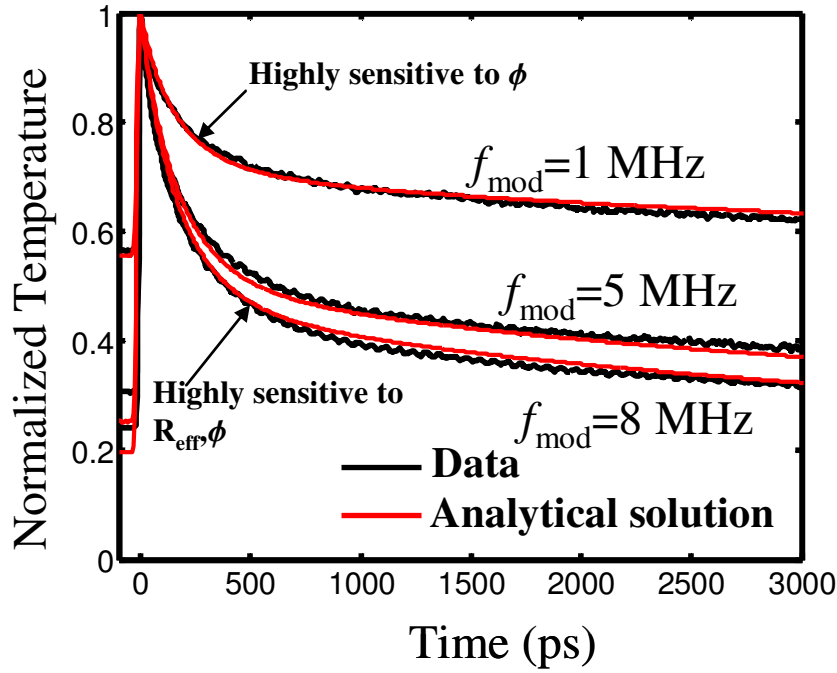


Figure 3.8: TDRT data for the MWNT/Al₂O₃/W/SiO₂ film for pump beam modulation frequencies of 1, 5, and 8 MHz. Simultaneously fitting the data to the thermal model for all three frequencies simultaneously extracts the CNT effective heat capacity through the volume fraction, ϕ , the effective MWNT-CNT interface resistance ($R_{eff,MWNT-Al_2O_3}$), and the W-Al₂O₃ interface resistance ($R_{W-Al_2O_3}$). The low frequency data are most sensitive to the heat capacitance of the MWNT film, and hence the effective volume fraction, while the high frequency data are most sensitive to the thermal properties confined near the temperature transducer. Due to the local self-heating of the lasers, the remaining known thermal properties are evaluated at 800 K.

The frequency dependence of the thermal response on the material properties permits their unique extraction. Features of the low frequency data such as the negative time delay and long-time (>1000 ps) data are strongly sensitive to the total thermal capacitance of the MWNT film, and hence its effective volume fraction, while the high frequency data are most sensitive to R_{eff,Al_2O_3-MWNT} and the thermal properties confined near the temperature transducer. The short-time data (<1000 ps) are most sensitive to $R_{W-Al_2O_3}$ and not the CNT film properties since heat diffusion into the CNT film is limited at these time scales. Thus, the unique approach of this measurement

provides a means to measure the MWNT density and MWNT interface resistance independently.

The effective Al_2O_3 -MWNT interface resistance falls in the range of 100-280 $\text{m}^2\text{K/GW}$, which is about an order of magnitude lower than the resistance of the growth interface and the metallization interface for the metal-coated SWNT films presented earlier in this work. This lower resistance may be due to the elevated temperatures lowering the TBR or an apparent increase in the effective CNT volume fraction when the heat flux is established from the base interface compared to when it is established from the top. Transient measurements of CNT films may measure different effective heat capacities when the heat flux is established from different interface with different CNT engagement factors if the CNTs do not entirely thermalize during the measurement time scales. From the volume fraction, ϕ , and the effective MWNT- Al_2O_3 interface resistance, the resistance of an individual MWNT contact can be estimated from the relation $R_{ind, \text{Al}_2\text{O}_3\text{-MWNT}} \approx \phi \times R_{eff, \text{Al}_2\text{O}_3\text{-MWNT}}$ to be ~1-1.5 $\text{m}^2\text{K/GW}$. This value is about an order of magnitude lower than the experimental data for the SWNT interface resistance data measured earlier in this work, but in reasonable agreement with predictions based on the AMM model presented earlier.

3.5 Summary and Future Directions

This work develops a novel multi-frequency picosecond TDTR system and thermal model suitable for the thermal characterization of buried thermal interfaces in nanotube films. Fitting multi-frequency of TDTR data simultaneously to a thermal model provides a means to measure multiple properties of the MWNT-substrate stack that were previously unattainable using the TDTR system. The results find MWNT interface resistances at the growth interface in the range of 100-180 $\text{m}^2\text{K/GW}$, which are rather low compared to the interface resistances at CNT tips. However, the measurement is complicated by the large temperature rise (~500 K) due to the steady state heating of the low conductivity substrate due to the lasers. This heating prohibits

PICOSECOND THERMOREFLECTANCE THERMOMETRY OF MWNT GROWTH INTERFACES

the measurement of the MWNT interface resistance (and heat capacity) at low temperatures, which would provide novel data for mesoscopic transport between low-dimensional interfaces and semi-infinite media [31, 34]. Future work is to develop sample sets of CNT films grown on high conductivity transparent substrates such as sapphire or MgO to enable low temperature measurements. To amplify the sensitivity to the TBR, the conduction to the substrates can be reduced at sub-nanosecond times scales by the inclusion of a low conductivity thermal buffer layer such as SiO₂ or a multi-layer film with high interface densities between the metal film and the high conductivity substrate. Similarly, varying the CNT density and length can provide increased sensitivity to desired properties along with an understanding of the dependence of the TBR on these properties.

Chapter 4

Thermal Resistance between Low-Dimensional Nanostructures and Semi-Infinite Media

4.1 Introduction

Nanostructured electronic and photonic devices typically contain materials with nanoscale dimensions that interface with larger micro or macrostructures at scales comparable to the phonon wavelength. These abrupt junctions between materials with differing dimensionality often arise because of the need to interface the nanosystem with the macro environment or thermal reservoirs. Examples of such geometry include recent experimental work measuring localized heating as a function of length of a single hydrocarbon molecule bonded between two electrodes [124], or the use of micro-fabricated suspended bridges coupled to large cavities for studying the quantized nature of thermal conductance [125]. Similarly, suspending an isolated carbon nanotube between two reservoirs is a common technique to study its thermal and electrical properties. This measurement geometry has yielded a variety of data such as thermal and electrical conductivities [40, 60, 126] as well as shown interesting properties such as thermal rectification arising from non-linear contact effects [127]. Recent experimental work on bulk arrays of aligned carbon nanotubes for thermal management applications revealed that nanoscale contact effects significantly reduce the thermal performance of the nanotube structures [69, 128].

THERMAL RESISTANCE BETWEEN LOW-DIMENSIONAL NANOSTRUCTURES AND SEMI-INFINITE MEDIA

Low temperature phonon transport through three dimensional point-contacts ranging in scale from a few nanometers to 1000 nm was reviewed by Feher *et al.* [11] In addition to the emergence of size and ballistic transport effects for contact dimensions less than 1000 nm, the work discussed the emergence of phonon diffraction effects on thermal transport through nanoscale contacts (~100 nm) at low temperatures ($T \sim 1$ K) [129, 130]. For contact dimensions less than 10 nm, this work highlighted the impact of the crystal geometry and surface effects in modifying the phonon spectral densities. In particular, the work demonstrated the modification in local phonon density of states for atoms located on the center plane of square atomic bridge structures with FCC crystal structure and edge lengths of 6 and 12 lattices constants bridging semi-infinite FCC crystals. The consequences of the modified phonon states on the thermal resistances in the structure were left unexplored.

Previous work modeling the thermal transport through abrupt nanoscale contacts has employed both continuum mechanics approaches and atomistic simulations. Research specifically focusing on the phonon transmission through an abrupt junction has relied extensively on continuum mechanics approaches, which are valid in the long wavelength limit and which normally apply at low temperatures. In this approach, the energy transmission through the junction is typically computed through a Green's function solution of the continuum equations of motion across the junction. Angelescu *et al.* [17] analyzed the energy transmission coefficient for an abrupt junction between two continuum 2D rectangular mediums by applying scalar wave mechanics with fixed boundaries, letting the width of one cavity tend to infinity. Cross and Lifshitz [32] analyzed the same geometry but assumed a more realistic stress-free boundary condition on all free surfaces, predicting a linear scaling of the transmission coefficient with frequency for all transverse bridge modes. The work also analyzed the junction using a long wavelength approximation to the full vector mechanics theory, which included the contributions of localized Rayleigh-like surface states to the energy transmission. Continuum analysis in full scalar and long wavelength perturbative vector approaches with stress-free boundary conditions has

also been extended to 3D abrupt junctions in rectangular [33] and cylindrical geometries [31, 131]. The prior continuum work suggests that the free surface created at an abrupt junction can significantly alter phonon modes that participate in heat transfer, creating additional contributions to the thermal resistance of the structure.

Atomistic modeling approaches provide a more detailed framework to model transport in nanostructures and directly include quantum effects. The majority of atomistic modeling of nanoscale interfaces has focused on computing the energy transmission through a one dimensional atomic lattice linking two thermal reservoirs [20, 132-135]. The simulations provide a detailed analysis of the transport physics through the atomic structure, but typically employ approximations to incorporate the affect of the reservoir contact on energy transmission through the structure. For example, Ohtsubot *et al.* [132] used classic molecular dynamics simulations to investigate the energy transmission through a 1D atomic lattice by approximating the reservoir contacts as adiabatic.

The study of quantum transport through atomic structures using Hamiltonian and Green's function techniques has incorporated more rigorous modeling of the contact physics. Approximation techniques to incorporate reservoir interface effects have included using the Debye density of state approximation within the Landauer formalism [133], the continuum-based local surface density of states (LDOS) in the Hamiltonian [134] and non-equilibrium Green's function (NEGF) formalism[20], and a finite extension of the atomic structure into the reservoir using the Hamiltonian formalism [135]. Incorporating the dynamics of the reservoir as a finite extension of the atomic system [135] showed significant impact on phonon transport through the system such as reduced transmission of transverse phonon modes. However, the computational constraints on the size reservoir domain limited its dimension to scales comparable to the phonon wavelength, which may inadequately capture the entire impact of the reservoir dynamics. Similarly, the LDOS approximation based on

THERMAL RESISTANCE BETWEEN LOW-DIMENSIONAL NANOSTRUCTURES AND SEMI-INFINITE MEDIA

continuum theory may be inadequate to represent the true LDOS of an atomic contact, particularly for higher frequency phonon modes.

The prior atomic scale and continuum modeling indicates that the details of the reservoir dynamics modify the energy transmission in nanoscale structures. Rigorous modeling of phonon transmission through an abrupt nanoscale contact presents a multi-scale computational challenge, requiring detailed analysis of an atomic scale structure connected to a macro scale reservoir.

This work uses a lattice dynamics calculation between a 1D harmonic lattice and a 3D FCC lattice, and between a 1D and 2D square lattice to provide perspective on the impact of phonon reservoir modes on thermal transport through an abrupt nanoscale junction. The lattice dynamic approach to predicting thermal boundary resistances has been applied to a variety of interfaces between lattices of similar dimensionality [19, 136]. To our knowledge, it has not been applied to the prediction of interface resistances between lattices of differing dimensionality. The approach presented here provides a rigorous solution of the lattice dynamics in this simplified model for an atomic point contact at all phonon wavelengths, within the assumptions of the model. We use the simplified geometry studied here to discuss the qualitative behavior of thermal transport through more practical geometries involving carbon nanotubes, silicon nanopillars, and graphene.

4.2 Model

4.2.1 Model Overview and Interface Geometry

This work uses a lattice dynamic analysis to investigate the phonon transmission through the two junctions geometries depicted in Fig. 4.1. In the first case, a 1D harmonic lattice is bonded to an individual atom on the (001) surface of a semi-infinite FCC lattice extending in the positive z direction with nearest-neighbor harmonic interactions. The mass of the atoms in the FCC lattice is M_2 and they interact through the nearest-neighbor axial (K_2^a) and shear (K_2^s) stiffnesses. In the second case, the 1D lattice bonds to the (01) surface of a 2D square lattice with second nearest-neighbor harmonic interactions. We consider atomic motion confined to the plane with nearest-neighbor axial and shear stiffnesses (K_2^a , K_2^s) and second nearest-neighbor axial and shear stiffness (K_d^a , K_d^s) along the unit cell diagonal. In the 1D lattice, we consider nearest neighbors interactions between the atoms with mass M_1 , characterized by axial and shear (K_l^a , K_l^s) bond stiffness. At the interface contact, the lattices interact through a nearest neighbor interaction with axial and shear (K_c^a , K_c^s) bond stiffness constants, which can potentially differ from those in either of the bulk domains. We choose values for the bond parameters that yield the Lamé constants in the continuum limit [137] of the 2D lattice. To simplify the analysis, we neglect the bond torsion stiffness, assume that equilibrium positions of the atoms near the interface retain the bulk lattice structure (c.f. Ref. [138] for discussion of surface structure modification effects), and assume that there are no foreign species bonded on the interface surface. Because the linear elastic continuum equations of motion (c.f. Ref. [139]) for a medium couple the displacement field components, consistency between the 2D square lattice and its continuum limit motivates the need to include second nearest neighbor interactions for this lattice.

*THERMAL RESISTANCE BETWEEN LOW-DIMENSIONAL NANOSTRUCTURES
AND SEMI-INFINITE MEDIA*

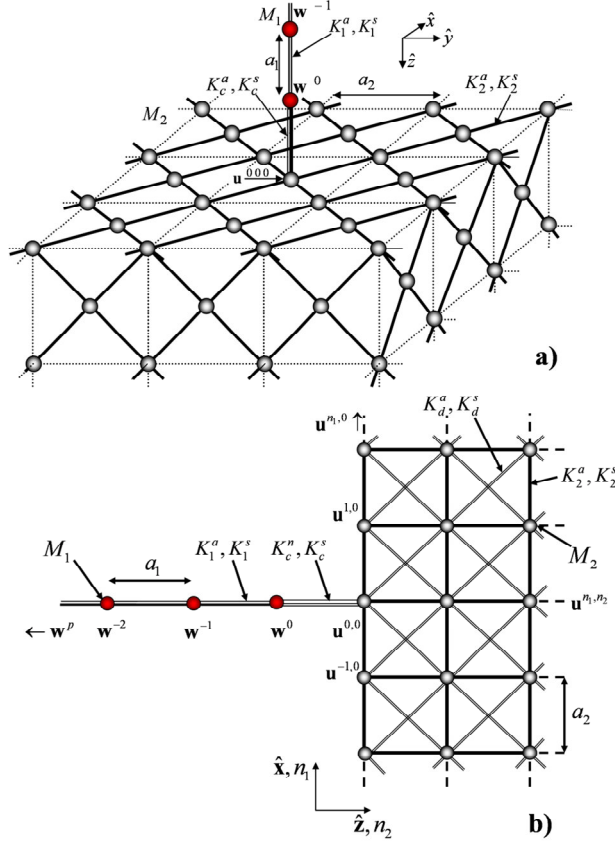


Figure 4.1: Schematic illustration of the lattice geometry used in this study a) junction between a 1D lattice and the (001) surface of semi-infinite FCC lattice extending in the positive z direction. b) junction between 1D lattice and the (01) surface of a semi-infinite 2D square lattice extending in the positive z direction.

From the perspective of the semi-infinite lattice, the phonon mode incident from the 1D domain appears as a localized steady periodic source radiating at the surface. The response of an elastic continuum half space to either a point source or line source was first studied by Lamb [140]. Others have studied finite radiating sources of various geometries [141-144]. In general, the effect of a localized radiating surface source is to produce an excitation composed of a superposition of bulk modes that is highly localized along the free interface. The continuum mechanics analogy with the point like surface interaction in this work suggests that the modes in the 1D lattice will couple strongly to a superposition of modes in the semi-infinite lattice that are localized near the surface. Consequently, the local density of states of the atomic point

contact with the discrete lattice is expected to differ from both the bulk density of states and the continuum free-surface approximation to the local density of states. The modification in the LDOS will affect the energy transmission and thermal conductance of the interface. In particular, the transmission coefficient will be less than unity, even for a junction between materials with identical bulk lattice properties.

We calculate phonon transmission using a Green's function approach as follows. We first solve for the Green's function for the response of the semi-infinite lattice to a harmonic point force on the surface, and then find the coupling of that force to the 1D lattice modes. The first step in computing the surface Green's function is to find the bulk eigenmodes in the semi-infinite lattice and their associated dispersion relation for a given frequency ω . The equations of motion for surface atoms in response to harmonic forces spatially distributed along the surface with arbitrary spatial frequency provide boundary conditions to be satisfied by a superposition of bulk modes. Then, an appropriate superposition of these solutions yields the response of the semi-infinite lattice to a harmonic point force of frequency ω localized on the atom at the index origin, $(n_1, n_2, n_3) = (0, 0, 0)$. The boundary conditions of the junction relate this point force to the 1D lattice dynamics to determine the amplitude ratios of the reflected modes in the 1D lattice and the transmitted modes in the semi-infinite lattice to the incident mode in the 1D lattice. The difference between the energy of the incident wave and the reflected wave is the energy that is transmitted across the interface, which gives the frequency dependent transmission coefficient of the junction.

4.2.2 Surface Green's Function for Semi-infinite Lattice

Prior research investigating the dynamics of semi-infinite lattices has considered 1D lattices [145], 2D square lattices with second nearest neighbor interactions [137], 2D hexagonal lattices [146], and 3D lattices [147, 148]. In this section, we present our formulation for constructing the surface Green's function for the semi-infinite FCC lattice. The 2D case follows an analogous approach and the details for computing the

*THERMAL RESISTANCE BETWEEN LOW-DIMENSIONAL NANOSTRUCTURES
AND SEMI-INFINITE MEDIA*

lattice dynamics of a square lattice with second nearest neighbor interaction and finite extent were studied by Suiker [137]. Because our analysis of a semi-infinite 2D domain differs mainly in the boundary conditions, we will refer the reader to Ref. [137] for the details of the calculations for the 2D case.

We represent the atomic displacement of the atoms in the FCC lattice by $\mathbf{u}^{n_1, n_2, n_3}$ for the atom located at $\mathbf{R} = n_1 \mathbf{a}_1 + n_2 \mathbf{a}_2 + n_3 \mathbf{a}_3$, where the primitive lattice vectors are

$$\mathbf{a}_1 = \frac{a_2}{2}(\hat{\mathbf{y}} + \hat{\mathbf{z}}), \quad \mathbf{a}_2 = \frac{a_2}{2}(\hat{\mathbf{z}} + \hat{\mathbf{x}}), \quad \mathbf{a}_3 = \frac{a_2}{2}(\hat{\mathbf{x}} + \hat{\mathbf{y}}), \quad (4.1)$$

and where a_2 is the lattice constant of the conventional cell. The equations of motion are

$$M_2 \ddot{\mathbf{u}}^{n_1, n_2, n_3} = - \frac{\partial U}{\partial \mathbf{u}^{n_1, n_2, n_3}} \quad (4.2)$$

where U is the crystal potential energy. For harmonic nearest-neighbor axial (K_2^a) and shear stiffness (K_2^s) interactions, U is given by

$$U = \sum_{m_1, m_2, m_3 = n.n.} \frac{1}{2} K_2^a (\Delta \mathbf{l}^{m_1, m_2, m_3})^2 + \frac{1}{2} K_2^s (\Delta \mathbf{s}^{m_1, m_2, m_3})^2 \quad (4.3)$$

where the sum runs over the indices of the nearest neighbors (n.n.) of the atom located at (n_1, n_2, n_3) and where $\Delta \mathbf{l}^{m_1, m_2, m_3}$ and $\Delta \mathbf{s}^{m_1, m_2, m_3}$ are the inter-atomic axial stretch and shear displacements that are given by

$$(\Delta \mathbf{l}^{m_1, m_2, m_3})^2 = \left((\mathbf{u}^{m_1, m_2, m_3} - \mathbf{u}^{n_1, n_2, n_3}) \bullet \hat{\mathbf{d}}^{m_1, m_2, m_3} \right)^2 \quad (4.4)$$

$$(\Delta \mathbf{s}^{m_1, m_2, m_3})^2 = (\mathbf{u}^{m_1, m_2, m_3} - \mathbf{u}^{n_1, n_2, n_3})^2 - \left((\mathbf{u}^{m_1, m_2, m_3} - \mathbf{u}^{n_1, n_2, n_3}) \bullet \hat{\mathbf{d}}^{m_1, m_2, m_3} \right)^2 \quad (4.5)$$

where $\hat{\mathbf{d}}^{m_1, m_2, m_3}$ is unit vector along the inter-atomic bond direction. Equation (4.2) is solved by assuming a solution of the form

$$\mathbf{u}_j^{n_1, n_2, n_3} = \mathbf{C}_j e^{i(\mathbf{R} \cdot \mathbf{k}_j - \omega t)} \quad (4.6)$$

where

$$\mathbf{R} \cdot \mathbf{k}_j = \frac{a_2}{2} ((n_2 + n_3)k_x + (n_1 + n_3)k_y + (n_1 + n_2)k_{z,j}) = \mathbf{R} \cdot (\mathbf{k}_{\parallel} + k_{z,j}\hat{\mathbf{z}}) \quad (4.7)$$

where \mathbf{C}_j are the Cartesian displacement amplitudes components and k_x , k_y , and $k_{z,j}$ are the Cartesian components of the wavevector. We denote the projection of the wavevector, \mathbf{k} , on the plane of the free interface as \mathbf{k}_{\parallel} and the component in the semi-infinite direction as $k_{z,j}$. The subscript “ j ” labels the three degenerate solutions that will arise from the solution of Eq. (4.2) for a given choice of \mathbf{k}_{\parallel} and ω , corresponding to generalized longitudinal and transverse waves. In general, the presence of the free interface will cause $k_{z,j}$ to be complex valued.

Substituting Eq. (4.6) into Eq. (4.2) yields the following three-by-three system of equations whose solution gives the dispersion relation and amplitude component ratio for the three degenerate bulk modes,

$$[M_2\omega^2\mathbf{I} + \mathbf{D}]\mathbf{C}_j = \mathbf{0} \quad (4.8)$$

Where

$$D_{11} = 4K_2^s(bc_j - 1) + 4\left(\frac{K_2^n + K_2^s}{2}\right)(ab + ac_j - 2) \quad (4.9)$$

$$D_{22} = 4K_2^s(ac_j - 1) + 4\left(\frac{K_2^n + K_2^s}{2}\right)(bc_j + ab - 2) \quad (4.10)$$

*THERMAL RESISTANCE BETWEEN LOW-DIMENSIONAL NANOSTRUCTURES
AND SEMI-INFINITE MEDIA*

$$D_{33} = 4K_2^s(ba - 1) + 4\left(\frac{K_2^n + K_2^s}{2}\right)(bc_j + ac_j - 2) \quad (4.11)$$

$$D_{12} = D_{21} = -4\left(\frac{K_2^n - K_2^s}{2}\right)\left(\sin\left(\frac{k_x a_2}{2}\right)\sin\left(\frac{k_y a_2}{2}\right)\right) \quad (4.12)$$

$$D_{13} = D_{31} = -4\left(\frac{K_2^n - K_2^s}{2}\right)\left(\sin\left(\frac{k_x a_2}{2}\right)\sin\left(\frac{k_{z,j} a_2}{2}\right)\right) \quad (4.13)$$

$$D_{23} = D_{32} = -4\left(\frac{K_2^n - K_2^s}{2}\right)\left(\sin\left(\frac{k_y a_2}{2}\right)\sin\left(\frac{k_{z,j} a_2}{2}\right)\right) \quad (4.14)$$

where

$$a = \cos\left(\frac{k_x a_2}{2}\right), \quad b = \cos\left(\frac{k_y a_2}{2}\right), \quad c_j = \cos\left(\frac{k_{z,j} a_2}{2}\right) \quad (4.15)$$

Since the Fourier space approach to constructing the surface Green's function requires superposing the bulk modes to solve for the response of the half space to a periodic surface force with the in-plane wavevector \mathbf{k}_{\parallel} and frequency ω , it is convenient to take the determinant of Eq. (4.8) and solve for $k_{z,j}$ in terms of \mathbf{k}_{\parallel} and ω to yield explicit relations for bulk displacement fields (Eq. (4.6)) in terms of these variables. Taking the determinant of Eq. (4.8) and solving for $k_{z,j}$ yields an explicit third order polynomial in c_j . The subscript “ j ” indexes the three roots of this polynomial, which lead to six values of $k_{z,j}$ corresponding to

$$k_{z,j} = \pm \frac{2}{a_2} \arccos(c_j) \quad (4.16)$$

In analyzing energy transmission into the semi-infinite lattice from the localized surface excitation, we will apply the radiation boundary condition in which we choose the wave vectors that correspond to modes that carry energy away from interface and are finite in the positive z direction. Because $k_{z,j}$ are in general complex valued, this boundary condition requires that the three physically acceptable solutions to Eq. (4.16)

have positive imaginary components. With $k_{z,j}$ in terms of \mathbf{k}_{\parallel} and ω , solving Eq. (4.8) for the ratio of the x and y to z components of the three bulk modes gives

$$\chi_{xj} = \frac{C_{x,j}}{C_{z,j}} = -\frac{(D_{23}(D_{11} + M_2\omega^2) - D_{13}D_{21})}{(D_{22}(D_{11} + M_2\omega^2) - D_{21}^2)} \quad (4.17)$$

$$\chi_{yj} = \frac{C_{y,j}}{C_{z,j}} = -\frac{(D_{23}D_{12} - D_{13}(D_{22} + M_2\omega^2))}{(D_{21}^2 - D_{22}(D_{11} + M_2\omega^2))} \quad (4.18)$$

$$\chi_{zj} = 1 \quad (4.19)$$

The next step to constructing the surface Green's function is to compute the response of the lattice to a harmonic surface force with spatial frequency \mathbf{k}_{\parallel} . The equations of motion for the atoms at the surface provide boundary conditions, which are satisfied by a superposition of the degenerate bulk modes at frequency ω . Then, an appropriate superposition of the response of the semi-infinite lattice to a spatially periodic force will yield the response of the semi-infinite lattice to a temporally harmonic point force located at $(n_1, n_2, n_3) = (0, 0, 0)$. The equations of motion for the surface atoms are

$$M_2 \ddot{\mathbf{u}}^{n_1, n_2, n_3} = -\frac{\partial U_s}{\partial \mathbf{u}^{n_1, n_2, n_3}} + \mathbf{F}^{n_1, n_2, n_3} \quad (4.20)$$

where $\mathbf{F}^{n_1, n_2, n_3}$ is the external force acting on the surface atom at (n_1, n_2, n_3) , U_s is the potential energy for an atom on the (001) surface, and (n_1, n_2, n_3) are restricted to surface sites. Assuming that the lattice retains its bulk structure and bond stiffnesses at the surface, and that there are no interactions arising from the negative z half-space, the potential energy for atoms on the surface sites, U_s , is

$$U_s = \sum_{m_1, m_2, m_3 = n.n. \ z \geq 0} \frac{1}{2} K_2^a (\Delta \mathbf{l}^{m_1, m_2, m_3})^2 + \frac{1}{2} K_2^s (\Delta \mathbf{s}^{m_1, m_2, m_3})^2 \quad (4.21)$$

THERMAL RESISTANCE BETWEEN LOW-DIMENSIONAL NANOSTRUCTURES AND SEMI-INFINITE MEDIA

where the sum runs only over atoms with positions on the surface and in the positive z direction. We assume a force distributed along surface of the form

$$\mathbf{F}^{n_1, n_2, n_3} = \mathbf{f}(\mathbf{k}_{\parallel}) e^{i(\mathbf{k}_{\parallel} \cdot \mathbf{R} - \omega t)} \quad (4.22)$$

where \mathbf{R} is confined to surface and \mathbf{f} is the amplitude of the force. We seek a solution to Eq. (4.20) that is a superposition of the three degenerate bulk modes with wavevector \mathbf{k}_{\parallel} and frequency ω ,

$$u_i^{n_1, n_2, n_3}(\mathbf{k}_{\parallel}) = \left(\sum_{j=1}^3 A_j \chi_{ij} e^{i \left(\frac{k_{z,j} a_2}{2} (n_1 + n_2) \right)} \right) e^{i(\mathbf{k}_{\parallel} \cdot \mathbf{R} - \omega t)} \quad (4.23)$$

where A_j are the amplitude coefficients of each of the three degenerate bulk modes. Substituting Eq. (4.22) and Eq. (4.23) into Eq. (4.20) gives a three by three system of equations to be solved for the amplitude coefficients, A_j ,

$$\mathbf{H}\mathbf{A} = -\mathbf{f}, \quad H_{ij} = \chi_{ij} M_2 \omega^2 - \left[\frac{\partial U_s}{\partial u_i^{n_1, n_2, n_3}} \right]_j \quad (4.24)$$

where the last term is interpreted as individually evaluating the i^{th} component of the gradient of the inter-atomic potential for a surface atom with respect to $\mathbf{u}^{n_1, n_2, n_3}$ with the j^{th} term in Eq. (4.23). Then, we can construct a force localized on the atom at $(n_1, n_2, n_3) = (0, 0, 0)$, namely $F_i^{n_1, n_2, n_3} = F_i \delta_{n_1, 0} \delta_{n_2, 0} \delta_{n_3, 0}$, where F_i is the magnitude of the i^{th} component of the force acting on the atom at $(0, 0, 0)$ and $\delta_{n_i, 0}$ is the Kronecker-Delta, by choosing the Fourier components of Eq. (4.22) to be $\mathbf{f}_i(\mathbf{k}_{\parallel}) = F_i$ and integrating Eq. (4.23) over the two dimensional (001) surface Brillouin zone with a density of states of $A_{cell}/(2\pi)^2$, where A_{cell} is the direct-space area of the (001) primitive surface unit cell. Superposing the Fourier space solutions, the total displacement amplitude for the point force is then given by

$$\mathbf{u}^{n_1, n_2, n_3} = \iint_{(001) \text{ b.z.}} \frac{A_{\text{cell}}}{(2\pi)^2} \mathbf{u}^{n_1, n_2, n_3}(\mathbf{k}_{\parallel}) d\mathbf{k}_{\parallel} \quad (4.25)$$

In calculating the energy transmission to the semi-infinite lattice, we assume that the 1D lattice only interacts with the displacement of the atom located at (0,0,0), which simplifies Eq. (4.25) to only evaluating the $(n_1, n_2, n_3)=(0,0,0)$ term. Thus, the displacement of the atom at the origin of the semi-infinite lattice is related to the external force (\mathbf{F}) on that atom by

$$\mathbf{u}^{0,0,0} = \mathbf{G}\mathbf{F}, \quad (4.26)$$

with

$$\mathbf{G} \equiv - \iint_{(001) \text{ b.z.}} \frac{A_{\text{cell}}}{(2\pi)^2} \chi \mathbf{H}^{-1} d\mathbf{k}_{\parallel} \quad (4.27)$$

when evaluating the integral in Eq. (4.27), we causally perturb the vibration frequencies to $\omega^2 \rightarrow \omega^2 + i\delta$ in the limit as $\delta \rightarrow 0^+$, where δ is a small number that related to the energy resolution of \mathbf{G} and whose physical significance is discussed in Ref. [149]. We use δ of the form recommended by Ref. [150], specifically ω_{max}

$$\delta = 0.02 \left(1 - \frac{\omega}{\omega_{\text{max}}} \right) \omega^2 \quad (4.28)$$

where ω_{max} is the maximum lattice vibration frequency. Smaller values of δ increase the energy resolution at the expense of computational time. Physically, \mathbf{G} can be interpreted as the Green's function for a surface atom since G_{ij} represents the displacement in the i^{th} direction of a surface atom in response to a localized force on that atom in the j^{th} direction. Due to the appearance of \mathbf{H}^{-1} in Eq. (4.27), large contributions to the integral arise from wavevector with \mathbf{k}_{\parallel} such that $\det(\mathbf{H}) \sim 0$, which, in light of Eq. (4.24), occurs when there is near zero surface force. This condition is

THERMAL RESISTANCE BETWEEN LOW-DIMENSIONAL NANOSTRUCTURES AND SEMI-INFINITE MEDIA

equivalent to free surface modes, which are localized near the interface, analogous to Rayleigh surface waves in the continuum[139], indicating that these localized modes strongly contribute in the phonon coupling from the 1D lattice to the semi-infinite lattice.

Symmetry of the equations of motion under the transformation $x \leftrightarrow y$ implies that $G_{xx}=G_{yy}$ and $G_{xz}=G_{yz}$. Mirror symmetry about the x and y axis implies that $G_{xy}=G_{yx}=G_{xz}=G_{yz}=0$, which numerical evaluation of \mathbf{G} confirmed. Similarly, numerical evaluation \mathbf{G} shows that $|G_{zx}|, |G_{zy}| \ll |G_{xx}|, |G_{zz}|$ for all frequencies, indicating that the in-plane forces weakly couple to normal displacements of the surface. Consequently, the reflection of energy from a longitudinal polarization incident from the 1D lattice into transverse polarizations is weak, and similarly for energy reflected from transverse polarization incident from the 1D lattice into longitudinal polarizations. The local density of states (LDOS), ρ , for an atomic site on the surface the surface is related to the Green's function through the relation [150, 151]

$$\rho = \frac{-M_2 2\omega}{\pi} \lim_{\delta \rightarrow 0^+} \left(-\text{Im} \left(\mathbf{G}(\omega^2 + i\delta) \right) \right) \quad (4.29)$$

where the additional negative sign arises due to our sign convention in defining the Green's function, and the mass factor from our definition of the dynamic matrix.

We verified the calculation by comparing the form of the local density of states to that of palladium [151] and by comparing the numerical evaluation of \mathbf{G} for the 2D lattice in the low frequency limit with the analogous continuum solution given in Ewing *et al.* [144]. Figure 4.2 compares the LDOS evaluated using Eq. (4.29) for the simple two parameter model of an Si-like material developed in the work with calculations by Treglia *et al.* [152] using a more complicated four parameter recursive technique for Pd and Ni FCC lattices. The similarity in the structure of the LDOS indicates that this simple model captures the essential features of the LDOS rather well and provides validation for the model. Figure 4.3 illustrates the impact of increased stiffness scaling of the bond stiffness on the surface site LDOS. Increasing the

stiffness decreases the LDOS and stretches out the features in the LDOS to higher frequencies. Figure 4.3b illustrates the quadratic power law behavior of the LDOS which is predicted by continuum theory [153] and provides further validation for the model.

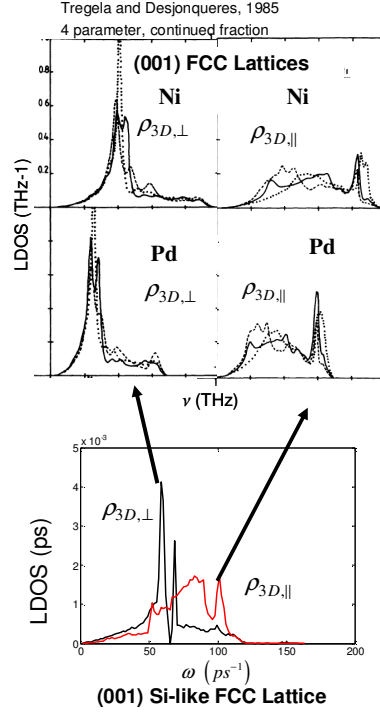


Figure 4.2: Comparison of the calculated value of the LDOS given by Eq. (4.29) using the two parameter model for the Si-like FCC lattice in this work (bottom) with calculations by Treglia *et al.* [152] using a four parameter recursive technique for Pd and Ni FCC lattices. The similarity in the structure of the LDOS indicate that this simple model captures the essential features of the LDOS and provide validation for the model.

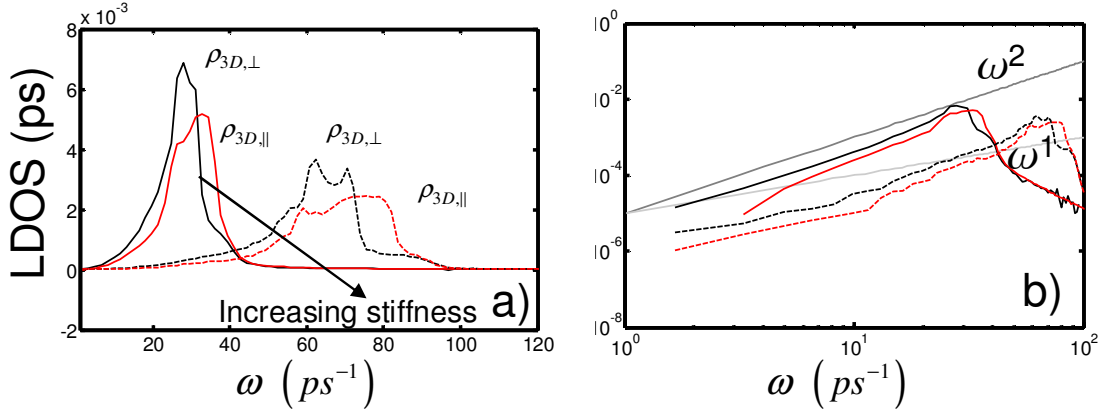


Figure 4.3: a) Illustration of impact of increasing the bond stiffness parameters on the surface LDOS, which show that increasing the bond stiffness reduces the magnitude of the LDOS and stretches and flattens the features. b) Log-log plot of the LDOS in (a) showing quadratic low-frequency behavior which is predicted by continuum theory [153] and provides further validation for the model.

4.2.3 Energy Transmission between the 1D and Semi-infinite Lattices

The interaction of the semi-infinite lattice with the 1D lattice through the coupling constants K_c^a and K_c^s (Fig. 4.1) gives the forces F_i imposed on the semi-infinite lattices

$$\mathbf{F} = \mathbf{S}_c (\mathbf{w}^0 - \mathbf{u}^{0,0,0}), \quad \mathbf{S}_c = \begin{bmatrix} K_c^s & & \\ & K_c^s & \\ & & K_c^a \end{bmatrix} \quad (4.30)$$

where \mathbf{w}^p are the amplitude components for the atom at site p in the 1D lattice, with $p=0$ indexing the atom that interacts with the semi-infinite lattice through the bond stiffnesses \mathbf{S}_c , and with p decreasing along the negative z direction. Combining Eq. (4.30) and Eq. (4.26) relates the displacements in the semi-infinite lattice to those in the 1D lattice,

$$\mathbf{u}^{0,0,0} = (\mathbf{I} + \mathbf{G}\mathbf{S}_c)^{-1} \mathbf{G}\mathbf{S}_c \mathbf{w}^0 \quad (4.31)$$

which allows the influence of the semi-infinite lattice to be transferred to the dynamics of the atom in the contact of the 1D lattice. Using Eq. (4.31) to cast the terms containing $\mathbf{u}^{0,0,0}$ in terms of \mathbf{w}^0 in the equations of motion for the atom in the contact of the 1D lattice ($p=0$) relates the amplitude components at the $p=0$ and $p=-1$ lattice sites,

$$0 = \mathbf{S}_{eff} \mathbf{w}^0 + \mathbf{S}_1 \mathbf{w}^{-1}, \quad (4.32)$$

where

$$\mathbf{S}_{eff} = (\mathbf{S}_c (\mathbf{I} + \mathbf{G} \mathbf{S}_c)^{-1} \mathbf{G} \mathbf{S}_c + M_1 \omega^2 \mathbf{I} - \mathbf{S}_1 - \mathbf{S}_c), \quad \mathbf{S}_1 = \begin{bmatrix} K_1^s & & \\ & K_1^s & \\ & & K_1^a \end{bmatrix} \quad (4.33)$$

and which ultimately enables the incident phonon amplitudes to be related to the reflected amplitudes in the 1D lattice and the evaluation of the energy transmission coefficient for the contact.

Derivation of the bulk equations of motion for the 1D harmonic lattice is standard in most introductory solid-state texts [154]. Solutions to the 1D lattice dynamics yield longitudinal and transverse oscillations that are decoupled with the following two dispersion relations relating ω , q_l , and q_t for the two polarizations,

$$M_1 \omega^2 = 4K_1^a \sin^2(q_l d_1/2) \quad (4.34)$$

$$M_1 \omega^2 = 4K_1^s \sin^2(q_t d_1/2) \quad (4.35)$$

where d_l is the 1D lattice constant, and q_l and q_t are the longitudinal and transverse wavevectors. Owing to the dynamics of harmonic processes conserving ω , this dispersion relation gives the corresponding longitudinal and transverse modes in the 1D lattice that couple to the modes of frequency ω in the semi-infinite lattice.

*THERMAL RESISTANCE BETWEEN LOW-DIMENSIONAL NANOSTRUCTURES
AND SEMI-INFINITE MEDIA*

In solving Eq. (4.32), the amplitude components in the 1D lattice are the sum of contributions arising from the incident and reflected modes, and are of the form

$$\mathbf{w}^p = (\Pi_+)^p \mathbf{P} + (\Pi_-)^p \mathbf{r} \quad (4.36)$$

where

$$\begin{aligned} \Pi_+ &= \begin{bmatrix} e^{iq_t d_1} & & \\ & e^{iq_t d_1} & \\ & & e^{iq_l d_1} \end{bmatrix}, \quad \Pi_- = \begin{bmatrix} e^{-iq_t d_1} & & \\ & e^{-iq_t d_1} & \\ & & e^{-iq_l d_1} \end{bmatrix}, \quad \mathbf{P} = \begin{bmatrix} \sin(\theta) \cos(\phi) \\ \sin(\theta) \sin(\phi) \\ \cos(\theta) \end{bmatrix}, \\ \mathbf{r} &= \begin{bmatrix} r_x \\ r_y \\ r_z \end{bmatrix} \end{aligned} \quad (4.37)$$

where \mathbf{r} are the amplitude components of the reflected mode and \mathbf{P} represents the amplitude components of the incident phonon mode with unit amplitude. θ is the angle between the amplitude displacement and z axis and ϕ is the azimuthal angle with respect to the x axis. We note that the wavevectors for the longitudinal and transverse waves, q_l and q_t , are in general different for a given frequency due to the difference in lattice stiffness for motion in the different directions. Substituting Eq. (4.36) into (4.32) yields the reflected components to be

$$\mathbf{r} = -(\mathbf{S}_{eff} + \mathbf{S}_1 \Pi_+)^{-1} (\mathbf{S}_{eff} + \mathbf{S}_1 \Pi_-) \mathbf{P} \quad (4.38)$$

With these reflected mode amplitudes, we can proceed to calculate the mode transmission coefficient and junction conductance. For small difference in temperature, the thermal conductance for a polarization “ i ” across an interface is expressed as [19]

$$\sigma_i(T) = \sum_{q_i > 0} v_i^+(q_i) \Gamma_i(\omega_{q_i}) \hbar \omega_{q_i} \frac{\partial n(\omega_{q_i}, T)}{\partial T} \quad (4.39)$$

where v_i^+ is the group velocity for modes incident on the interface, $n(\omega_q, T)$ is the Bose distribution for phonon occupation number at temperature T , and $\Gamma_i(\omega_q)$ is the transmission coefficient for the “ i ” polarization. Although the calculation of Eq. (4.39) is based on the properties of the incident modes, this relation accounts for the bi-directional net interface conductance [19]. Because the energy transmission coefficient represents the difference between the incident and total reflected energy, we can express it in terms of the calculated values for the amplitudes, \mathbf{r} , of the modes reflected by the junction. Because the longitudinal and transverse projection of incident modes are linearly independent and have different dispersion relations we will calculate the transmission for these channels separately and add their contributions to find the net conductance. For incident longitudinal (\perp) and transverse (\parallel) modes, the expressions for the transmission coefficient that produce the proper energy flux when used in Eq. (4.39) are

$$\Gamma_{\perp} = 1 - |r_{z\perp}|^2 - \frac{v_t}{v_l} (|r_{x\perp}|^2 + |r_{y\perp}|^2) \quad (4.40)$$

$$\Gamma_{\parallel} = 1 - |r_{x\parallel}|^2 - |r_{y\parallel}|^2 - \frac{v_l}{v_t} |r_{z\parallel}|^2 \quad (4.41)$$

where \mathbf{r}_{\perp} and \mathbf{r}_{\parallel} are computed using $\mathbf{P}_{\perp} = (0, 0, 1)$ and $\mathbf{P}_{\parallel} = (\pi/2, 0, 0)$ in Eq. (4.38), respectively. Because of the symmetry of \mathbf{G} under the transformation $x \leftrightarrow y$, Γ_{\parallel} (polarization of in the plane of the surface of the semi-infinite lattice) is independent of ϕ . Since no modes can propagate above the mode cut-off frequency, and that the maximum frequency cut-off for transverse modes, $\omega_{max,t}$, is less than that of longitudinal modes, we set $\Gamma_{\parallel}(\omega > \omega_{max,t}) = 0$. For the same reason, $r_{x\perp}$ and $r_{y\perp}$ are zero above $\omega_{max,t}$.

4.3 Results and Discussion

We begin by considering an abrupt junction between two materials with identical bulk stiffness parameters, which will emphasize contributions to the junction impedance due to solely to geometric effects and not impedances due to material mismatch. In this analysis, for representative results, we model a “silicon-like” material where we choose bond stiffnesses parameters that yield the Lamé constants in the continuum limit of the 2D semi-infinite lattice. For the 2D semi-infinite lattice, the four bond parameters defined in Fig. 4.1 are interrelated to yield the two independent Lamé constants by the relations [137]

$$\lambda = \frac{K_2^a - 3K_2^s}{2a_2}, \quad \mu = \frac{K_2^a + K_2^s}{2a_2}, \quad 2K_d^a = K_2^a - K_2^s, \quad K_d^s = 0 \quad (4.42)$$

For comparison, we used the values of K_2^a and K_2^s derived from Eq. (4.42) for the semi-infinite FCC lattice. For silicon, we used a lattice constant of $a_2=5.4$ Å and Lamé constants of $\lambda=56$ GPa and $\mu=79$ GPa [155]. Of course, our analysis differs from that of silicon in the basis for the FCC lattice and lattice geometry for the 2D lattice, though we expect the qualitative aspects to be illustrative.

Figure 4.4 shows the transmission coefficient for longitudinal and transverse modes incident from the 1D lattice into both the 3D FCC lattice (Fig. 4.4a and 4.4b) and 2D square lattice (Fig. 4.4c and 4.4d) as a function of frequency normalized to the maximum frequency of longitudinal mode of the 1D lattice. Figures 4.4a and 4.4c show the impact of changing the relative bond stiffness ratio between the 1D and semi-infinite lattices for the 2D and 3D cases, respectively, while holding all other parameters fixed. Figure 4.4b and 4.4d show the impact of changing the relative mass ratio between the 1D and semi-infinite lattices for the 2D and 3D cases, respectively, while holding all other parameters fixed. The solid black curves are the results for identical parameters in both the 1D and semi-infinite lattices, while the blue dashed

and red dotted curves corresponds to a parameter ratio of 1.25 and 0.75, respectively. To further validate the numerical solution, we performed the calculation in limiting values of the lattice parameters, and in all cases the transmission coefficient behaved appropriately.

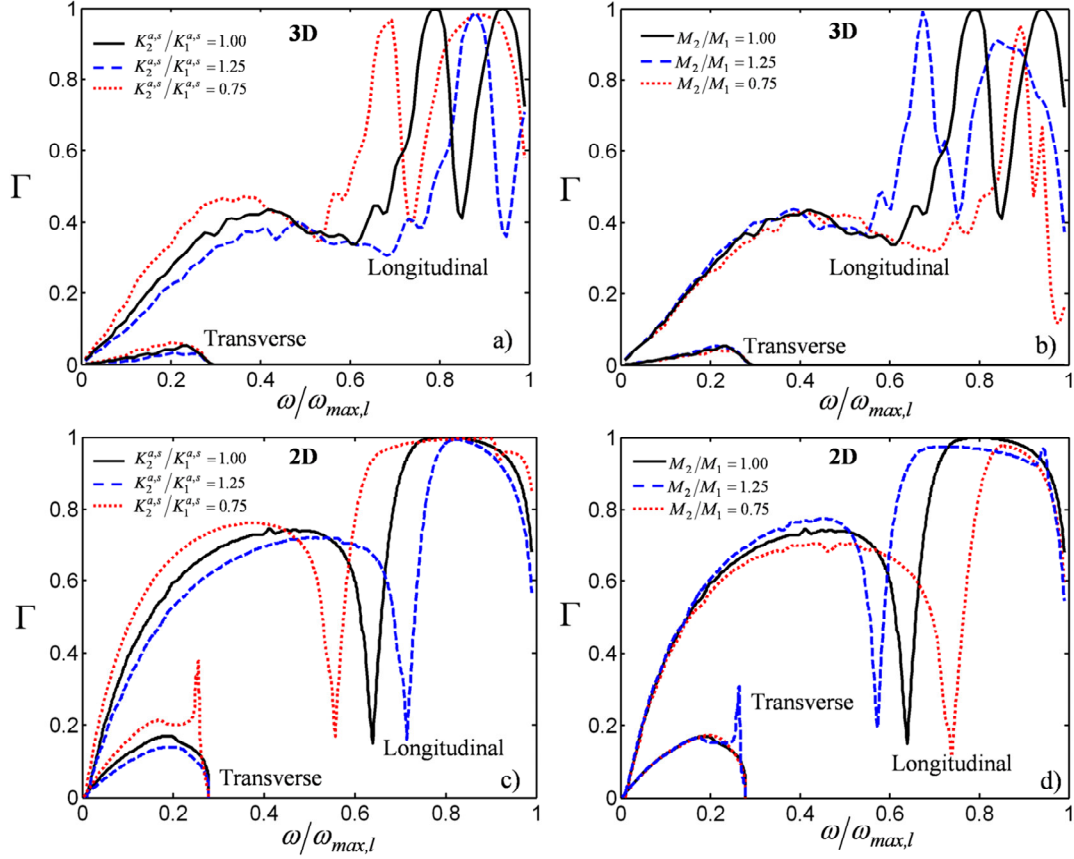


Figure 4.4: Transmission coefficient for longitudinal and transverse polarizations incident on the junction between the 1D and 3D (a, b) and 1D and 2D (c, d) lattices as a function of frequency normalized to the maximum longitudinal polarization of the 1D lattice. The solid black curves show the transmission for lattices with identical stiffness and mass parameters for a “silicon-like” material. The blue dashed curve and red dotted curve show the impact of changing the ratio of the mass or lattice stiffness parameters in the semi-infinite lattice to those in the 1D lattice to 1.25 and 0.75, respectively. For the 3D case (a) shows the effect of scaling the stiffness and (b) show the effect scaling the mass. For the 2D case, (c) shows the effect of scaling the stiffness and (d) show the effect scaling the mass. The impact of scaling mass and stiffness are qualitatively quite similar, but differ in the details of the transmission curve shapes due to their unique role in the junction boundary conditions.

The calculation shows that even for identical lattice parameters between the 1D lattice and semi-infinite lattices, the transmission coefficient is less than unity for both polarizations, which is in contrast to the perfect transmission across a junction between identical materials of similar dimensionality. The incomplete transmission across this point junction is due to a change in effective impedance that originates from the strong coupling to modes localized near the surface, which have a different effective stiffness compared to modes in either bulk domain or at the free surface alone. The unity transmission peak demonstrated by both cases indicates that the impedance for modes at these particular frequencies is well matched. That the 3D lattice shows two resonant transmission peaks whereas the 2D lattice shows only one is due to the modification in the LDOS due to the number of surface waves present in each case, which is related to the surface dimensionality and structure.

Figure 4.5 shows the evaluation of LDOS (Eq. (4.29)) for the 3D (black-solid and black-dashed) and 2D (red-solid) lattices for the case of unity parameter ratios, the corresponding transmission coefficients (black dot and black dash-dot), and the bulk density of states of the 1D lattice (red-dashed). The in-plane LDOS is given by the relation $\rho_{\parallel} = (\rho_{xx} + \rho_{yy})/2$ and out-of-plane is given by $\rho_{\perp} = \rho_{zz}$. A large relative LDOS for a particular mode indicates a relative amplitude enhancement and reduced effective stiffness for that mode. The LDOS of the 3D lattice is on average lower than that of the 2D lattice because, for identical stiffness parameters, the 3D lattice has a large number of neighbor interactions, which increases the effective stiffness of an atom in response to an external force. Comparing the LDOS and transmission in Fig. 4.5 shows that the transmission peaks and dips are related to peaks in the LDOS caused by the surface modes. The 3D lattice shows two peaks due to the two surface modes for (001) surface of a FCC lattice [151], whereas the 2D lattice has only one. The large range swept by the spectral LDOS due to the surface modes ensures an opportunity for impedance matching between the 1D and semi-infinite lattices, leading to a transmission coefficient of unity. Consequently, the number of transmission

peaks depends on the surface dimensionality and number of surface modes present. The peaks in the LDOS tend to reduce the transmission coefficient due to the large density of states mismatch between the lattices. This effect can be understood qualitatively from the fact that a large density of states mismatch is related to a large impedance mismatch due to differing effective mode stiffnesses and velocities. The form of the LDOS in Fig. 4.5 is a complicated function that deviates, particularly at high frequencies, from the free surface approximation [153] that is typically employed in calculations, and which is often approximated to scale as a power of the frequency [20, 134]. However, the linear trend in the LDOS for the 2D case and near-quadratic trend for the 3D LDOS [151, 153] observed in Fig. 4.5 at low frequencies justifies approximating the LDOS as a power of the frequency in this regime. These results indicate that accurate prediction of the energy transmission through abrupt junction requires a rigorous computation of the reservoir dynamics, particularly for the transmission of high frequency modes.

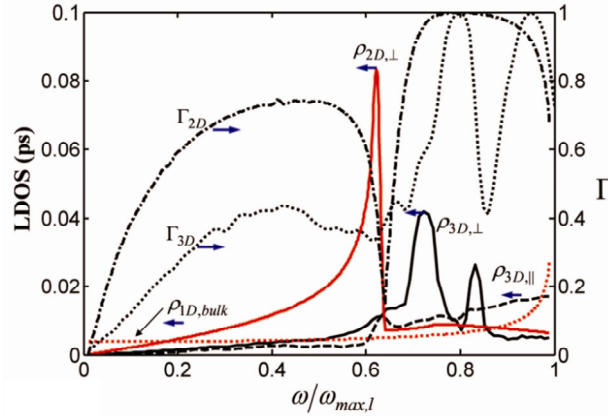


Figure 4.5: The local density of states for out-of-plane displacements ($\rho_{3D,\perp}$, black solid) for the 3D lattice, in-plane ($\rho_{3D,\parallel}$, black dashed) for the 3D lattice, and out-of-plane ($\rho_{2D,\perp}$, red solid) for the 2D lattice. Also shown is the bulk DOS for the 1D lattice ($\rho_{1D,bulk}$, red solid) and the corresponding transmission coefficients for the 3D and 2D cases. The frequency is normalized to the maximum frequency of the longitudinal mode in the 1D lattice.

THERMAL RESISTANCE BETWEEN LOW-DIMENSIONAL NANOSTRUCTURES AND SEMI-INFINITE MEDIA

The weak transmission of transverse modes for all cases and frequencies can be explained by the fact that the mode displacement fields in the semi-infinite lattices are mirror-symmetric about the z axis, whereas the incident transverse oscillations are anti-symmetric with respect the z axis. This symmetry mismatch causes weak coupling of the two modes. These results are consistent with the calculation by Buldum *et al.* [135] of energy transfer through an atomic wire contacting finite atomic reservoirs, in which transverse modes were found to be highly localized in the wire, weakly coupling to the reservoir modes.

The parameter scaling trends in Fig. 4.4 show that increasing the stiffness and decreasing the mass ratio between the 1D and semi-infinite lattices show the qualitatively similar effects of shifting the features of the transmission curves up in frequency and decreasing the average transmission coefficient, whereas reducing the ratio shows the opposite trend. The qualitatively similar behavior between increasing the stiffness and decreasing the mass is due to the fact that these parameters enter into the equations of motion for the bulk modes only through their ratio. However, variations in the mass and stiffness of the semi-infinite lattices impact the details of the transmission curves differently due to the fact that they enter differently in the boundary conditions at the lattice junctions. For both semi-infinite lattices at low frequencies, variations in the mass show little impact on the transmission, whereas at high frequencies, particularly for the 3D case, mass variations show a more dramatic change in shape of the transmission peaks. In comparing the effect of varying the stiffness ratio to that of the mass, variations in the stiffness ratio show a greater change in transmission at low frequencies and a less dramatic change in shape of the transmission peaks at higher frequencies, particularly for the 3D case. These differences in trends are related to the larger inertial contribution at higher frequencies. That the change in shape of the transmission curves are a complicated function of the stiffness and mass scaling ratios indicates that the junction transmission arising from material property mismatches are intertwined with the impedance contributions due to geometric effects, and do not simply separate into two individual contributions.

The total thermal conductance, including contributions from longitudinal and transverse modes, for an abrupt junction for the 1D to 2D and 3D cases are shown in Fig. 4.6. Figure 4.6a shows the impact of variations in the stiffness ratio on the conductance, while Fig. 4.6b shows the impact of variations in the mass ratio. The calculations show that the contribution to the thermal resistance due solely to the geometric effects (solid black curves) is comparable to acoustic mismatch effects at interfaces between materials with similar dimensions. The conductance of the junction with the 3D lattice is less than that with the 2D lattice because of the lower average transmission coefficient resulting from the larger effective stiffness of the 3D lattice. Converting the conductance of 130 pWK^{-1} for the 2D case and 72 pWK^{-1} for the 3D case at 300 K to a thermal resistance using the circular cross sectional area of the 1D lattice with a diameter of the lattice spacing, i.e. $A_c = \pi(d_l/2)^2$, gives a thermal resistance of $1.8 \text{ m}^2\text{K/GW}$ (2D) and $3.3 \text{ m}^2\text{K/GW}$ (3D), which is comparable to typical contributions from an acoustic impedance mismatch. From Fig. 4.4, the transmission coefficient is nearly linear in ω at low frequencies for both the 2D case and the 3D case, but shows more quadratic like behavior for the 3D case, which is expected given the stronger quadratic nature of the LDOS for the 3D case. The strong linear component in the transmission coefficient at low frequencies for the 3D case compared to the pure quadratic predictions of the continuum theory [31] are most likely due to the stretching of the LDOS due to the rather stiff bond stiffness parameters used in this work. The near-linear behavior of the transmission coefficient yields a low temperature conductance should scale as $\sim T^2$, as is seen in the low temperature limit of Fig. 4.6. The results do not show any crossing of the conductance trends over the full temperature range.

THERMAL RESISTANCE BETWEEN LOW-DIMENSIONAL NANOSTRUCTURES AND SEMI-INFINITE MEDIA

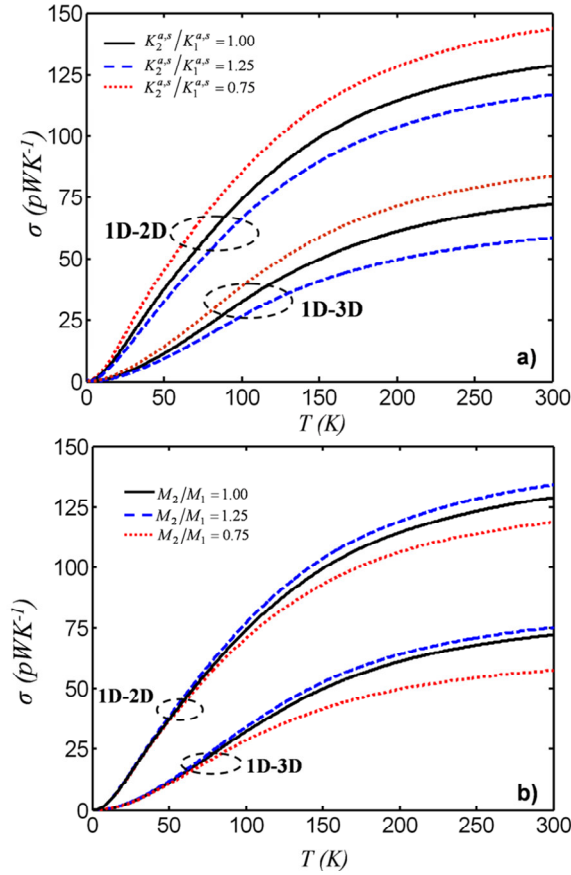


Figure 4.6: Total thermal conductance as a function of temperature for a junction for both the 3D and 2D cases. (a) shows the impact of varying the stiffness scaling of the semi-infinite lattices or the junction conductance, and (b) shows the impact of varying the mass on the junction conductance. The solid black curves show the transmission for lattices with identical stiffness and mass parameters. The blue dashed curve and red dotted curve show the impact of changing the ratio of the mass or lattice stiffness parameters in the semi-infinite lattice to those in the 1D lattice to 1.25 and 0.75, respectively. The results show that there is a finite conductance of comparable magnitude to the acoustic mismatch conductance even for materials of identical stiffness parameters.

In the case of an abrupt junction, the largest junction thermal conductance does not occur with materials of similar bulk impedances, as is the case with conventional interfaces between materials of similar dimensionality, but with a semi-infinite lattice that has a stiffness less than or a mass greater than the 1D lattice. Figure 4.7 shows the junction conductance as a function of the stiffness and mass scaling ratio between

the 1D lattice and 3D lattice for 300 K and 30 K. For each data set, either the stiffness or mass ratio is varied while all other parameters are held fixed. For 300 K, the results show that the maximum thermal conductance of the junction occurs with a stiffness ratio of ~ 0.5 and a mass ratio of ~ 1.5 . At 30 K, the data do not show a maximum conductance, which is due to only the low frequency phonon modes being populated and the monotonic dependence of the transmission coefficient on the stiffness and mass at low frequencies. These results suggest the thermal conductance of nanostructured thermal interfaces may in general be best optimized by engineering a junction with a reservoir material that has a bulk impedance which is lower than that of the nanostructure, rather than materials that have similar intrinsic impedances.

While this lattice dynamics calculation focuses on the relatively simple model problem of a 1D atomic chain in contact with 2D and 3D semi-infinite lattices, it enables qualitative arguments about the practical phonon transmission effects on contact resistances that will be found in actual nanostructure geometries. For the interface between a graphene nanosheet and 3D semi-infinite medium, the phonon transmission would be complicated by non-orthogonal lattice geometry in the graphene layer and phonon modes with angular incidence, which each have displacement components in and out of the plane of the interface. We expect that the results of the calculation for the 1D to 2D case would give reasonable predictions for the transmission of longitudinal modes in the graphene sheet with normal incidence. We expect the transmission of normal incidence in-plane and out-of-plane transverse modes to couple weakly to a semi-infinite medium, for reasons similar to those for the weak coupling of transverse modes of the 1D-2D junction. For modes with angular incidence, the energy transmission would be dominated by the transmission of the longitudinal projection of the displacement field, and thus the conductance should scale as $\sim \cos^2(\theta)$, where θ is the angle between the polarization vector and the z axis.

*THERMAL RESISTANCE BETWEEN LOW-DIMENSIONAL NANOSTRUCTURES
AND SEMI-INFINITE MEDIA*

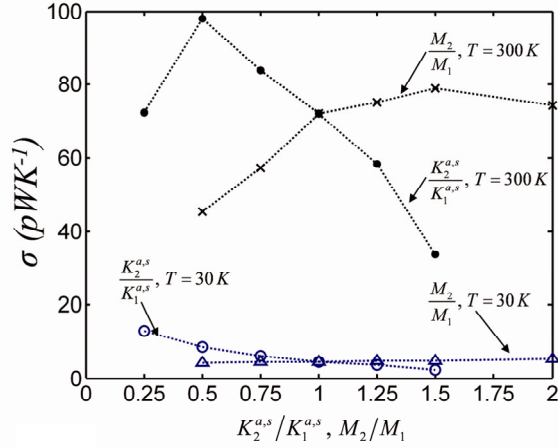


Figure 4.7: The junction conductance as a function of stiffness ratios between the semi-infinite and 1D lattice at 300 K (black solid circles) and 30 K (blue open circles) and mass ratios between the semi-infinite and 1D lattice at 300 K (black x) and 30 K (blue triangle). For each data set, the noted ratio is varied while all other parameters are held fixed. The results show that there is a maximum conductance for a stiffness ratio of ~ 0.5 and mass ratio of ~ 1.5 . The conductances at 30 K do not show a maximum conductance.

For phonon modes with quadratic dispersion, such as flexure modes in nanotubes [41], nanowires, and elastic bridges [139], the amplitude displacement is predominantly parallel to the free interface for the 3D case and for the in-plane mode in the 2D case. Since the quadratic nature of the dispersion relation for these modes is unrelated to the fundamental symmetry basis for the weak coupling of the transverse displacement fields, it has little impact on the transmission since the dispersion relation only enters into the transmission calculation through $q_t(\omega)$ in Eq. (4.37) for the 1D to 3D and 1D to in-plane-polarized 2D cases. Though these modes are not present in the 1D lattice model used in this analysis, and their detailed calculation is beyond the scope of this work, we investigated the impact of a quadratic dispersion with a simple approximation that modifies the dispersion relation used in Eq. (4.37) from Eq. (4.35) to

$$q_t = \frac{\pi}{a_1} \sqrt{\frac{\omega}{\omega_{max,t}}} \quad (4.43)$$

This substitution slightly sharpens the peak in the transverse transmission curve in Fig. 4.4, with insignificant impact on longitudinal modes, increase in net transmission, and overall impact. Since it is a less common geometry, the transmission of out-of-plane flexure modes for the 1D-2D case was not considered in this analysis. However, we expect that these flexure modes would couple to the out-of-plane modes with quadratic dispersion in the 2D domain, and that due to similar symmetry arguments, the transmission would behave much like the longitudinal branch with a different effective stiffness.

For the contact between a carbon nanotube and semi-infinite 3D media, we believe that the 1D-3D case is a representative model that suggests that the longitudinal mode will dominate the transmission, while the transverse and torsion modes will have negligible transmission due the large amplitude component in the plane of the interface. The specific form of the phonon transmission function, particularly at high frequencies, would require detailed calculation and be sensitive to the specific interface bonding geometry, including bonding of the nanostructure to multiple atoms on the surface. For materials with polyatomic cross-sectional structure such as multi-walled carbon nanotubes or silicon nanopillars, we expect that as the cross-sectional area increases, the impedance mismatch effects arising from geometry will decrease and the transmission of modes with wavelength less than the characteristic cross-section dimension will increase due to stronger coupling to bulk-like modes.

Because dimensionally mismatched interfaces are becoming more prevalent in nanostructured technology, their impact on thermal transport investigated by this work strongly motivates the need to consider more detailed calculations considering dimensional mismatched effects.

4.4 Conclusions

This work uses a lattice dynamics approach to investigate the transmission of energy across an abrupt junction between a harmonic 1D and 3D FCC lattice and between a 1D and 2D square lattice with second nearest neighbor interactions. Although this is a relatively simple geometry compared to many of the practical problems in nanostructures, it provides a simple approximation to nanoscale point contacts and can be viewed as an approximation relevant to nanotube-like structures. The results show that energy strongly couples to modes localized near the surface of the semi-infinite lattice and that the energy transmission coefficient across the interface is less than unity even for identical bulk properties in both domains. The calculation shows that the transmission coefficient for the transverse incident modes is very low at all frequencies due to symmetry effects. The abrupt change in geometry of the junction presents a thermal resistance contribution that is comparable to that of a mismatch in material impedance. The results suggest that energy transmission through nanoscale thermal interfaces may be enhanced by intentionally using materials with intrinsic impedance mismatches. The lattice dynamics calculations performed here provide an initial perspective on the impact of localized phonon modes on the acoustic mismatch resistance and lay the groundwork for more detailed studies involving 3D molecular dynamics.

Chapter 5

Thermal Properties of Ultra-thin Hafnium Oxide Gate Dielectric Films

5.1 Introduction

As HfO_2 is currently replacing SiO_2 as the gate dielectric of choice below the 45 nm node [156, 157], its thermal properties are of increasing importance since the thermal conductivity and thermal interface resistance can significantly influence the phonon temperature during device switching and indirectly affect device performance and reliability [1, 158]. However, to date, most research has focused almost exclusively on the electrical [159, 160] and chemical interface [161, 162] properties of HfO_2 . While previous 3ω measurements of the thermal conductivity of thick (> 500 nm) microcrystalline HfO_2 films report a room temperature value of $1.2 \text{ Wm}^{-1}\text{K}^{-1}$ [163], recent scanning thermal microscopy measurements (SThM) of 3 nm thick a- HfO_2 films report a significantly lower value in the range 0.27—0.49 $\text{Wm}^{-1}\text{K}^{-1}$ [164]. This strong reduction in conductivity for thin amorphous films can be due to a variety of effects including contributions from interfaces and variations in volumetric and interface microstructure on thermal conduction. In this letter, we report the intrinsic thermal conductivity and interface resistance of 200 Å, 118 Å, and 56 Å thick HfO_2 films grown on Si substrates measured over the temperature range 300-500 K using pump-probe time-domain thermoreflectance thermometry (TDTR).

5.2 Sample Fabrication and Experimental Setup

The samples were prepared by cleaning prime Si (100) wafers (1-10 Ωcm) by the RCA method [165], followed by immediate oxidation for 45 s in a slot-plane-antenna plasma processing chamber at 500°C and 4 kW microwave power in a 5 Torr ambient with O₂ flow rate of 400 sccm and Ar flow rate of 1200 sccm. The thickness of the plasma SiO₂ was measured to be 1.7 nm by ellipsometry. Different thicknesses of HfO₂ were subsequently deposited onto the samples by controlling the number of cycles in the atomic-layer-deposition (ALD) method, described elsewhere [166], at 250°C with tetrakisdeethylamino hafnium (TDMAHf) as the precursor and water as the oxidant. Following the HfO₂ ALD, 30 nm of Al was deposited by e-beam evaporation without substrate heating. Finally, the samples were annealed in forming gas (95% N₂, 5% H₂) at 400°C for 30 minutes.

Transmission Electron Microscopy (TEM) imaging and Selective Area Electron Diffraction (SAED) analysis of the samples after metallization and annealing reveal that the a-HfO₂ films contain increasing volume fractions of tetragonal (t-HfO₂) nanocrystals with increasing film thickness. Fig. 5.1a is a representative sample cross section of the 200 Å thick HfO₂ showing embedded nano-scale t-HfO₂ grains. The plan-view TEM images of the 200 Å and 118 Å in Fig. 5.1 (b), (c) demonstrate an increase in crystallite volume fraction with film thickness. Table 5.1 summarizes the TEM measurements of the film thicknesses and composition, including crystalline volume fractions estimations extracted from large field-of-view TEM images (not shown). Comparison of cross sectional TEMs of regions with and without aluminum suggest that oxygen is transferred from the underlying layers to form an amorphous AlO_x interfacial layer at the HfO₂/Al interface during the anneal process, likely from residual oxidant species present in the as-grown ALD-HfO₂ [167], and for thinner HfO₂ layers, from the SiO₂ interlayer via a previously reported oxygen gettering phenomenon [168].

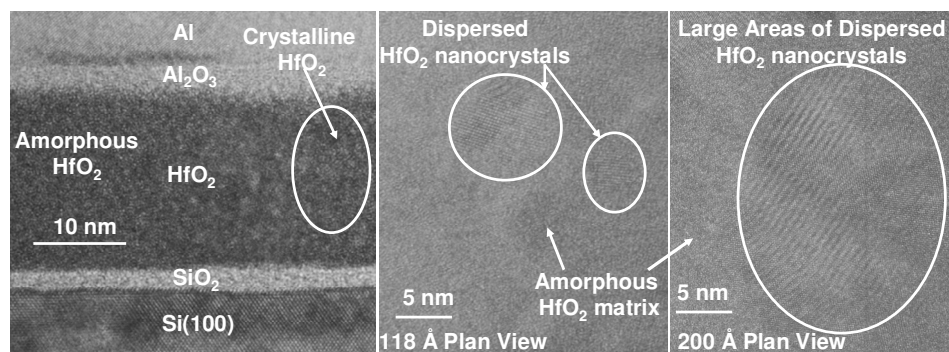


Figure 5.1: a) Representative cross-sectional TEM of 200 Å thick sample showing HfO₂ nanocrystals embedded in an amorphous HfO₂ matrix. b) Plan view of the 118 Å sample showing a low density of HfO₂ nanoparticles in an amorphous matrix. c) Plan view of the 200 Å sample showing a high density of HfO₂ crystallites in an amorphous matrix.

Picosecond TDTR is an established technique for measuring the thermal conductivity and interface resistances in thin films, thoroughly described in the literature [116, 121, 122]. In brief, periodic picosecond pump pulses (9.2 ps pulse width, 82 MHz repetition rate, ~350 pJ/pulse energy, 1064 nm wavelength) from a mode-locked Nd:YVO₄ laser deposit heat in the metal film, establishing a transient temperature field within the sample. The surface temperature of the metal is then measured by an optically delayed probe beam, derived from the pump, which is reflected off of the sample and collected by a fast photodetector. The pump beam is externally modulated at 8 MHz for lock-in detection and converted to 532 nm with a second harmonic generator to enable rejection of pump leakage at the detector. The co-aligned pump and probe beams are focused on the sample surface with Gaussian waist diameters of 10.0 μm and 5.0 μm and powers of 20 mW and 5 mW, respectively. The temperature excursion (<10 K) due to the laser heating is significantly less than the HfO₂ deposition temperature.

The thermal conductivity and buried interface resistances are extracted by fitting the data to the solution of the radial-symmetric three dimensional heat diffusion equation for the multi-layer stack with surface heating by a modulated periodic pulse train [121, 122]. The measurement system and thermal model were validated by confirming a

THERMAL PROPERTIES OF ULTRA-THIN HAFNIUM OXIDE GATE DIELECTRIC FILMS

measured value of $1.4 \text{ Wm}^{-1}\text{K}^{-1}$ for the thermal conductivity of a 102 nm thick thermally grown SiO_2 film coated with a 38 nm thick Al film. The unique temporal dependence of the thermal response sensitivity on the spatial distribution of thermal properties permits their isolation [122, 169]. We fit the data with two parameters: the HfO_2 thermal conductivity, k_{HfO_2} , and the total HfO_2 - SiO_2 -Si boundary resistance, R_b . In fitting k_{HfO_2} and R_b , we set the HfO_2 -Al interface resistance to zero as the data bounds the value to below $3 \text{ m}^2\text{K/GW}$, below which data extraction is insensitive to its value. The HfO_2 heat capacity and other required thermal properties were taken from the literature [123].

Table 5.1: Structure, composition, and thermal properties of HfO_2 sample films.

HfO_2 Thickness (Å) (± 10)	Al Thickness (Å) (± 20)	SiO_2 Thickness (Å)	a- Al_2O_3 Thickness (Å)	Crystal Fraction in a- HfO_2	Effective (intrinsic) Film Thermal Conductivity at 400 K from (1). ($\text{Wm}^{-1}\text{K}^{-1}$)
200	390	15	18	20-30 %	0.68 (0.80)
118	330	15	16	5-10 %	0.54 (1.14)
56	410	Absent	14	Absent	0.42 (0.58)

5.3 Results and Discussion

Fig. 5.2 shows intrinsic k_{HfO_2} and R_b temperature dependence, with the volumetric SiO_2 resistance subtracted, assuming $1.4 \text{ W/(m}\cdot\text{K)}$ for the SiO_2 thermal conductivity. The uncertainty bars in Fig. 5.2 include the effects of the film thickness uncertainty in Table 1, the contribution of the Al_2O_3 layer and HfO_2 -Al interface, and the uncertainty related to the ability of the measurement to uniquely resolve the interface and volumetric resistances. The latter is the dominant uncertainty in the 56 Å film data. Fitting this data with a single effective conductivity parameter provides the

conductivity uncertainty lower bound. The thermal conductivities of the 118 and 56 Å samples both exhibit slight increases with temperature, a characteristic of amorphous dielectrics consistent with previous measurements [163]. The weaker temperature dependence of the thermal conductivity of the 200 Å sample is most likely due to the offsetting temperature trends for volumetric resistance contributions of the amorphous and crystalline components. The k_{HfO_2} data fall between the theoretical estimations from the minimum thermal conductivity model [170], k_{min} , of HfO₂ (Fig. 5.2a) when evaluated using either the atomic or the molecular number density in combination with the known HfO₂ acoustic velocities [171]. The application of these number density definitions is related to the relevant fundamental vibration unit, which is not entirely understood for amorphous materials [172].

THERMAL PROPERTIES OF ULTRA-THIN HAFNIUM OXIDE GATE DIELECTRIC FILMS

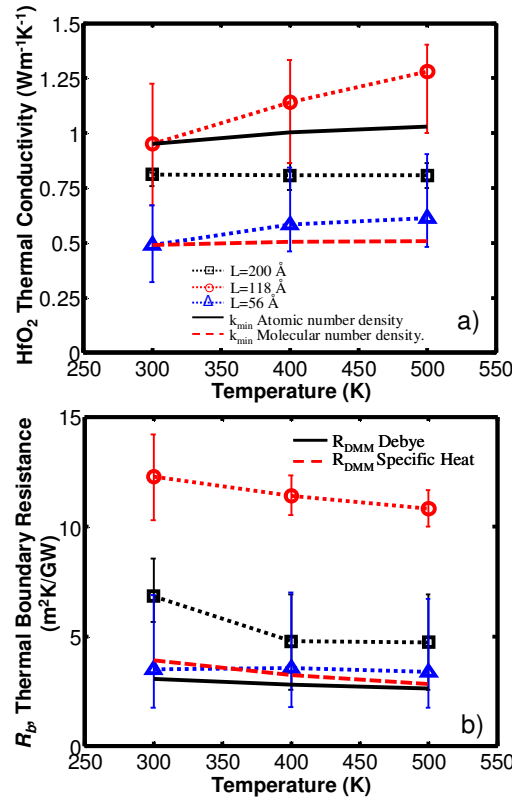


Figure 5.2: a) Intrinsic HfO₂ thermal conductivity for 200 Å (black square), 118 Å (red circle), and 56 Å (blue triangle) as a function of temperature. Predictions for the minimum thermal conductivity theory calculate using the atomic number density (solid black) are molecular density (black dashed) . b) Total thermal resistance for the HfO₂-SiO₂-Si interface, and DMM predictions in the Debye approximation (solid black) [22, 24] and using the specific heat correction to the density of states (red dashed) [24] .

Due to its upper bound of 3 m²K/GW, the possible residual HfO₂-Al interface resistance cannot explain the reduction in intrinsic thermal conductivity for the 200 Å film compared to the 118 Å film. This trend may be due to the increased HfO₂ nanocrystal volume fraction in the 200 Å film creating additional interface resistances, which can be larger (~10 m²K/GW) than the reduction in resistance due to the substitution of the crystalline phase. Previous work reported nanolaminates thermal conductivities [173] below the minimum due to the presence of interfaces, and similar reductions in the In_{0.53}Ga_{0.47}As thermal conductivity with increasing ErAs nanoparticle concentration due to the scattering of mid-to-long-wavelength phonons [174]. This

similar reduction in conductivity due to the scattering of mid-to-long-wavelength phonons suggesting the importance of long wavelength phonons (below ~ 3 meV) [172, 174] in the thermal conduction in a-HfO₂ films.

Because R_b and the volumetric resistance (L/k_{HfO_2}) are comparable in value, the effective thermal conductivity of the layer will exhibit a thickness dependence according to

$$k_{\text{eff}} = \frac{k_{\text{HfO}_2}}{1 + R_b k_{\text{HfO}_2} / L_{\text{HfO}_2}}, \quad (5.1)$$

presented in Table 1 for a typical device operating temperature of 400 K. Including R_b in k_{eff} yields values closer to previously measured thin-film values [164].

Currently, there are no rigorous models accurately predicting thermal interface resistances at high temperature (>20 K) [22]; however, the diffuse mismatch model (DMM) is a simplified approach that assumes phonons are diffusely scattered at an interface, an approximation most relevant at room temperature [22, 24]. The reasonable predictions of the DMM model suggest that the interfaces are high-quality and that long wavelength phonons may be important in heat conduction. The relative values of the interface resistances for the three films are most likely due to the variations in interface quality observed in the TEMs, with the lowest interface resistance for the 56 Å film, which is the most diffuse.

5.4 Conclusion

The intrinsic HfO₂ thermal conductivity depends on the film thickness and post-deposition processing, deviating from both bulk values and measurements of effective film thermal conductivities. Consequently, modifications in gate dielectric microstructure due to post-deposition thermal processing can impact device

*THERMAL PROPERTIES OF ULTRA-THIN HAFNIUM OXIDE GATE DIELECTRIC
FILMS*

temperatures through unexpected changes in the thickness dependent film thermal conductivity.

Chapter 6

Conclusion

This section summarizes the work and results of this dissertation and provides some suggestions and discussion of future work.

6.1 Summary

This dissertation focuses on characterizing and understanding the physics and thermal properties of nanostructure materials, with particular emphasis on understanding the impact of thermal interfaces in aligned arrays of carbon nanotubes and ultra-thin hafnium oxide films. This dissertation provides several main contributions to the field.

First, this work measures the composition and temperature dependence of the interface resistance and effective heat capacity of metal-coated aligned CNT films, and develops the following understanding of conduction within these films. While aligned films of CNTs can be relatively uniform on the macroscale, the variations in roughness and porosity at the nanoscale can cause partial engagement of the CNTs when the film interfaces with substrates such as a deposited metal film or pressed mechanic contact. The partial engagement reduces the effective volume fraction of CNTs participating in heat transfer, which amplifies the nanoscale interface and volume resistances. For films below $50\text{ }\mu\text{m}$, the nanoscale interface resistances dominate over the volumetric contribution for high quality CNTs.

This understanding of conduction was developed by characterizing the properties of CNT films through a novel extension of the nanosecond thermorefectance technique

CONCLUSION

that uniquely extracts the effective heat capacity and interface resistances of the films. This technique yields a measurement of the effective volume fraction of CNTs participating in conduction. Prior work on aligned MWNT films found resistances significantly higher than would be expected from simply scaling the CNT conductivity by the volume fraction [62, 88]. This work finds a similar total thermal resistance of SWNT films, falling in the range of $R''_{eff,tot} = 12-60 \text{ m}^2\text{KW}^{-1}$. However, directly measuring the interface resistances using the nanosecond thermoreflectance technique revealed that the interfaces are often the dominant source of the thermal resistance in CNT films. The reduced effective heat capacity data for the films as well as the correlation between the interface resistance and effective CNT heat capacities suggest that partial nanotube engagement (<1% vol engagement for films with 3-12% vol nominal density) is the origin of these large interface resistances in CNT films. This conclusion is supported by images of the metal film, the CNT surface topography, and CNT-metal contact.

This work develops a model for conduction within the film at the nanoscale, which allows for the extraction of individual SWNT-interface contact resistances, yielding values in the range of $10-50 \text{ m}^2\text{KW}^{-1}$. These results are approximately an order of magnitude larger than theoretical predictions based on a modification of the AMM TBR model for CNT structures developed in this work. The temperature dependence of the individual SWNT-metal interface suggests that inelastic scattering may be important in phonon conduction at nanotube interfaces. The low values of the extracted individual SWNT-interface resistances along with the dependence of the resistance and engagement on metallization suggest that improving the engagement by engineering the interfaces offers the potential to reduce the resistances of CNT films below $1 \text{ m}^2\text{KW}^{-1}$. This work explored improving this interface resistance by combining MWNT films with indium solder, discovering a reduction in the total resistance to $7 \text{ m}^2\text{KW}^{-1}$. This reduction in total resistance was achieved at film thickness promising for a reliable thermo-mechanical bond. ($150 \mu\text{m}$). However future work is necessary to further improve the thermal performance of these films.

A second contribution of this work is the direct characterization of the thermal boundary resistance of the CNT film growth interface by developing and using a through-substrate multi-frequency picosecond time domain thermoreflectance technique. Measurements of the growth interface resistances are advantageous since the CNTs are fully engaged with the substrate. However, directly measuring this interface is complicated by the need to obtain optical access to a metal-coated buried interface. In this work, MWNTs are grown on metal-coated transparent substrates and picosecond TDTR data taken at multiple modulation frequencies measures the effective MWNT-substrate interface resistance and CNT volume fraction, yielding values of 150-280 m^2KW^{-1} (for local a temperature of ~ 800 K) and 0.01-0.019%, respectively. These resistance values, measured using a heat flux established from the base of the CNTs, are lower than those for the CNT-substrate interface resistances measured for SWNT films, where the heat flux was established through the CNT film from the top. This variability is most likely due to differences in the effective engagement factor described previously. The data yield a resistance of 1-1.5 m^2KW^{-1} for an individual CNT-substrate contact, which is in reasonable agreement with theoretical predictions. Thus, further study of such interfaces offers an approach to studying fundamental phonon transport across low dimensional interfaces.

A third contribution of this work is the development of a theoretical model for phonon conduction between low dimensional materials and semi-infinite media such as CNTs, molecular junctions, and other nanostructures. Most previous work has focused on the understanding of phonon conduction through interfaces between three dimensional materials, while relatively little work [31-33] has focused on developing models relevant for low dimensional interfaces. In nanostructures and low dimensional interfaces, the localization of phonons in directions parallel to the interface may strongly influence the effective thermal resistance through modifying the modes that participate in heat transfer.

CONCLUSION

The present work investigates model problems of abrupt junctions between a harmonic 1D and a 3D FCC lattice and between a 1D and a 2D square lattice using a Green's function lattice dynamics approach. For the 1D-3D and the 1D-2D cases, the thermal resistances arising from the dimensional mismatch effects for Si-like materials are 3.3 and 1.8 $\text{m}^2\text{K/W}$, which are comparable to resistance values arising from acoustic mismatch at the interfaces of bulk media. The resistances of the dimensionally mismatched interfaces are in reasonable agreement with the individual CNT-substrate interface resistances measured in this work. The localization of modes near the surface of the semi-infinite lattice modifies the effective impedance of the phonon modes in the semi-infinite lattice, yielding a sub-unity interface phonon transmission coefficient even for identical bond stiffnesses in both domains. For the 1D-3D interface, the results suggest that its transmittance may be enhanced by using materials with a mismatch in bulk impedances. The lattice dynamics calculations are used to develop qualitative arguments for the interface resistances in practical geometries involving carbon nanotubes, silicon nanopillars, and graphene.

A fourth contribution of this work is the application of the TDTR metrology to study the thermal conductivity and interface resistance of ultra-thin HfO_2 films, which incorporate nanoparticle features. Although the thermal properties of HfO_2 are of increasing importance as it is currently replacing SiO_2 as the gate dielectric of choice below the 45 nm node [1, 156-158], there are little data for their value. This work measures the intrinsic thermal conductivity and interface resistance of 200 Å, 118 Å, and 56 Å thick HfO_2 films grown on Si substrates measured over the temperature range 300-500 K. The data yield room temperature intrinsic thermal conductivity values between 0.49-0.95 $\text{Wm}^{-1}\text{K}^{-1}$ and interface resistances of 5-12 $\text{m}^2\text{KGW}^{-1}$, which agree reasonable well with theoretical predictions based on DMM TBR calculations. The intrinsic HfO_2 thermal conductivity depends on the film thickness and post-deposition processing, deviating from both bulk values and measurements of effective film thermal conductivities. The presence of nanocrystals in the a- HfO_2 matrix reduces its conductivity, suggesting that the scattering of long wavelength phonons is

important for conduction amorphous films. Consequently, modifications in gate dielectric microstructure due to post-deposition thermal processing can impact device temperatures through unexpected changes in the thickness-dependent film thermal conductivity.

6.2 Discussion and Suggestions for Future Work

6.2.1 Thermal Properties of CNT Interface Materials

Given that the thermal resistances in CNT films are dominated by interfaces, and thermal conduction within CNT films is often dominated by inter-tube contact resistance [103], the effective thermal conductivity of CNT films and the conductivity of individual nanotubes within bulk films is difficult to measure and remains an open question requiring further research. The literature reports a wide range for the conductivity of individual nanotubes, with values falling between $200\text{-}10000\text{ Wm}^{-1}\text{K}^{-1}$ [100], but it is unclear that such values are realized in bulk CNT materials. Some recent works suggest that the conductivity of individual CNT in bulk materials may be significantly lower, on the order of $\sim 30\text{-}50\text{ Wm}^{-1}\text{K}^{-1}$ [175, 176]. Such reductions in individual CNT conductivity may be due to an increased defect density or increased scattering due to CNT-CNT contact. In addition to extending some of the techniques in this work to increasing their sensitivity to measuring the conductivity of CNTs, micro Raman thermometry is a promising approach for measuring local thermal conductivities in CNT films [102, 177]. This technique can provide local thermal conductivities through measuring the absolute temperature rise with micron spatial resolution due to optical self-heating. Open questions for the conductivity of CNT films include 1) the impact of the CNT density (as-grown and artificially densified) on the thermal conductivity since the competing effects of increased phonon scattering and conduction pathways due to increased inter-tube contact are ambiguous, 2) the

CONCLUSION

impact on the thermal conductivity of individual tubes on imbedding CNTs in a matrix material.

The majority of the thermal property data that is currently available for CNT films is a compilation of measurements from different researchers for samples with different geometries, growth processes, compositions, and interface structures. Such variations challenge achieving a comprehensive understanding of and models for conduction in CNT materials. Future research needs to develop comprehensive measurements that carefully study the impact of variation in film properties (e.g. CNT length, density, quality, etc.) on the film thermal conductivity and interface resistances. Such data will supplement the needed modeling efforts in such directions, and some modeling efforts are heading that way [103, 178].

While the reduction in resistances in CNT arrays by the inclusion of indium demonstrated in this work and by Tong *et al.* [69] is promising, such reductions have currently been realized under laboratory conditions, and are difficult to reproduce. Optimizing the interface metallization, ensuring its reliability, and developing a practical fabrication and implementation approach are essential for developing high performance TIM interfaces. Particularly challenging is current scarcity of data for the impact of thermal cycling on CNT film properties. Extending such developments to broader applications such as thermoelectrics is particularly challenging due to the requirements of a more severe thermal environment.

Understand the temperature scaling of the CNT growth interface TBR by extending the through-substrate measurements developed in this work to low temperatures can provide insight into fundamental phonon conduction physics in low dimensional mesoscopic systems. Practically, such measurement requires the development of a process to grow CNTs on high conductivity transparent substrates with thermal buffer layers. Since the CNT engagement is interface dependent, bi-directional measurement

of the effective heat capacity of such film may provide insight into the nanotube engagement and thermal coupling within the array.

6.2.2 Mechanical Properties of CNT Films

While the potential for CNT based TIMs has generated much recent research efforts which have improved our understanding of their thermal properties [48, 69, 89, 95, 179], there are little data for their mechanical properties such as elastic modulus and shear stiffness. The mechanical properties are critical in determining the maximum shear stress experience by a TIM due to thermal expansion mismatch, which affect the reliability of the TIM. The impact of the mechanical properties are particularly acute for thermoelectric applications, where the TIMs have much larger bond line thicknesses and are subjected to much larger temperature gradients compared to microprocessor applications [180]. What little data there are for the mechanical properties of aligned CNT arrays has focused almost entirely on the axial elastic modulus, with no data for the lateral elastic modulus [181, 182], which is the more relevant parameter. These data for the vertical elastic modulus yield values around ~ 10 MPa [182, 183], which is comparable to that of a polymer and suggest that the lateral modulus is also low. Future work is needed to characterize and understand the mechanical properties of aligned CNT film and their dependence on the physical properties of the film (e.g. CNT density, CNT length, etc.).

Traditional methods for measuring the modulus of thin films such as nanoindentation are challenging to apply to measuring the lateral elastic modulus of CNT films due to the challenges in physically accessing the CNT cross-section and the deflection of the CNTs caused by the indenter tip. One approach to measure the lateral elastic modulus is to grow CNTs on microresonators and measure the shift in resonant frequency due to the presence of the CNTs. For resonator bending modes, this shift is most strongly determined by the CNT lateral elastic modulus and mass density. Fig. 6.1 illustrate the growth of CNTs on a MEMS microresonator along with

CONCLUSION

a cross-sectional SEM of a fabricated resonator structure. Laser Doppler velocimetry provides a non-contact approach to measuring the resonant frequency of the structures. Data for different resonator geometries can provide the elastic modulus and density of the CNT films independently, which are quite difficult to measure accurately with other techniques. Resonator Q-factor damping data for the CNT films can potentially provide information into the CNT conduction and thermo-mechanical interaction mechanisms in the arrays. Such structures also allow for the measurement of the thermal properties of the film using the optical techniques developed in this work.

The ultimate goal of this work would be to provide comprehensive thermo-mechanical data for CNT films and understand the physical parameters that dictate these properties. A key goal is to find optimal combinations of film properties that minimize the thermal resistance while paying little penalty in elastic modulus.

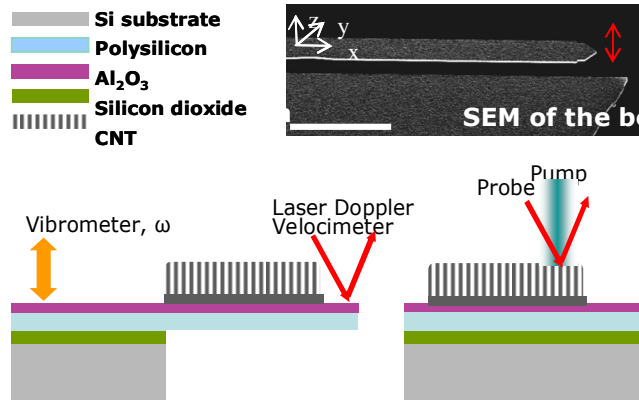


Figure 6.1: Schematic of CNT grown on a microresonator and example cross section of a fabricated micro resonator for measuring the lateral elastic modulus and density of CNT films. The resonant frequency can be measured through using laser Doppler velocimetry and the thermal properties can be measured through the optical techniques developed in this work.

6.2.3 Engineering and Fundamental Physics of Interface Resistances in Nanostructures

Thermal modeling of phonon conduction through mesoscopic interfaces is still a developing field. The strong relation between the LDOS of the surface and the phonon transmission suggests the possibility that engineering the phonon spectra may be able to reduce the interface resistance for particular phonon modes, if not the total resistance, for nanostructures in contact with thermal reservoirs. Such an advancement would be particularly useful for reducing the effective interface resistance in applications with single molecule devices since energy is often scattered into specific vibration modes of the molecule. Currently, efforts developing the non-equilibrium Green's function approach are promising for incorporating more realistic effects such as anharmonic effects [20], realistic nanostructures, and realistic surface structures and interface bonding (which strongly affect the spectral structure of the LDOS). Pseudo-empirical approaches that use measured data for the surface DOS to calculate the transmission coefficient as substitute for calculating the Green's function, combined with the more simple calculations to yield the conduction, may provide a more practical approach to estimating the interface conductance.

More data are needed for phonon conduction through dimensionally mismatch interfaces to benchmark and validate conduction models. Promising approaches to provide such data include measuring a large number of individual identical molecular interfaces in parallel such as in self assembled molecule layers [184] and CNT films (c.f. section 2.3), or directly measuring individual nanostructure interfaces using nanomanipulation techniques such as suspending individual molecules between an AFM tip and a substrate surface [185].

Bibliography

- [1] E. Pop and K. E. Goodson, "Thermal Phenomena in Nanoscale Transistors," *J. Electronic Packaging*, vol. 128, pp. 102-108, 2006.
- [2] E. Pop, K. Banerjee, P. Sverdrup, R. Dutton, and K. Goodson, "Localized heating effects and scaling of sub-0.18 micron CMOS devices," in *Electron Devices Meeting, 2001. IEDM Technical Digest. International*, 2001, pp. 31.1.1-31.1.4.
- [3] A. Faraon and J. Vučkovic, "Local temperature control of photonic crystal devices via micron-scale electrical heaters," *Appl. Phys. Lett.*, vol. 95, pp. 043102-3, 2009.
- [4] E. Pop, D. Mann, Q. Wang, K. Goodson, and H. Dai, "Thermal Conductance of an Individual Single-Wall Carbon Nanotube above Room Temperature," *Nano. Lett.*, vol. 6, pp. 96-100, 2006.
- [5] C. Yu, L. Shi, Z. Yao, D. Li, and A. Majumdar, "Thermal Conductance and Thermopower of an Individual Single-Wall Carbon Nanotube," *Nano Lett.*, vol. 5, pp. 1842-1846, 2005.
- [6] M. P. A. a. F. L'Amour, "Physics of carbon nanotube electronic devices," *Rep. Prog. Phys.*, vol. 69, p. 507, 2006.
- [7] B. Yakobson and P. Avouris, "Mechanical Properties of Carbon Nanotubes," in *Carbon Nanotubes*, 2001, pp. 287-327.
- [8] J. M. Ziman, *Electrons and Phonons*. Oxford: Oxford University Press, 1979.
- [9] F. Claro and G. D. Mahan, "Transient heat transport in solids," *J. Appl. Phys.*, vol. 66, pp. 4213-4217, 1989.
- [10] F. Incropera and D. DeWitt, *Fundamentals of Heat and Mass Transfer*. New York: Wiley and Sons, 2002.

BIBLIOGRAPHY

- [11] A. Feher, A. A. Mamalui, A. Y. Dul'fan, E. S. Syrkin, and A. G. Shkorbatov, "Low-temperature phonon transport in 3D point-contacts " *Low Temperature Physics*, vol. 31, pp. 921-946, 2005.
- [12] R. Prasher, "Predicting the Thermal Resistance of Nanosized Constrictions," *Nano. Lett.*, vol. 5, pp. 2155-2159, 2005.
- [13] R. Prasher, T. Tong, and A. Majumdar, "Diffraction-limited phonon thermal conductance of nanoconstrictions," *App. Phys. Lett.*, vol. 91, pp. 143119-3, 2007.
- [14] G. Chen, "Thermal conductivity and ballistic-phonon transport in the cross-plane direction of superlattices," *Phys. Rev. B*, vol. 57, p. 14958, 1998.
- [15] Y. Chen, D. Li, J. R. Lukes, Z. Ni, and M. Chen, "Minimum superlattice thermal conductivity from molecular dynamics," *Phys. Rev.*, vol. 72, pp. 174302-6, 2005.
- [16] P. Reddy, K. Castelino, and A. Majumdar, "Diffuse mismatch model of thermal boundary conductance using exact phonon dispersion," *App. Phys. Lett.*, vol. 87, pp. 211908-3, 2005.
- [17] D. E. Angelescu, M. C. Cross, and M. L. Roukes, "Heat Transport in Mesoscopic Systems," *Superlattices and Microstructures*, vol. 23, pp. 673-689, 1998.
- [18] H. Zhao and J. B. Freund, "Lattice-dynamical calculation of phonon scattering at ideal Si--Ge interfaces," *J. of Appl. Phys.*, vol. 97, pp. 024903-7, 2005.
- [19] D. A. Young and H. J. Maris, "Lattice-Dynamical Calculation of the Kapitza Resistance Between FCC Lattices," *Phys. Rev. B*, vol. 40, p. 3685 3693, 1989.
- [20] N. Mingo, "Anharmonic Phonon Flow Through Molecular-Sized Junctions," *Phys. Rev. B*, vol. 74, pp. 125402-1 125402-13, 2006.
- [21] R. J. Stevens, L. V. Zhigilei, and P. M. Norris, "Effects of temperature and disorder on thermal boundary conductance at solid-solid interfaces:

BIBLIOGRAPHY

- Nonequilibrium molecular dynamics simulations," *Int. J. of Heat and Mass Trans.*, vol. 50, pp. 3977-3989, 2007.
- [22] E. Schwartz and R. Pohl, "Thermal Boundary Resistance," *Rev. Mod. Phys.*, vol. 61, pp. 605-668, 1989.
- [23] H.-K. Lyo and D. G. Cahill, "Thermal conductance of interfaces between highly dissimilar materials," *Phys. Rev. B*, vol. 73, pp. 144301-6, 2006.
- [24] P. E. P. Lisa De Bellis, Ravi S. Prasher, "Variations of Acoustic and Diffuse Mismatch Models in Predicting Thermal-Boundary Resistance," *J. Thermophys. and Heat Trans.*, vol. 14, pp. 144-150, 2000.
- [25] P. E. Hopkins and P. M. Norris, "Relative Contributions of Inelastic and Elastic Diffuse Phonon Scattering to Thermal Boundary Conductance Across Solid Interfaces," *J. Heat Transfer*, vol. 131, pp. 022402-9, 2009.
- [26] P. E. Phelan, "Application of Diffuse Mismatch Theory to the Prediction of Thermal Boundary Resistance in Thin-Film High-T_c Superconductors," *J. Heat Transfer*, vol. 120, pp. 37-43, 1998.
- [27] R. Prasher, "Acoustic mismatch model for thermal contact resistance of van der Waals contacts," *Appl. Phys. Lett.*, vol. 94, pp. 041905-3, 2009.
- [28] R. S. Prasher and P. E. Phelan, "A Scattering-Mediated Acoustic Mismatch Model for the Prediction of Thermal Boundary Resistance," *J. H. Transfer*, vol. 123, pp. 105-112, 2001.
- [29] W. A. Little, "The transport of heat between dissimilar solids at low temperatures," *Can. J. Phys.*, vol. 37, p. 334, 1959.
- [30] Y. Chen, D. Li, J. R. Lukes, Z. Ni, and M. Chen, "Minimum superlattice thermal conductivity from molecular dynamics," *Phys. Rev. B*, vol. 72, pp. 174302-6, 2005.

BIBLIOGRAPHY

- [31] R. Prasher, T. Tong, and A. Majumdar, "An acoustic and dimensional mismatch model for thermal boundary conductance between a vertical mesoscopic nanowire/nanotube and a bulk substrate," *J. Appl. Phys.*, vol. 102, pp. 104312-10, 2007.
- [32] M. C. Cross and R. Lifshitz, "Elastic Wave Transmission at an Abrupt Junction in a Thin Plate with Application to Heat Transport and Vibrations in Mesoscopic Systems," *Phys. Rev. B*, vol. 64, pp. 085324-1 085324-22, 2001.
- [33] W.-X. Li, T. Liu, and C. Liu, "Phonon Transport Through a Three-Dimensional Abrupt Junction," *Appl. Phys. Lett.*, vol. 89, pp. 163104-1 163104-3, 2006.
- [34] M. A. Panzer and K. E. Goodson, "Thermal resistance between low-dimensional nanostructures and semi-infinite media," *J. Appl. Phys.*, vol. 103, pp. 094301-10, 2008.
- [35] R. Saito, G. Dresselhaus, and M. S. Dresselhaus, *Physical Properties of Carbon Nanotubes*. London: Imperial College Press, 1998.
- [36] R. S. Ruoff and D. C. Lorents, "Mechanical and thermal properties of carbon nanotubes," *Carbon*, vol. 33, pp. 925-930, 1995.
- [37] S. Berber, Y.-K. Kwon, and D. Tománek, "Unusually High Thermal Conductivity of Carbon Nanotubes," *Phys. Rev. Lett.*, vol. 84, pp. 4613-4616, 2000.
- [38] M. A. Osman and D. Srivastava, "Temperature Dependence of the Thermal Conductivity of Single-wall Carbon Nanotubes," *Nanotechnology*, vol. 12, pp. 21-21, 2001.
- [39] S. Maruyama, "A Molecular Dynamics Simulation of Heat Conduction of a Finite Length Single-Walled Carbon Nanotube," *Microscale Thermophysical Engineering*, vol. 7, pp. 41-50, 2003.

BIBLIOGRAPHY

- [40] P. Kim, L. Shi, A. Majumdar, and P. L. McEuen, "Thermal Transport Measurements of Individual Multiwalled Nanotubes," *Phys. Rev. Lett.*, vol. 87, p. 215502, 2001.
- [41] G. D. Mahan and G. S. Jeon, "Flexure modes in carbon nanotubes," *Phys. Rev. B* vol. 70, pp. 075405-11, 2004.
- [42] M. S. Dresselhaus and P. C. Eklund, "Phonons in Carbon Nanotubes." vol. 49: Taylor & Francis, 2000, pp. 705 - 814.
- [43] R. Prasher, "Thermal boundary resistance and thermal conductivity of multiwalled carbon nanotubes," *Phys. Rev. B*, vol. 77, pp. 075424-11, 2008.
- [44] Y. Xiao and et al., "Three-phonon Umklapp process in zigzag single-walled carbon nanotubes," *J. Phys. C: Cond. Matt.*, vol. 15, p. L341, 2003.
- [45] M. S. Dresselhaus, G. Dresselhaus, and A. Jorio, "Unusual Properties and Structure of Carbon Nanotubes." vol. 34, 2004, pp. 247-278.
- [46] J. Hone, M. Whitney, C. Piskoti, and A. Zettl, "Thermal conductivity of single-walled carbon nanotubes," *Phys. Rev. B*, vol. 59, p. R2514, 1999.
- [47] J. Hone, B. Batlogg, Z. Benes, A. T. Johnson, and J. E. Fischer, "Quantized Phonon Spectrum of Single-Wall Carbon Nanotubes," *Science*, vol. 289, pp. 1730-1733, 2000.
- [48] M. A. Panzer, G. Zhang, D. Mann, X. Hu, E. Pop, H. Dai, and K. E. Goodson, "Thermal Properties of Metal-Coated Vertically Aligned Single-Wall Nanotube Arrays," *J. Heat Transfer*, vol. 130, pp. 052401-9, 2008.
- [49] R. Prasher, "Thermal Interface Materials: Historical Perspective, Status, and Future Directions," *Proc. of the IEEE*, vol. 94, pp. 1571-1586, 2006.
- [50] "International Technology Roadmap for Semiconductors," 2004.

BIBLIOGRAPHY

- [51] X. Hu, L. Jiang, and K. E. Goodson, "Thermal Conductance Enhancement of Particle-filled Thermal Interface Materials Using Carbon Nanotube Inclusions," in *Proc. Intersociety Conf. on Thermal and Thermo-mechanical Phenomena in Electronic Systems*, 2004, pp. 63-69.
- [52] X. J. Hu, A. A. Padilla, J. Xu, T. S. Fisher, and K. E. Goodson, "3-Omega Measurements of Vertically Oriented Carbon Nanotubes on Silicon," *J. Heat Transfer*, vol. 128, pp. 1109-1113, 2006.
- [53] C. Dames and G. Chen, "1 omega, 2 omega, and 3 omega methods for measurements of thermal properties," *Rev. Sci. Inst.*, vol. 76, pp. 124902-14, 2005.
- [54] D. G. Cahill, K. Goodson, and A. Majumdar, "Thermometry and Thermal Transport in Micro/Nanoscale Solid-State Devices and Structures," *J. Heat Transfer*, vol. 124, pp. 223-241, 2002.
- [55] J. R. Lukes and H. Zhong, "Thermal Conductivity of Individual Single-Wall Carbon Nanotubes," *J. Heat Transfer*, vol. 129, pp. 705-716, 2007.
- [56] C. W. Padgett and D. W. Brenner, "Influence of Chemisorption on the Thermal Conductivity of Single-Wall Carbon Nanotubes," *Nano. Lett.*, vol. 4, pp. 1051-1053, 2004.
- [57] N. Mingo and D. A. Broido, "Length Dependence of Carbon Nanotube Thermal Conductivity and the "Problem of Long Waves"," *Nano. Lett.*, vol. 5, pp. 1221-1225, 2005.
- [58] N. Mingo and D. A. Broido, "Carbon Nanotube Ballistic Thermal Conductance and Its Limits," *Physical Review Letters*, vol. 95, pp. 096105-4, 2005.
- [59] R. Pan, Z. Xu, Z. Zhu, and Z. Wang, "Thermal Conductivity of Functionalized Single-wall Carbon Nanotubes," *Nanotechnology*, vol. 18, p. 285704, 2007.

BIBLIOGRAPHY

- [60] M. Fujii, X. Zhang, H. Xie, H. Ago, K. Takahashi, T. Ikuta, H. Abe, and T. Shimizu, "Measuring the Thermal Conductivity of a Single Carbon Nanotube," *Phys. Rev. Lett.*, vol. 95, p. 065502, 2005.
- [61] J. Hone, M. C. Llaguno, N. M. Nemes, and A. T. Johnson, "Electrical and Thermal Transport Properties of Magnetically Aligned Single Wall Carbon Nanotube Films," *App. Phys. Let.*, vol. 77, pp. 666-668, 2000.
- [62] W. Yi, L. Lu, Z. Dian-lin, Z. W. Pan, and S. S. Xie, "Linear Specific Heat of Carbon Nanotubes," *Phys. Rev. B*, vol. 59, pp. R9015 -R9018, 1999.
- [63] S. Shenogin, L. Xue, R. Ozisik, R. Koblinski, and D. Cahill, "Role of Thermal Boundary Resistance on the Heat Flow in Carbon-nanotube Composites," *J. Appl. Phys.*, vol. 95, pp. 8136-8144, 2004.
- [64] Q. Z. Xue, "Model for the Effective Thermal Conductivity of Carbon Nanotube Composites," *Nanotechnology*, vol. 17, pp. 1655-1660, 2006.
- [65] S. U. S. Choi, Z. G. Zhang, W. Yu, F. E. Lockwood, and E. A. Grulke, "Anomalous Thermal Conductivity Enhancement in Nanotube Suspensions," *App. Phys. Let.*, vol. 79, p. 2252 2254, 2001.
- [66] M. J. Biercuk, M. C. Llaguno, M. Radosavljevic, J. K. Hyun, A. T. Johnson, and J. E. Fischer, "Carbon Nanotube Composites for Thermal Management," *App. Phys. Let.*, vol. 80, pp. 2767-2769, 2002.
- [67] C. Guthy, F. Du, S. Brand, K. I. Winey, and J. E. Fischer, "Thermal Conductivity of Single-Walled Carbon Nanotube/PMMA Nanocomposites," *J. Heat Transfer*, vol. 129, pp. 1096-1099, 2007.
- [68] D. J. Yang, Q. Zhang, G. Chen, S. F. Yoon, J. Ahn, S. G. Wang, Q. Zhou, Q. Wang, and J. Q. Li, "Thermal Conductivity of Multiwalled Carbon Nanotubes," *Phys. Rev. B*, vol. 66, p. 165440, 2002.

BIBLIOGRAPHY

- [69] T. Tong, Y. Zhao, L. Delzeit, A. Kashani, M. Meyyappan, and A. Majumdar, "Dense Vertically Aligned Multiwalled Carbon Nanotube Arrays as Thermal Interface Materials," *IEEE Transactions on Components and Packaging Technologies*, vol. 30, pp. 92-100, 2007.
- [70] S. T. Huxtable, D. G. Cahill, S. Shenogin, L. Xue, R. Ozisik, P. Barone, M. Usrey, M. S. Strano, G. Siddons, M. Shim, and P. Keblinski, "Interfacial Heat Flow in Carbon Nanotube Suspensions," *Nat. Mater.*, vol. 2, pp. 731-734, 2003.
- [71] G. Zhang, D. Mann, L. Zhang, A. Javey, Y. Li, E. Yenilmez, Q. Wang, J. P. McVittie, Y. Nishi, J. Gibbons, and H. Dai, "Ultra-high-yield Growth of Vertical Single-walled Carbon Nanotubes: Hidden Roles of Hydrogen and Oxygen," *PNAS*, vol. 102, pp. 16141-16145, 2005.
- [72] D. Chu, M. Touzelbaev, S. Babin, R. F. Pease, and K. E. Goodson, "Thermal Conductivity Measurements of Thin-film Resist," *J. Vac. Sci. Technol. B*, vol. 19, pp. 2874-2877, 2001.
- [73] O. W. Kading, H. Skurk, and K. E. Goodson, "Thermal Conduction in Metallized Silicon-dioxide Layers on Silicon," *Appl. Phys. Lett.*, vol. 65, pp. 1629-1631, 1994.
- [74] A. Smith, D. Hostetler, and P. Norris, "Thermal Boundary Resistance Measurements Using a Transient Thermoreflectance Technique," *Microscale Thermophysical Engineering*, vol. 4, pp. 51-60, 2000.
- [75] R. Stoner and H. Maris, "Kapitza Conductance and Heat Flow Between Solids at Temperature from 50 to 300K," *Phys. Rev. B*, vol. 48, pp. 16373-16387, 1993.
- [76] C. A. Paddock and G. L. Eesley, "Transient Thermoreflectance from Thin Metal Films," *J. Appl. Phys.*, vol. 60, pp. 13285-13290, 1986.

BIBLIOGRAPHY

- [77] R. W. Schoenlein, W. Z. Lin, J. G. Fujimoto, and G. L. Eesley, "Femtosecond Studies of Nonequilibrium Electronic Processes in Metals," *Phys. Rev. Lett.*, vol. 58, p. 1680, 1987.
- [78] H. E. Elsayed-Ali, T. B. Norris, M. A. Pessot, and G. A. Mourou, "Time-resolved Observation of electron-phonon Relaxation in Copper," *Physical Review Letters*, vol. 58, p. 1212, 1987.
- [79] K. Ujihara, "Reflectivity of Metals at High Temperatures," *J. Appl. Phys.*, vol. 43, pp. 2376-2383, 1972.
- [80] D. Guidotti and J. Wilman, "Novel and Nonintrusive Optical Thermometer," *Appl. Phys. Lett.*, vol. 60, pp. 524-526, 1991.
- [81] B. Clemens, G. Eesley, and C. Paddock, "Time-resolved Thermal Transport in Compositionally Modulated Metal Films," *Phys. Rev. B*, vol. 37, pp. 1085-1096, 1988.
- [82] H. A. Bethe, "Theory of diffraction by small holes," *Phys. Rev.*, vol. 66, pp. 163-182, 1944.
- [83] E. X. Jin and X. Xu, "Radiation Transfer Through Nanoscale Apertures," *Journal of Quantitative Spectroscopy and Radiative Transfer*, vol. 93, pp. 163-173.
- [84] J. Xu and T. Fisher, "Thermal Contact Conductance Enhancement Using Carbon Nanotube Arrays," in *International Mechanical Engineering Congress and Exposition* Anaheim, CA, 2004, pp. IMECE2004-60185.
- [85] X. J. Hu, M. A. Panzer, and K. E. Goodson, "Infrared Microscopy Thermal Characterization of Opposing Carbon Nanotube Arrays," *J. Heat Transfer*, vol. 129, p. 91, 2007.

BIBLIOGRAPHY

- [86] H. Zhong and J. R. Lukes, "Interfacial Thermal Resistance Between Carbon Nanotubes: Molecular Dynamics Simulations and Analytical Thermal Modeling," *Phys. Rev. B*, vol. 74, p. 125403, 2006.
- [87] P. Phelan, "Application of Diffuse Mismatch Theory to the Prediction of Thermal Boundary Resistance in Thin-Film High-Tc Superconductors," *J. Heat Transfer*, vol. 120, pp. 37-43, 1998.
- [88] J. Xu and T. S. Fisher, "Enhancement of Thermal Interface Materials with Carbon Nanotube Arrays," *Int. J. of Heat and Mass Transfer*, vol. 49, pp. 1658-1666, 2006.
- [89] B. A. Cola, J. Xu, C. Cheng, X. Xu, T. S. Fisher, and H. Hu, "Photoacoustic Characterization of Carbon Nanotube Array Thermal Interfaces," *J. of Appl. Phys.*, vol. 101, pp. 054313-9, 2007.
- [90] T. Y. Tsai, C. Y. Lee, N. H. Tai, and W. H. Tuan, "Transfer of patterned vertically aligned carbon nanotubes onto plastic substrates for flexible electronics and field emission devices," *Appl. Phys. Lett.*, vol. 95, pp. 013107-3, 2009.
- [91] Q. Cao, Z.-T. Zhu, M. G. Lemaitre, M.-G. Xia, M. Shim, and J. A. Rogers, "Transparent flexible organic thin-film transistors that use printed single-walled carbon nanotube electrodes," *Appl. Phys. Lett.*, vol. 88, pp. 113511-3, 2006.
- [92] A. Modi, N. Koratkar, E. Lass, B. Wei, and P. M. Ajayan, "Miniaturized gas ionization sensors using carbon nanotubes," *Nature*, vol. 424, pp. 171-174, 2003.
- [93] E. J. Garcia, B. L. Wardle, and A. John Hart, "Joining prepreg composite interfaces with aligned carbon nanotubes," *Comp. A*, vol. 39, pp. 1065-1070, 2008.
- [94] J. Chen, Y. Liu, A. I. Minett, C. Lynam, J. Wang, and G. G. Wallace, "Flexible, Aligned Carbon Nanotube/Conducting Polymer Electrodes for a Lithium-Ion Battery," *Chem. Mat.*, vol. 19, pp. 3595-3597, 2007.

BIBLIOGRAPHY

- [95] Y. Son, S. K. Pal, T. Borca-Tasciuc, P. M. Ajayan, and R. W. Siegel, "Thermal resistance of the native interface between vertically aligned multiwalled carbon nanotube arrays and their SiO₂/Si substrate," *J. of Appl. Phys.*, vol. 103, pp. 024911-7, 2008.
- [96] H. M. Duong, N. Yamamoto, D. V. Papavassiliou, S. Maruyama, and B. L. Wardle, "Inter-carbon nanotube contact in thermal transport of controlled-morphology polymer nanocomposites," *Nanotechnology*, vol. 20, p. 155702, 2009.
- [97] Y. Murakami, Y. Miyauchi, S. Chiashi, and S. Maruyama, "Direct synthesis of high-quality single-walled carbon nanotubes on silicon and quartz substrates," *Chem. Phys. Lett.*, vol. 377, pp. 49-54, 2003.
- [98] E. Einarsson, H. Shiozawa, C. Kramberger, M. H. Rummeli, A. Gruneis, T. Pichler, and S. Maruyama, "Revealing the Small-Bundle Internal Structure of Vertically Aligned Single-Walled Carbon Nanotube Films," *J. Phys. Chem. C*, vol. 111, pp. 17861-17864, 2007.
- [99] H. M. Duong, K. Ishikawa, J. Okawa, K. Ogura, E. Einarsson, J. Shiomi, and S. Maruyama, "Mechanism and Optimization of Metal Deposition onto Vertically Aligned Single-Walled Carbon Nanotube Arrays," *J. Phys. Chem. C*, vol. 113, pp. 14230-14235, 2009.
- [100] M. Akoshima, K. Hata, D. N. Futaba, K. Mizuno, T. Baba, and M. Yumura, "Thermal Diffusivity of Single-Walled Carbon Nanotube Forest Measured by Laser Flash Method," *J. J. Appl. Phys.*, vol. 48, p. 05EC07, 2009.
- [101] T.-Y. Choi, D. Poulikakos, J. Tharian, and U. Sennhauser, "Measurement of the Thermal Conductivity of Individual Carbon Nanotubes by the Four-Point Three- $\dot{\text{I}}$ % Method," *Nano Lett.*, vol. 6, pp. 1589-1593, 2006.

BIBLIOGRAPHY

- [102] J. Yang, S. Waltermire, Y. Chen, A. A. Zinn, T. T. Xu, and D. Li, "Contact thermal resistance between individual multiwall carbon nanotubes," *Appl. Phys. Lett.*, vol. 96, pp. 023109-3, 2010.
- [103] R. S. Prasher, X. J. Hu, Y. Chalopin, N. Mingo, K. Lofgreen, S. Volz, F. Cleri, and P. Keblinski, "Turning Carbon Nanotubes from Exceptional Heat Conductors into Insulators," *Phys. Rev. Lett.*, vol. 102, pp. 105901-4, 2009.
- [104] M. Hu, P. Keblinski, J.-S. Wang, and N. Ravivkar, "Interfacial thermal conductance between silicon and a vertical carbon nanotube," *J. Appl. Phys.*, vol. 104, pp. 083503-4, 2008.
- [105] J. Diao, D. Srivastava, and M. Menon, "Molecular dynamics simulations of carbon nanotube/silicon interfacial thermal conductance," *J. of Chem. Phys.*, vol. 128, pp. 164708-5, 2008.
- [106] Y. Zhang, N. W. Franklin, R. J. Chen, and H. Dai, "Metal Coating on Suspended Carbon Nanotubes and its Implication to Metal-tube Interaction," *Chemical Physics Letters*, vol. 331, pp. 35-41, 2000.
- [107] M. A. Panzer and K. E. Goodson, "Thermal resistance between low-dimensional nanostructures and semi-infinite media," *J. of Appl. Phys.*, vol. 103, pp. 094301-10, 2008.
- [108] W. Zhang, N. Mingo, and T. S. Fisher, "Simulation of phonon transport across a non-polar nanowire junction using an atomistic Green's function method," *Phys. Rev. B*, vol. 76, pp. 195429-9, 2007.
- [109] D. W. Brenner, "Empirical potential for hydrocarbons for use in simulating the chemical vapor deposition of diamond films," *Phys. Rev. B*, vol. 42, p. 9458, 1990.
- [110] J. Shiomi and S. Maruyama, "Non-Fourier heat conduction in a single-walled carbon nanotube: Classical molecular dynamics simulations," *Phys. Rev. B*, vol. 73, p. 205420, 2006.

BIBLIOGRAPHY

- [111] R. J. Stoner and H. J. Maris, "Kapitza conductance and heat flow between solids at temperatures from 50 to 300 K," *Physical Review B*, vol. 48, p. 16373, 1993.
- [112] P. E. Hopkins, P. M. Norris, and R. J. Stevens, "Influence of Inelastic Scattering at Metal-Dielectric Interfaces," *J. Heat Transfer*, vol. 130, pp. 022401-9, 2008.
- [113] P. Hopkins, R. Salaway, R. Stevens, and P. Norris, "Temperature-Dependent Thermal Boundary Conductance at Al/Al₂O₃ and Pt/Al₂O₃ interfaces," *Int. J. of Thermophysics*, vol. 28, pp. 947-957, 2007.
- [114] M. Panzer, X. Hu, K. Goodson, and D. Mann, "Composite thermal interface material including aligned nanofiber with low melting temperature binder," L. P. Firm, Ed. USA, Submitted 2006.
- [115] D. G. Cahill, "Analysis of Heat flow in Layered Structures for Time-domain Thermoreflectance," *Review of Scientific Instruments*, vol. 75, pp. 5119-5122, 2004.
- [116] W. S. Capinski and H. J. Maris, "Improved Apparatus for Picosecond Pump-and-probe Optical Measurements," *Rev. Sci. Inst.*, vol. 67, pp. 2720-2726, 1996.
- [117] P. M. Norris, A. P. Caffrey, R. J. Stevens, J. M. Klopff, J. James T. McLeskey, and A. N. Smith, "Femtosecond Pump-probe Nondestructive Examination of Materials," *Rev. Sci. Instrum.*, vol. 74, pp. 400-406, 2003.
- [118] A. J. Schmidt, X. Chen, and G. Chen, "Pulse accumulation, radial heat conduction, and anisotropic thermal conductivity in pump-probe transient thermoreflectance," *Rev. Sci. Inst.*, vol. 79, pp. 114902-9, 2008.
- [119] A. J. Schmidt, R. Cheaito, and M. Chiesa, "A frequency-domain thermoreflectance method for the characterization of thermal properties," *Rev. Sci. Inst.*, vol. 80, pp. 094901-6, 2009.

BIBLIOGRAPHY

- [120] N. Taketoshi, T. Baba, E. Schaub, and A. Ono, "Homodyne Detection Technique using Spontaneously Generated Reference Signal in Picosecond Thermoreflectance Measurements," *Rev. Sci. Instrum.*, vol. 74, pp. 5226-5230, 2003.
- [121] D. G. Cahill, "Analysis of Heat Flow in Layered Structures for Time-domain Thermoreflectance," *Rev. of Sci. Inst.*, vol. 75, pp. 5119-5122, 2004.
- [122] A. Schmidt, M. Chiesa, X. Chen, and G. Chen, "An optical pump-probe technique for measuring the thermal conductivity of liquids," *Rev. Sci. Inst.*, vol. 79, pp. 064902-1--064902-5, 2008.
- [123] T. P. R. Center, *Thermophysical Properties of Matter*. Larayette, Ill.: Purdue University Press, 1970.
- [124] Z. Huang, F. Chen, R. D'Agosta, P. A. Bennett, M. Di Ventra, and N. Tao, "Local Ionic and Electron Heating in Single-molecule Junctions," *Nat Nano*, vol. 2, pp. 698-703, 2007.
- [125] K. Schwab, E. A. Henriksen, J. M. Worlock, and M. L. Roukes, "Measurement of the Quantum of Thermal Conductance," *Nature*, vol. 404, pp. 974-977, 2000.
- [126] E. Pop, D. Mann, J. Cao, Q. Wang, K. Goodson, and H. Dai, "Negative Differential Conductance and Hot Phonons in Suspended Nanotube Molecular Wires," *Phys. Rev. Lett.*, vol. 95, p. 155505, 2005.
- [127] C. W. Chang, D. Okawa, A. Majumdar, and A. Zettl, "Solid-State Thermal Rectifier," *Science*, vol. 314, pp. 1121-1124, 2006.
- [128] M. Panzer, G. Zhang, D. Mann, X. Hu, E. Pop, H. Dai, and K. E. Goodson, "Thermal Properties of Metal-Coated Vertically-Aligned Single Wall Nanotube Films," *Accepted for publication in J. Heat Transfer*, vol. HT-06-1448, 2007.

BIBLIOGRAPHY

- [129] A. G. Shkorbatov, Stef. P. nyi, Bystrenov, E., and A. Feher, "Phonon Transport in Pressure-made Point Contacts," *Journal of Physics: Condensed Matter*, vol. 10, pp. 8313-8326, 1998.
- [130] A. G. Shkorbatov, T. Z. Sarkisyan, A. Feher, and P. Stefanyi, "Low-temperature Phonon Thermal Conductivity of Point-contacts," *Low Temp. Phys.*, vol. 19, pp. 881-886, 1993.
- [131] C.-M. Chang and M. R. Geller, "Mesoscopic Phonon Transmission Through a Nanowire-Bulk Contact," *Phys. Rev. B*, vol. 71, pp. 125304-1 125304-8 2005.
- [132] Y. Ohtsubot, N. Nishiguchit, and T. Sakumaf, "The Thermal Conductivity in One-Dimensional Monatomic Lattices with Harmonic and Quartic Interatomic Potentials," *J. Phys.: Condens. Matter*, vol. 6, pp. 3013-3024, 1994.
- [133] A. Ozpineci and S. Ciraci, "Quantum Effects of Thermal Conductance Through Atomic Chains," *Phys. Rev. B*, vol. 63, pp. 125415-1 125415-5, 2001.
- [134] K. R. Patton and M. R. Geller, "Thermal Transport Through a Mesoscopic Weak Link," *Phys. Rev. B*, vol. 64, pp. 155320-1 155320-7, 2001.
- [135] A. Buldum, S. Ciraci, and C. Y. Fong, "Quantum Heat Transfer Through an Atomic Wire," *J. Phys.: Condens. Matter*, vol. 12, pp. 3349-3358, 2000.
- [136] M. E. Lumpkin, W. M. Saslow, and W. M. Visscher, "One-Dimensional Kapitza Conductance: Comparison of the Phonon Mismatch Theory with Computer Experiments," *Phys. Rev. B*, vol. 17, p. 4295 4302, 1978.
- [137] A. S. J. Suiker, A. V. Metrikine, and R. De Borst, "Dynamic Behaviour of a Layer of Discrete Particles, Part 1: Analysis of Body Waves and Eigenmodes," *J. Sound and Vib.*, vol. 240, pp. 1-18, 2001.

BIBLIOGRAPHY

- [138] T. E. Feuchtwang, "Dynamics of a Semi-Infinite Crystal Lattice in a Quasiharmonic Approximation. II. The Normal-Mode Analysis of a Semi-Infinite Lattice," *Phys. Rev.*, vol. 155, pp. 731-743, 1967.
- [139] L. D. Landau and E. M. Lifshitz, *Theory of Elasticity*. New York: Pergamon Press, 1986.
- [140] H. Lamb, "On the Propagation of Tremors over the Surface of an Elastic Solid," *Proc. Soc. Lond.*, vol. 72, pp. 128-130, 1903.
- [141] G. F. Miller and H. Pursey, "The Field and Radiation Impedance of Mechanical Radiators on the Free Surface of a Semi-Infinite Isotropic Solid," *Proc. Soc. Lond. A*, vol. 223, pp. 521-541, 1954.
- [142] G. F. Miller and H. Pursey, "On the Partition of Energy Between Elastic Waves in a Semi-Infinite Solid," *Proc. Soc. Lond. A*, vol. 233, pp. 55-96, 1955.
- [143] T. J. Roystona, H. A. Mansy, and R. H. Sandler, "Excitation and Propagation of Surface Waves on a Viscoelastic Half-Space with Application to Medical Diagnosis," *J. Acoust. Soc. Am.*, vol. 106, p. 3678, 1999.
- [144] W. M. Ewing, W. S. Jaretzky, and R. Press, *Elastic Waves in Layered Media*. New York: McGraw-Hill, 1962.
- [145] D. C. Gazis and R. F. Wallis, "Surface Vibrational Modes in Crystal Lattices with Complex Interatomic Interactions," *J. Math. Phys.*, vol. 3, pp. 190-199, 1962.
- [146] A. M. Kosevich and S. E. Savotchenko, "Surface and Quasi-Surface Phonons and Transformation Waves in a Hexagonal Crystal," *Low Temp. Phys.*, vol. 24, pp. 748-756, 1998.

BIBLIOGRAPHY

- [147] T. E. Feuchtwang, "Dynamics of a Semi-Infinite Crystal Lattice in a Quasiharmonic Approximation. I. The Static Configuration of a Semi-Infinite Lattice," *Phys. Rev.*, vol. 155, pp. 715-729, 1967.
- [148] D. C. Gazis and R. Herman, "Surface Elastic Waves in Cubic Crystals," *Phys. Rev.*, vol. 119, pp. 533-544, 1960.
- [149] S. Datta, *Quantum Transport: Atom to Transistor*. New York: Cambridge University Press, 2005.
- [150] W. Zhang, T. Fisher, and N. Mingo, "The Atomistic Green's Function Method: An Efficient Simulation Approach for Nanoscale Phonon Transport " *Numerical Heat Transfer, Part B*, vol. 51, pp. 333-349, 2007.
- [151] M. C. Deshonoreres and D. Spanjaard, *Concepts in Surface Physics*. Berlin: Springer-Verlag, 1993.
- [152] G. Treglia and M. C. Desjonquères, "Bulk and surface vibrational and thermodynamical properties of fcc transition and noble metals : a systematic study by the continued fraction technique," *J. Phys. France*, vol. 46, pp. 987-1000, 1985.
- [153] M. R. Geller, "Local Phonon Density of States in an Elastic Substrate," *Phys. Rev. B*, vol. 70, pp. 205421-6, 2004.
- [154] N. W. Ashcroft and N. D. Mermin, *Solid State Physics*: Thomas Learning, Inc., 1976.
- [155] W. C. O'Mara, R. B. Herring, and L. P. Hunt, *Handbook of Semiconductor Silicon Technology*. Salem, MA: William Andrew Publishing/Noyes, 1990.
- [156] K. Mistry, C. Allen, C. Auth, B. Beattie, D. Bergstrom, M. Bost, M. Brazier, M. Buehler, A. Cappellani, R. Chau, C. H. Choi, G. Ding, K. Fischer, T. Ghani, R. Grover, W. Han, D. Hanken, M. Hattendorf, J. He, J. Hicks, R. Huessner, D. Ingerly, P. Jain, R. James, L. Jong, S. Joshi, C. Kenyon, K. Kuhn, K. Lee, H. Liu,

BIBLIOGRAPHY

- J. Maiz, B. McLntyre, P. Moon, J. Neiryneck, S. Pae, C. Parker, D. Parsons, C. Prasad, L. Pipes, M. Prince, P. Ranade, T. Reynolds, J. Sandford, L. Shifren, J. Sebastian, J. Seiple, D. Simon, S. Sivakumar, P. Smith, C. Thomas, T. Troeger, P. Vandervoorn, S. Williams, and K. Zawadzki, "A 45nm Logic Technology with High-k+Metal Gate Transistors, Strained Silicon, 9 Cu Interconnect Layers, 193nm Dry Patterning, and 100% Pb-free Packaging," in *IEDM 2007*, 2007, pp. 247-250.
- [157] G. D. Wilk, R. M. Wallace, and J. M. Anthony, "High-k gate dielectrics: Current status and materials properties considerations," *J. Appl. Phys.*, vol. 89, pp. 5243-5275, 2001.
- [158] E. Pop, S. Sinha, and K. E. Goodson, "Heat Generation and Transport in Nanometer-Scale Transistors," *Proc. IEEE*, vol. 94, pp. 1587-1601, 2006.
- [159] H. Kim, P. C. McIntyre, and K. C. Saraswat, "Effects of crystallization on the electrical properties of ultrathin HfO₂ dielectrics grown by atomic layer deposition," *App. Phys. Lett.*, vol. 82, pp. 106-108, 2003.
- [160] Z. Xu, M. Houssa, R. Carter, M. Naili, S. De Gendt, and M. Heyns, "Constant voltage stress induced degradation in HfO₂/SiO₂ gate dielectric stacks," *J. Appl. Phys.*, vol. 91, pp. 10127-10129, 2002.
- [161] R. Jiang, E. Xie, and Z. Wang, "Interfacial chemical structure of HfO₂/Si film fabricated by sputtering," *Appl. Phys. Lett.*, vol. 89, pp. 142907-1-142907-3, 2006.
- [162] O. Renault, D. Samour, D. Rouchon, P. Holliger, A. M. Papon, D. Blin, and S. Marthon, "Interface properties of ultra-thin HfO₂ films grown by atomic layer deposition on SiO₂/Si," *Thin Solid Films*, vol. 428, pp. 190-194, 2003.
- [163] S. M. Lee, D. G. Cahill, and T. H. Allen, "Thermal conductivity of sputtered oxide films," *Phys. Rev. B*, vol. 52, pp. 253-257, 1995.

BIBLIOGRAPHY

- [164] M. Hinz, O. Marti, B. Gotsmann, M. A. Lantz, and U. Durig, "High resolution vacuum scanning thermal microscopy of HfO_2 and SiO_2 ," *Appl. Phys. Lett.*, vol. 92, pp. 043122-1--043122-3, 2008.
- [165] J. D. Plummer, M. D. Deal, and P. B. Griffin, "Silicon VLSI Technology — Fundamentals, Practice and Modeling," Prentice Hall, 2000, p. 159.
- [166] T. Sugawara, R. Sreenivasan, and P. C. McIntyre, "Mechanism of germanium plasma nitridation," *J. Vac. Sci. Technol. B*, vol. 24, pp. 2442-2448, 2006.
- [167] M. T. Ho, Y. Wang, R. T. Brewer, L. S. Wielunski, Y. J. Chabal, N. Moumen, and M. Boleslawski, "In situ infrared spectroscopy of hafnium oxide growth on hydrogen-terminated silicon surfaces by atomic layer deposition," *Appl. Phys. Lett.*, vol. 87, pp. 133103-1--133103-3, 2005.
- [168] H. Kim, P. C. McIntyre, C. O. Chui, K. C. Saraswat, and S. Stemmer, "Engineering chemically abrupt high-k metal oxide/silicon interfaces using an oxygen-gettering metal overlayer," *J. Appl. Phys.*, vol. 96, pp. 3467-3472, 2004.
- [169] R. M. Costescu, M. A. Wall, and D. G. Cahill, "Thermal conductance of epitaxial interfaces," *Phys. Rev. B*, vol. 67, pp. 054302-1--054302-5, 2003.
- [170] D. G. Cahill, S. K. Watson, and R. O. Pohl, "Lower Limit to the Thermal Conductivity of Disordered Crystals," *Phys. Rev. B*, vol. 46, pp. 6131-6140, 1992.
- [171] K. F. M. Ivanda, S. Music', M. Ristic', M. Gotic', D. Ristic', A. M. Tonejc, I. Djerdj, M. M. M. Mattarelli, F. Rossi, M. Ferrari, A. Chiasera, Y. Jestin, G. C. Righini, and a. R. R. G. W. Kiefer, "Low wavenumber Raman scattering of nanoparticles and nanocomposite materials," *J. Raman Spectrosc.*, vol. 38, pp. 647-659, 2007.
- [172] J. J. Freeman and A. C. Anderson, "Thermal conductivity of amorphous solids," *Phys. Rev. B*, vol. 34, pp. 5684 - 5690, 1986.

BIBLIOGRAPHY

- [173] R. M. Costescu, D. G. Cahill, F. H. Fabreguette, Z. A. Sechrist, and S. M. George, "Ultra-Low Thermal Conductivity in W/Al₂O₃ Nanolaminates," *Science*, vol. 303, pp. 989-990, 2004.
- [174] W. Kim, J. Zide, A. Gossard, D. Klenov, S. Stemmer, A. Shakouri, and A. Majumdar, "Thermal Conductivity Reduction and Thermoelectric Figure of Merit Increase by Embedding Nanoparticles in Crystalline Semiconductors," *Phys. Rev. Lett.*, vol. 96, pp. 045901-1--045901-4, 2006.
- [175] M. Panzer, G. Zhang, D. Mann, X. Hu, E. Pop, H. Dai, and K. E. Goodson, "Thermal Properties of Metal-Coated Vertically-Aligned Single Wall Nanotube Films," in *Proc. Intersociety Conference on Thermal and Thermomechanical Phenomena in Electronic Systems (Itherm)* San Diego, California, 2006.
- [176] M. Panzer, A. Marconnet, H. Duong, Y. N., L. Pan, S. Dogbe, B. Wardle, and K. Goodson, "Thermal Conductivity and Boundary Resistance of Aligned Carbon Nanotube Films and their Polymeric Composites," in *Materials Research Society*, San Francisco, 2009.
- [177] I. K. Hsu, M. T. Pettes, A. Bushmaker, M. Aykol, L. Shi, and S. B. Cronin, "Optical Absorption and Thermal Transport of Individual Suspended Carbon Nanotube Bundles," *Nano Lett.*, vol. 9, pp. 590-594, 2009.
- [178] B. A. Cola, J. Xu, and T. S. Fisher, "Contact mechanics and thermal conductance of carbon nanotube array interfaces," *Int. J. Heat and Mass Trans.*, vol. 52, pp. 3490-3503, 2009.
- [179] B. A. Cola, X. Xu, and T. S. Fisher, "Increased Real Contact in Thermal Interfaces: A Carbon Nanotube/foil Material," *Appl. Phys. Lett.*, vol. 90, pp. 093513-3, 2007.

BIBLIOGRAPHY

- [180] Y. Gao, A. Marconnet, M. Panzer, S. LeBlanc, S. Dogbe, and K. E. Goodson, "Nanostructured Interfaces for Thermoelectrics," in *Proc. 28th Int. Conf. on Thermoelectrics* Freiburg, Germany, 2009.
- [181] SuhrJ, VictorP, CiL, SreekalaS, ZhangX, NalamasuO, and P. M. Ajayan, "Fatigue Resistance of Aligned Carbon Nanotube Arrays Under Cyclic Compression," *Nat. Nano.*, vol. 2, pp. 417-421, 2007.
- [182] H. J. Qi, K. B. K. Teo, K. K. S. Lau, M. C. Boyce, W. I. Milne, J. Robertson, and K. K. Gleason, "Determination of mechanical properties of carbon nanotubes and vertically aligned carbon nanotube forests using nanoindentation," *J. of the Mech. Phys. of Solids*, vol. 51, pp. 2213-2237, 2003.
- [183] Suhr J, Victor P, Ci L, Sreekala S, Zhang X, Nalamasu O, and P. M. Ajayan, "Fatigue Resistance of Aligned Carbon Nanotube Arrays Under Cyclic Compression," *Nat. Nano.*, vol. 2, pp. 417-421, 2007.
- [184] Z. Wang, J. A. Carter, A. Lagutchev, Y. K. Koh, N.-H. Seong, D. G. Cahill, and D. D. Dlott, "Ultrafast Flash Thermal Conductance of Molecular Chains," *Science*, vol. 317, pp. 787-790, 2007.
- [185] P. Reddy, S.-Y. Jang, R. A. Segalman, and A. Majumdar, "Thermoelectricity in Molecular Junctions," *Science*, vol. 315, pp. 1568-1571, 2007.